Promoting Negative Gaussian Curvature in Lyotropic Liquid Crystal Systems with Oleate-Derived Gemini Surfactants

A THESIS
SUBMITTED TO THE FACULTY OF THE
UNIVERSITY OF MINNESOTA
BY

Michelle T. Hoard

IN PARTIAL FULFILMENT OF THE REQUIREMENTS
FOR THE DEGREE OF
MASTER OF SCIENCE

Mahesh Mahanthappa

July 2019

Acknowledgements

Throughout my time in graduate school, I have benefitted from the gracious support of family, friends, mentors, and colleagues. It is through their efforts and kindness that I have grown as an engineer and researcher.

Foremost, I would like to express my gratitude to my advisor, Professor Mahesh Mahanthappa, for his guidance, continuous motivation, enduring enthusiasm, and the immense amount of knowledge that he has shared with me.

Additionally, I would like to thank the entire Mahanthappa research group, not only for their mentorship and research guidance, but also for their friendship and good company. Specifically, I would like to thank Dr. Grayson Jackson, Carlos Baez-Cotto, and Ashish Jayaraman for their mentorship and discussions related to surfactant self-assembly. Moreover, I would like to thank Dr. Tyler Mann, to whom I owe much gratitude for his organic synthesis tutelage and unrelenting patience in lab.

Finally, I would like to thank the beamline scientists at the Advance Photon Source at Sector 12-ID-B, Byeongdu Lee and Alexis Quental, for all of the resources that they have provided.

Financial Support

We gratefully acknowledge financial support from the University of Minnesota – Twin Cities and the College of Science and Engineering, along with the National Science Foundation under Grant No. CHE-1608115 and CHE-1807330. This work was also supported by the National Science Foundation Graduate Research Fellowship under Grant No. 000039202. Synchrotron SAXS studies were carried out at the Advanced Photon Source (Argonne National Lab in Argonne, IL) at Sector 12-ID-B, which is supported by the U.S. Department of Energy, Office of Science, Office of Basic Energy Sciences under Contract No. DE-AC02-06CH11357.

Dedication

In loving memory of my mom;

And in dedication to both my parents for their unending love and support

Abstract

Lyotropic liquid crystals (LLCs) are formed by solvent-driven microphase separation of amphiphilic molecules to yield assemblies with hydrophilic and hydrophobic domains. Commonly observed mesophases include: lamellae (flat curvature), cylinders, sphere packings, and network phases. Unlike lamellae and cylinders, which have constant mean curvature, networks phases deviate from constant mean curvature with local regions of flat curvature and negative Gaussian curvature (NGC) or "saddle-splay". Lyotropic liquid crystals (LLCs) are excellent platforms for studying the formation of NGC interfaces because they are well-controlled systems with many tunable parameters. This thesis focuses on molecular amphiphilic designs that promote network LLC phase formation by trying to create packing mismatch between the hydrophilic and hydrophobic regions though the use of long-tail gemini dicarboxylates with unsaturated tails. Small angle X-ray scattering was used to observe the phase behavior of potassium oleate and tetramethylammonioum oleate, as well as preliminary exploration of the oleate-derived gemini surfactant.

Table of Contents

Acknowledgements ..... **i**

Financial Support ..... **ii**

Dedication ..... **iii**

Abstract ..... **iv**

Table of Contents ..... **v**

List of Tables ..... **vii**

List of Figures ..... **viii**

List of Schemes ..... **x**

Chapter 1: Design Rules for Promoting Negative Gaussian Curvature **1**

1.1 Overview 2

1.2 Biological Membranes 3

1.3 Phase Behavior of Lyotropic Liquid Crystals 6

1.4 Experimental Design Criteria that Stabilize LLC Network Phases 10

Chapter 2: LLC Phase Behavior of Oleate Salts **17**

2.1 Introduction 18

2.2 Experimental 19

2.3 Results 20

2.4 Discussion 23

2.5 Conclusions 30

Chapter 3: Synthesis and LLC Phase Behavior of an Oleate Gemini Surfactant **32**

3.1 Introduction 33

3.2 Oleate Gemini Synthesis via Olefin Metathesis 34

3.3 K-C19:1 Gemini Synthesis via Wittig Reaction 41

3.4 LLC Phase Behavior of Oleate Gemini Acid-Soaps 49

3.5 Conclusions 53

Chapter 4: Conclusion and Outlook **55**

4.1 Conclusion 56
4.2 Outlook 57
References 60
Appendix 1: Supporting Information for Chapter 2 - LLC Phase Behavior of Oleate Salts 70
Appendix 2: Supporting Information for Chapter 3 - Synthesis and LLC Phase Behavior of Oleate Gemini 88

List of Tables

Table A1.1: Lab notebook page numbers for synthesis oleate salts 70
Table A1.2: Phase data for **NMe_4-oleate**/water and **K-oleate**/water mixtures..... 83
Table A1.3: Partially interdigitated bilayer tail packing data for **NMe_4-oleate** and **K-oleate**..... 84

Table A2.1: Laboratory notebook page numbers for synthesis steps of oleate gemini, **4**, via olefin metathesis 88
Table A2.2: Olefin metathesis conditions and yields 88
Table A2.3: Laboratory notebook page numbers for synthesis steps of oleate gemini, **11**, via Wittig olefination 94
Table A2.4: Measured and calculated L_α parameters for K-C19:1 gemini (**11**)/water system 95

List of Figures

Figure 1.1: Diagram of lamellar phases 3
Figure 1.2: Diagram of NGC in biological membranes 4
Figure 1.3: Cardiolipin 5
Figure 1.4: Monte Carlo simulation of adding anisotropic inclusions to a membrane 5
Figure 1.5: LLC mesophases 7
Figure 1.6: Minimal surfaces of bicontinuous shown phases 8
Figure 1.7: Structure and phase diagram of monoglyceride fatty acids 11
Figure 1.8: Branched-tail amphiphiles that form inverse network phases 12
Figure 1.9: Ionic gemini molecules that form network phases 14

Figure 2.1: Representative SAXS patterns and phase diagram for **NMe_4-oleate** 21
Figure 2.2: Phase diagram for **K-oleate** 23
Figure 2.3: Lattice parameters for oleate salts 24
Figure 2.4: 1D SAXS pattern of **K-oleate** at 57.5 wt% and 70 °C 26
Figure 2.5: Area per headgroup of oleate salts 27
Figure 2.6: Partially interdigitated L_α model 28
Figure 2.7: Tail splay and bilayer thickness of oleate salts 30

Figure 3.1: Isomerization pathway during olefin metathesis 40
Figure 3.2: Representative SAXS patterns and phase diagram for K-C19:1 gemini 50
Figure 3.2: Representative SAXS patterns and phase diagram for K-C19:1 gemini 50
Figure 3.3: L_α *d*-spacings for K-C19:1 gemini 51
Figure 3.4: Area per headgroup of K-C19:1 gemini 53
Figure 3.5: Bilayer thickness of K-C19:1 gemini 53

Figure A1.1: Diagram of rectangular (ribbon) and complex hexagonal phases 72
Figure A1.2: 1D SAXS patterns of **K-oleate** at 55 wt% after annealing for 1.5 hours at 60 °C. 72
Figure A1.3: 1D SAXS patterns of **K-oleate** at 60 wt% 74
Figure A1.4: Electron density reconstruction of **K-oleate** at 60 wt% 74
Figure A1.5: 2D SAXS pattern of **K-oleate** at 70 wt% and 59.4 °C 75
Figure A1.6: 3-dimensional packing of cylinders for a non-interdigitated, partially interdigitated, and fully interdigitated structure 82
Figure A1.7: Diagram of partially interdigitated bilayer 82
Figure A1.8: 1D SAXS patterns of **NMe_4-oleate** at 10 wt% tetradecane loading and 40 wt% surfactant. 85

Figure A2.1: ^{1}H NMR of olefinic protons for HG2 catalyzed product 89
Figure A2.2: Mass spectrometry showing isomerization products without inhibitor..... 90
Figure A2.3: Isomerization pathways..... 91
Figure A2.4: Mass spectrometry showing reduction of isomerization products with inhibitor..... 92
Figure A2.5: Mass spectrometry showing ring-closing metathesis and higher order coupling byproducts..... 93
Figure A2.6: ^{1}H NMR of olefinic protons for *Z*-selective Wittig reaction..... 94

List of Schemes

Scheme 2.1: Oleate salt synthesis 19

Scheme 3.1: Olefin metathesis route to oleate-derived gemini..... 35
Scheme 3.2: Wittig reaction route to oleate-derived gemini..... 42

Scheme 4.1: Proposed synthesis of gemini surfactant with cyclic tail end using Wittig reaction..... 58
Scheme 4.2: Proposed synthesis of potassium oleate with deuterated tail ends using a Wittig reaction 59

Chapter 1: Design Rules for Promoting Negative Gaussian Curvature

1.1 Overview

Cell membranes are composed of amphiphilic molecules, or lipids, that self-assemble on the nanometer length scale.[1] In biological membranes, lipid self-assembly provides the mobility required for the membrane to react in response to external stimuli.[2] While many membrane bilayers prefer flat or minimal curvature, membrane functions such as fusion, fission, and pore formation require the formation of negative Gaussian curvature (NGC), also known as "saddle-splay" curvature.[3] The ability of cell membranes to adopt NGC depends on many parameters, including amphiphile structure and lipid composition.

NGC is also observed in microphase-separated lyotropic liquid crystal (LLC) assemblies.[4] Microphase separation between the hydrophilic and hydrophobic domains drives lyotropic liquid crystal self-assembly into different morphologies such as lamellae (stacks of bilayers), hexagonally-packed columns, ordered arrays of quasispherical micelles, and polycontinuous network phases.[5] Network phases contain interconnected hydrophilic and hydrophobic channels that exhibit non-constant mean curvature, with regions of flat (zero) curvature and regions of NGC (saddle curvature).[6] While the structure of network phases makes them desirable for many applications including drug delivery[7] and protein crystallization[8], they are traditionally only observed over narrow concentration windows.

The goal of this chapter is to review the current understanding of amphiphile self-assembly into NGC structures, emphasizing conditions for NGC formation in biological membranes and also in LLC systems. The end of this chapter focuses on understanding

molecular design parameters for stabilizing NGC in LLC systems over wider phase windows.

1.2 Biological Membranes

1.2.1 Bilayer Polymorphism

Biological membranes are mostly comprised of lipids and proteins. Membrane lipids are amphiphilic molecules in which the hydrophobic tails self-associate and the hydrophilic headgroups prefer to interact with aqueous environments. Most anhydrous lipids form crystals, whereas mixing with water directs them to self-assemble into various crystalline, liquid crystalline, or disordered phases.[9] Under most physiological conditions, lipids form bilayer structures (or lamellar phases). A bilayer is composed of two lipid layers (known as leaflets), in which the polar headgroups line the outside of the bilayer and the hydrophobic tails are inside (Figure 1.1).

Thermotropic polymorphism has been well studied in lipid bilayers by many techniques including infrared spectroscopy,[10] differential thermal analysis (DTA),[11] differential scanning calorimetry (DSC),[12] nuclear magnetic resonance (NMR),[13] electron microscopy,[14] and X-ray diffraction.[15] Below the melting temperature of the hydrocarbon chains, lipid tails are rigid and the membranes are said to be in the gel phase, L_β, or crystalline, L_c, forms. The gel phase exhibits multiple known polymorphs including structures in which the tails form

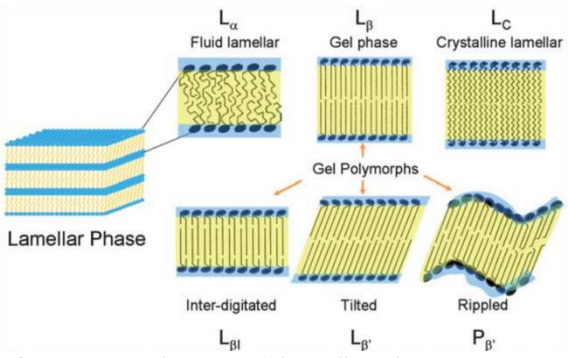

Figure 1.1: Diagram of lamellar phases

Crystalline and liquid crystalline lamellar phases (bilayers) are commonly observed in biological membranes.[9] Fig. from Ref [9]

interdigitated, tilted, and rippled structures.[9] Above the melting temperature, the hydrocarbon tails become fluid and exhibit a high degree of molecular mobility, giving rise to a lamellar liquid crystalline phase, L_α (Figure 1.1). For phospholipids containing shorter chain lengths or unsaturated bonds, the $L_\beta \rightarrow L_\alpha$ phase transition occurs at lower temperatures.

1.2.2 Importance of Negative Gaussian Curvature

While many naturally-occurring membranes prefer flat curvature, non-flat curvature is of great biological importance because it is critical to cellular activity such as movement, transport, growth, and division.[3] A classic example is the plasma membrane of red blood cells whose biconcave, disc-like geometry allows for greater surface area and increased oxygen absorption.[16] Furthermore, the formation of negative Gaussian curvature (NGC) or "saddle-splay" curvature is required for membrane activities such as pore formation, fusion, and fission (Figure 1.2 A).[3-4] The Gaussian curvature, K, of a point on a surface is defined as the product of the principal curvatures at that point. A surface has NGC when it curves away

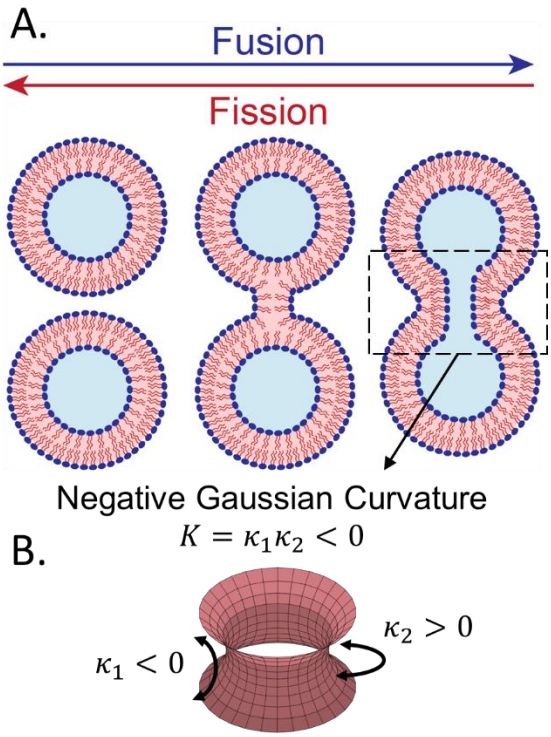

Figure 1.2: Diagram of NGC in biological membranes

A. Vesicle fusion and fission processes create a stalk with negative Gaussian curvature or "saddle-splay" curvature shown in dashed box. **B.** A catenoid surface having negative Gaussian curvature depicts the surface formed by membranes during fusion, fission, and pore formation where κ_1 and κ_2 are principal curvatures.

from the tangent plane in two different directions; hence, the principal curvatures have opposite signs (Figure 1.2 B).

Recent molecular dynamics simulations and experimental studies of cardiolipin, a tetra-tail gemini lipid present in bacterial and mitochondrial membranes (Figure 1.3), was found to increase membrane deformability by aggregating at regions of high negative curvature[18] and trigger the formation of non-lamellar structures.[19] Additionally, cardiolipin clusters at areas with saddle curvature along the pore perimeter during cytochrome *c* triggered pore formation. These experimental observations coincide well with theory: Fournier predicted that introducing anisotropic inclusions in a membrane bilayer would favor NGC and that anisotropic inclusions orient themselves on saddle points.[20] In subsequent work by Dommersnes and Fournier, Monte

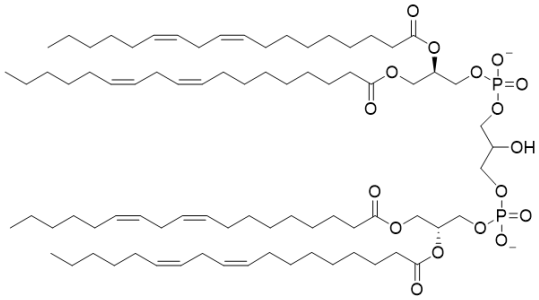

cardiolipin

Figure 1.3: Cardiolipin

Cardiolipin is a naturally occurring tetra-tail gemini lipid found in bacterial and mammalian mitochondrial membranes. The tails are each 18 carbons long, varying from 1-3 degrees of unsaturation. Tails with 2 degrees of unsaturation is depicted above.

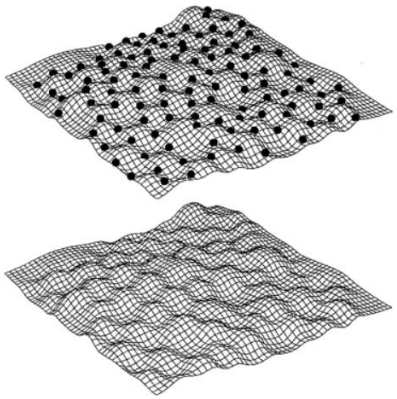

Figure 1.4: Monte Carlo simulation of adding anisotropic inclusions to a membrane

Results of Monte Carlo simulation show that adding anisotropic inclusions to a membrane create an “egg-carton” structure. The top figure shows the black anisotropic inclusions aggregate at the saddle-points[17] Fig. from Ref. [17].

Carlo simulations demonstrated that anisotropic inclusions will aggregate and, thus, form an "egg-carton" structure with the inclusions located at the saddle points (Figure 1.4).[17]

Naturally occurring examples of NGC-forming membranes have been observed in eukaryotic cells. In the endoplasmic reticulum (ER), vesicles that transport proteins to the Golgi apparatus selectively bud from structures having NGC within the peripheral ER membrane.[21] Furthermore, specific proteins have been observed to help stabilize NCG. The M2 protein of the influenza A virus has been found to mediate viral budding by stabilizing NGC to allow a virus to leave the host cell during the replication process.[22] Similarly, monomeric α-synuclein, an amyloid protein associated with Parkinson's disease, binds to anionic lipid membranes causing bilayer thinning and inducing local NGC.[23]

Additionally, a lot of effort has been focused at inducing curvature in cellular membranes for effective intracellular drug or RNA delivery.[24-25] Most targeted drug carriers enter the cell through endocytosis, during which the drug and carrier are encapsulated in an endosome. While there are multiple methods for endosomal escape, two prevalent methods, pore formation and endosomal fusion, require formation of NGC interfaces.[25] Hence, understanding NGC interface formation has implications in membrane activity, viral replication, and developing intracellular drug delivery vehicles.

1.3 Phase Behavior of Lyotropic Liquid Crystals

1.3.1 Generalized Phase Behavior

Aside from the saddle-splay curvature seen in biological membranes, NGC is also observed in systems with long-range crystallographic order known as liquid crystals (LCs).[5, 26] LCs can be classified as either thermotropic or lyotropic, meaning that phase

transitions are induced by changes in temperature or concentration, respectively.[26] Self-assembly of lyotropic liquid crystals is driven by the hydrophobic effect, the entropic drive for small hydrophobic molecules to aggregate in water.[27-28] This effect arises from a minimization of the disruption of hydrogen-bonding in water, and the favorable cohesive forces between non-polar components which grow linearly with volume. The rearrangement to form an interface is costly from a free energy viewpoint and grows linearly with surface area.[27] The global morphology of the system depends on many parameters including temperature, pH, pressure, hydration, and amphiphilic structure.[29] Hence, LLCs are a well-defined platform with many tunable parameters that allow us to study design criteria for promoting NGC and to develop new insights into biological membrane processes.

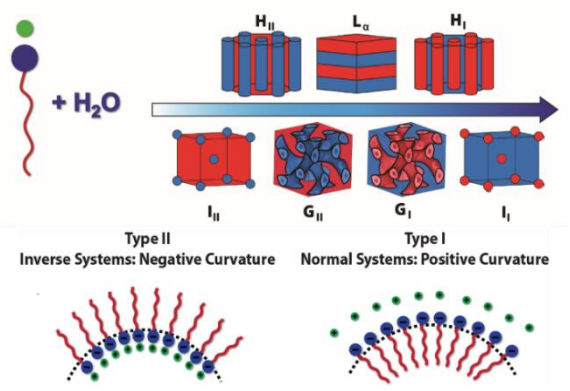

Figure 1.5: LLC mesophases

Highly concentrated aqueous solutions of ionic surfactants self-assemble to form LLCs of micellar (I), cylindrical (H), network phases such as double gyroid (G), and lamellar (L_α) phases. Type I (normal) phases are defined by positive curvature towards the hydrophobic domains; whereas Type II (inverse) phases have positive curvature towards aqueous domains.[30]

LLCs exhibit a plethora of mesophases ranging from high curvature to flat curvature. These morphologies include ordered arrays of micelles (I), hexagonally-packed columns (H), network phases such as double gyroid (G), and lamellae (L_α) (Figure 1.5). As a result of the intricate mesostructures, LLCs have been studied for many applications including water filtration membranes,[31] protein crystallization,[32] templates for mesoporous

silicate synthesis,[33] drug delivery vehicles,[7, 34-35] and even as biological sensors for bacteria and viruses.[36] LLC morphologies are classified into two types: Type I (normal) phases are defined by positive curvature towards the hydrophobic domains; whereas Type II (inverse) phases have positive curvature towards the aqueous domains.

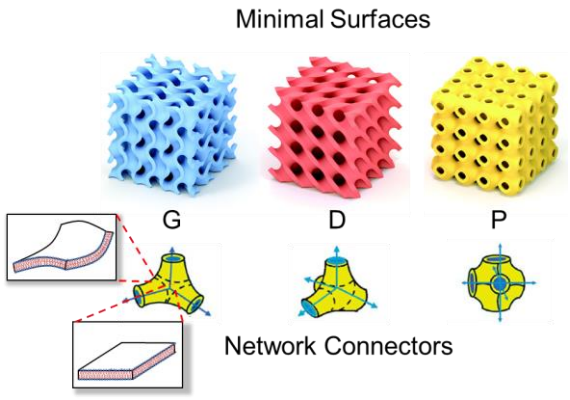

Figure 1.6: Minimal surfaces of bicontinuous shown phases

Shown above are the minimal surfaces for double gyroid (G), double diamond (D), and primitive (P).[37] The networks of these phases have 3, 4, and 6-fold connectors, respectively (below). The 3-fold connector of double gyroid is shown having local regions of flat curvature and negative Gaussian curvature ("saddle-splay"). [38] Figure adapted from Ref [37] and Ref [38].

1.3.2 Network Phase LLCs

NGC is a distinguishing characteristic of LLC network phases, which are typically observed between L_α (flat) and H (highly curved).[39-40] The three commonly observed bicontinuous cubic phases are double gyroid (G, *Ia3(-)d*), double diamond (D, *Pn3(-)m*), and primitive (P, *Im3(-)m*). G, D, and P consist of 3, 4, and 6-fold connectors, respectively, that form interpenetrating hydrophobic and hydrophilic channels in 3-dimensions. The connectors of these phases have regions of flat (zero) curvature and regions of NGC ("saddle-splay" curvature).[41] Figure 1.6 shows the triply periodic minimal surfaces of G, D, and P. In addition to the bicontinuous cubic phases, a 3D-hexagonal network phase, with the space group $P6_3/mcm$, was first predicted by Hyde and Schroder[39-40] and later observed in aqueous gemini-dicarboxylate surfactants.[42]

Inverse (Type II) bicontinuous phases are particularly appealing for drug delivery because the bicontinuous channels allow for controlled release of molecules and can incorporate a wide range of hydrophobic and hydrophilic therapeutics.[7, 43] Leal *et al*. demonstrated that cubosome vehicles with G_{II} (Type II) morphology resulted in more efficient delivery of siRNA than liposomal carriers as a result of enhanced rates of fusion of the complex with the endosomal membrane.[34] Bicontinuous cubic phases have also been studied for protein crystallization.[8, 44-45] Landau and Rosenbusch found that the bicontinuous cubic phases provided nucleation sites and facilitated crystal growth by allowing protein molecules to diffuse laterally through the membrane, but micellar phases did not allow for protein crystallization.[46]

While network phases are useful for the aforementioned applications, the non-constant mean curvature causes unfavorable differences in headgroup hydration and local hydrophobic tail packing. Hence, saddle-splay curvature LLC structures are observed only in limited concentration and temperature windows.[47] Defining experimental design criteria for stabilizing NGC is the motivation for this work.

1.3.3 Methods of LLC Identification

There are two widely used methods for LLC characterization: (1) polarized optical microscopy (POM) and (2) small angle X-ray scattering (SAXS). In POM, a LLC sample is placed between a set of cross-polarizers and the optical texture is observed on a white light illumination using a microscope. One- and two- dimensional LLC morphologies, such as H and L_α, are optically anisotropic and result in birefringent textures when observed between cross polarizers.[48] However, LLC network phases, such as G, D, and P, are three-

dimensionally isotropic; thus, they exhibit no birefringence and appear black between cross polarizers. While distinctions can be made between different birefringent LLCs, POM does not provide structural information and cannot distinguish between network phases. Conversely, SAXS enables elucidation of detailed structural information about the different morphologies. In SAXS, X-ray diffraction arises from differences in electron density between the periodic hydrophilic and hydrophobic domains. Not only is SAXS employed for discerning LLC phases, but can also be used to obtain characteristic dimensions such as unit cell parameters and pore diameters.[5] Additional techniques, such as Differential Scanning Calorimetry (DSC)[49] and rheology[50] have been used to help identify phase transition temperatures, however, they do not furnish any structural information. In instances of very large amphiphilic molecules, such as block copolymers, electron microscopy has been used to obtain LC phase information by direct visualization.[51-52]

1.4 Experimental Design Criteria that Stabilize LLC Network Phases

1.4.1 Effects of Hydrophobic Tail Structure

The hydrophobic tail structure influences the way in which tail packing occurs and, thus, impacts the LLC phase behavior. Israelachvili quantified the relationship between the interfacial area for the hydrophilic headgroup and hydrophobic tail in terms of the packing parameter, P, which is given by:

$$P = \frac{v}{a_0 l_c} \tag{1.1}$$

where v is the hydrophobic volume, a_0 is the effective area per headgroup, and l_c is the hydrophobic tail length.[28, 53] If $P \approx 1$, then the amphiphiles prefer to form zero-curavture

interfaces. Amphiphiles tend to form positive curvature interfaces when P is less than 1 (bulky headgroups compared to tails) and negative curvature interfaces when P is greater than 1 (bulky tails compared to headgroups). Since the values of v, a_0, and l_c are not constant for a given surfactant and can change with temperature, hydration, and pH, the packing parameter is not an all-encompassing model, but rather a geometric rationalization for self-assembly.[56-57] However, it teaches that changes in the hydrophobic tail (v and l_c) will influence the phases formed.

Monoolein, also known as glycerol monooleate (Figure 1.7c), is used as a food emulsifier and has gained much attention for its ability to form inverse bicontinuous cubic phases largely in part to form cubosome drug delivery vehicles.[58] In monoolein systems, packing frustrations destabilize L_α to make network phases. The oleate tail structure of monoolein has 18 carbons with a 9,10-*cis*-unsaturation that fixes the tail at an angle, thus, inducing packing frustration. Work by Kulkarni *et al.*[54] and Qiu *et al.*[55, 59] showed that increasing "chain splay" by changing the number, position, and isomerism of the

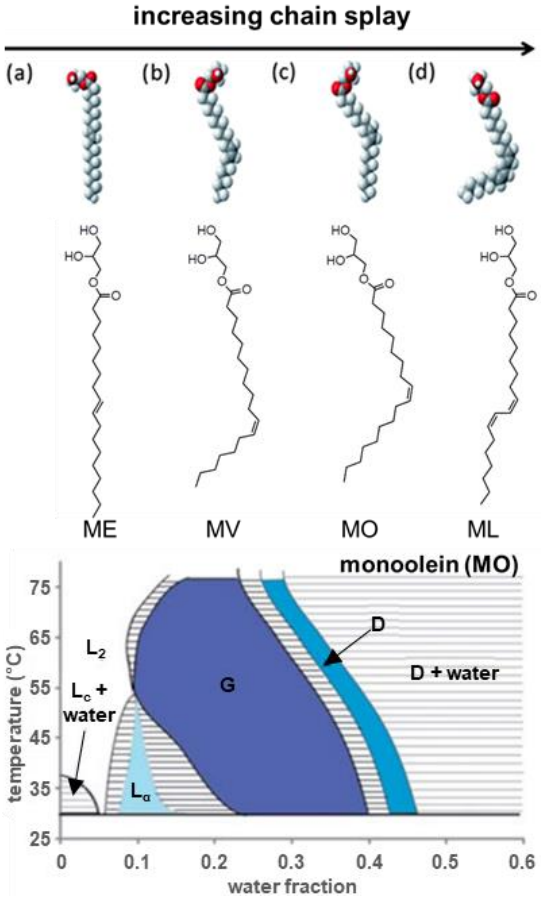

Figure 1.7: Structure and phase diagram of monoglyceride fatty acids

Increasing hydrocarbon chain splay (top) of unsaturated monoglyceride fatty acids: monoelaidin (ME), monovaccenin (MV), monoolein (MO), monolinolein (ML). Phase diagram (bottom) of monoolein/water system.[54-55] Fig. adapted from Ref. [54] and Ref. [55].

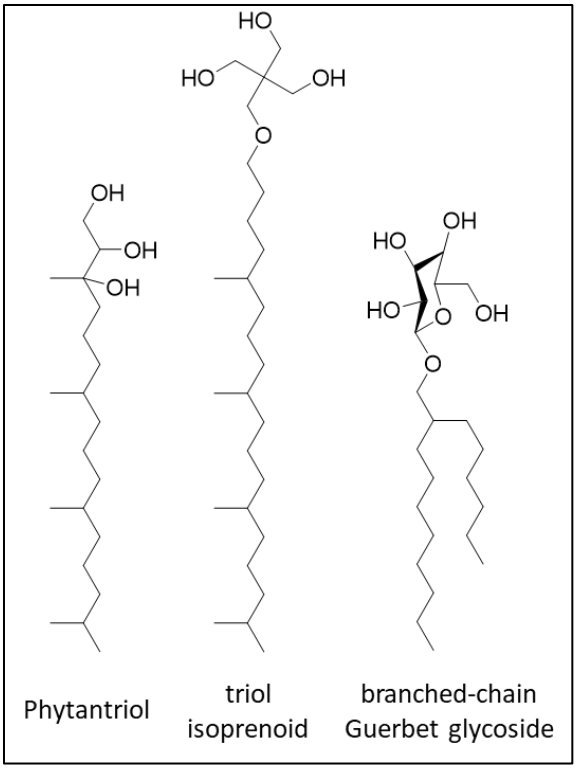

Figure 1.8: Branched-tail amphiphiles that form inverse network phases

Phytantriol forms G_{II} and P_{II} in water (left).[60] The triol isoprenoid studied by Hato and coworkers form D_{II} (middle).[61] The branched-chain Guerbet glycoside studied by Brooks, *et al.* formed G_{II} in excess water (right).[62]

double bond (molecules from lowest to highest chain splay: monoelaidin, ME; monovaccenin, MV; monoolein, MO; and monolinolein, ML) resulted in phases with higher negative mean curvature. Monoolein, in particular, had almost completely destabilized L_α in favor of a wide G_{II} window and forms D_{II} in excess water (Figure 1.7).

Tail branching can be used as an alternative way to create packing frustration. Phytantriol (Figure 1.8), a commonly used ingredient in cosmetic products, is known for forming inverse G_{II} and P_{II} phases when mixed with water.[60] The tail of Phytantriol, classified as an isoprenoid chain, has periodically positioned methyl branches. Hato and coworkers synthesized a group of isoprenoid compounds (Figure 1.8) with varied tail lengths and hydrophilic headgroup moieties such as glycerol and simple sugars.[61, 63-64] They found that the longer tails increased inverse curvature and that balancing the tail length with the right headgroup allowed access to P_{II} and D_{II} network phases. In a study of Guerbet branched-chain β-D-glucosides (Figure 1.8), Brooks, *et al.* systematically varied the length of the tail branches.[62] Similarly, negative mean curvature

increased from disordered normal micelles to L_α to G_{II} to H_{II} as branched tail lengths increased at concentrations of excess water.

1.4.2 Gemini Architectures

The structural design of amphiphiles furnishes a useful tool for accessing network phases. Gin and coworkers observed that cationic ammonium,[65] phosphonium,[66] and imidazolium[67] gemini ("twin head-twin tail") surfactants were more likely to form G_I. Subsequently, Mahanthappa and coworkers showed that anionic dicarboxylate gemini surfactants exhibited wider, more stable G_I windows as compared to their single-tail counterparts.[47] Examples of gemini surfactants that form Type I network phases are shown in Figure 1.9. Molecular dynamics (MD) simulations suggest that the gemini architecture destabilizes L_α in favor of the G_I morphology because of unfavorable headgroup repulsions that drive dimeric amphiphile tail splay.[68] The competition between the favorable cohesive energy of tail packing and the unfavorable repulsion between headgroups creates packing frustrations prompting the "wrinkling" of the flat interface or destabilization of L_α.

In gemini architectures, the linker length is a crucial parameter for controlling the phase behavior.[69] The "gemini effect" turns on when the critical linker length of gemini amphiphiles is shorter than the distance between two headgroups in a system of single-tail equivalents. When the linker length is smaller than the critical linker length, than the headgroups are tethered closer together than naturally preferred causing intramolecular tail splay. Since surface area per headgroup varies with hydration, the critical linker length is also expected to vary with hydration. Mahanthappa and coworkers observed that lengthening the linker from 4 to 6 carbons in a dicarboxylate gemini system led to the

destabilization of the L_α in favor of network phases, which they attributed to the fact that the longer 6-carbon linker enhances the molecular conformational flexibility.[47] In a subsequent study of dicarboxylate gemini surfactants, Mahanthappa and coworkers observed an odd/even effect in the linker length dependence. The H_I phase was destabilized in favor of the G_I phase in systems with odd carbon linkers, suggesting that molecular conformations that both maintain headgroup hydration and tuck the surfactant tails together needed for H_I are not allowed by odd carbon linkers.[41, 70]

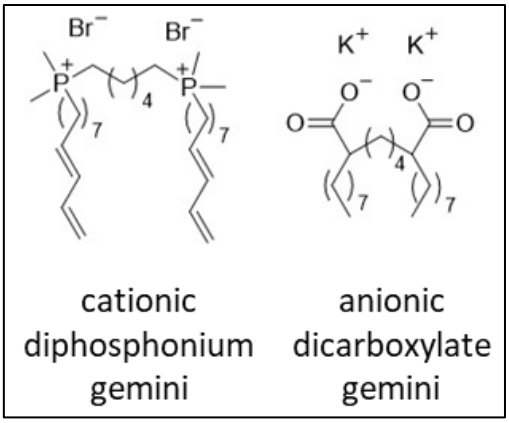

Figure 1.9: Ionic gemini molecules that form network phases

Earlier work by Gin and coworkers showed that cationic diphosphonium gemini formed Type I network phases (left).[66] Subsequent work by Mahanthappa and coworkers showed that an anionic dicarboxylate gemini also stabilized network phases as compared to its single tail counterpart (right).[47]

1.4.3 Effects of Headgroup Interactions

While altering the surfactant architecture and hydrophobic tail structures are viable means for modulating phase behavior and accessing network phase LLCs, headgroup functionality is a more dominant factor in LLC self-assembly because the hydration state of headgroup most strongly depends on the headgroup chemical functionality. Intermolecular hydrogen-bonding among headgroups helps facilitate assembly into certain geometries, often Type II phases. Contrastingly, electrostatic repulsions between headgroups often favors Type I phases.

In a study where Hato and coworkers varied headgroups while leaving the isoprenoid tail constant, they observed that increasing the headgroup size led to flatter inverse curvature in their nonionic systems.[61, 63] This result is predicted by Israelachvili's critical packing parameter estimation.[28, 53] Other than headgroup size, the ability for a headgroup to hydrogen bind also impacts phase behavior in nonionic systems. Drummond and coworkers synthesized a series of urea surfactants with bulky tails (both oleate and isoprenoid) which formed liquid crystalline phases (H_{II}) despite strong intermolecular hydrogen-bonding between urea headgroups which limits their solubility in water.[71] By modifying the urea headgroup with a hydroxy alkyl moiety added to one of the urea nitrogen atoms, they saw improved LLC stability with more mesophases including G_{II} and D_{II}. The added hydroxy alkyl moiety is believed to disrupt intermolecular hydrogen-bonding to open the LLC window, while also increasing the headgroup size leading to flatter curvature.

While the emphasis until now has predominantly been on non-ionic headgroups, examples of network-forming LLCs are also observed in ionic systems. Coulombic interactions are non-selective, long-range, and relatively strong[72] causing them to be a dominant factor in ionic surfactant LLC self-assembly. Early observations of the bicontinuous cubic phases in ionic systems were made by Luzzati and coworkers in potassium soaps.[73-74] Originally thought to be face-centered cubic micellar phases, it was later determined by resolving higher order peaks that these phases were actually the body-centered cubic phase now known as double gyroid.[73, 75] While Luzzati and Husson observed G_I-phase windows of 6-8 wt% in certain potassium soaps (potassium laurate,

potassium myristate, and potassium palmitate); these bicontinuous cubic phases were not observed in their sodium counterparts, suggesting that counterion selection is an important factor in ionic LLC self-assembly.[73] Kunz and coworkers studied carboxylate surfactants varying in 12 to 18 carbon tails with a bulky choline counterion where they observed G_I-phase windows 4-15 wt% wide formed at low hydration (80-97 wt% surfactant).[76] Subsequently, Mahanthappa *et al*. studied the effect of counterions in their dicarboxylate gemini systems by varying the counterion from Na^+ to K^+ to NMe^{4+} (shown in decreasing association).[47] Their findings demonstrated that more highly disassociated counterions favored phases with high curvature; and that the NMe^{4+} dicarboxylate gemini had the widest H_I-phase window and smallest G_I-phase window compared to its Na^+ and K^+ counterparts.

Chapter 2: LLC Phase Behavior of Oleate Salts

2.1 Introduction

At low surfactant concentration, potassium and sodium oleate (soaps) form micelles in aqueous solutions and begin to form cylindrical micelles at slightly higher concentrations.[77-80] Molchanov, *et al*. showed that when cylindrical potassium oleate micelles become entangled that they exhibit viscosities up to six orders of magnitude higher than pure water.[78] This increase in viscosity makes oleate soaps useful as thickening agents. Additionally, potassium oleate has been extensively study for its ability to form microemulsions, thermodynamically stable mixtures of water, oil, and surfactant mixtures, at low concentrations.[81-83] Industrially, sodium oleate is widely used in coating formulations for buildings as a dispersing agent which helps with waterproofing.[84] Potassium oleate is mainly employed as a thickening and emulsifying agent in consumer products and cosmetics and is also used for its ability to raise the melting temperature of flexible parafilms and waxes.[84] Furthermore, the Food and Drug Administration has approved potassium oleate as a regulated food additive.[85]

At higher concentrations, potassium and sodium soaps form normal phase LLCs in water. While phase behavior for potassium and sodium oleate have previously been explored,[73, 86-90] these phase diagrams were either not fully mapped, did not use X-rays to study the phase behavior, or were explored only in multi-component systems. Luzzati and Husson developed more complete phase diagrams for potassium oleate (**K-oleate**), but they were unable to definitively assign phases between H_I and L_α where network phases are commonly observed.[73, 87] Furthermore, an exhaustive literature search yielded no prior studies of the phase behavior of tetramethylammonium oleate (**NMe_4-oleate**), which is less

studied than its metal soap counterparts since NMe_4^+ salts are generally toxic. Hence, having updated and complete phase diagrams of **NMe_4-oleate** and **K-oleate** are needed to understand the effect of oleate-derived gemini surfactants on stabilizing phases with NGC.

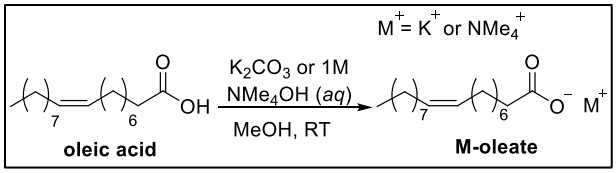

Scheme 2.1: Oleate salt synthesis

K-oleate and **NMe_4-oleate** were synthesized from commercially available oleic acid by stoichiometrically deprotonation with K_2CO_3 and $NMe_4OH(aq)$, respectively.

2.2 Experimental

K-oleate and **NMe_4-oleate** were synthesized by dissolving commercially available oleic acid in methanol and stoichiometrically adding K_2CO_3 and $NMe_4OH(aq)$, respectively (Scheme 2.1). Full details for the synthesis of the oleate salts can be found in Appendix 1.1.

LLC Sample Preparation: Following a procedure previously reported by Mahanthappa and coworkers,[47, 91] ~80 mg samples of the oleate salts were weighed out in a glovebox and sealed in 4 mL scintillation vials. Outside of the glovebox, ultra-pure water (18 MΩ•cm) was added to furnish the desired composition. To achieve homogeneous mixing, the LLC samples were hand mixed and centrifuged (4950 g, 10 minutes) in three cycles. The samples were rigorously sealed and wrapped with parafilm to avoid evaporation. Surfactant concentration is quantified as the wt% surfactant and as mol water per mol surfactant headgroup, w_0. w_0 is a useful measure for comparing relative hydration between surfactants of different molecular weights and number of headgroups per molecule.

Small Angle X-ray Scattering: Small angle X-ray scattering (SAXS) was collected on the synchrotron at the Advanced Photon Source, Sector 12-ID-B at Argonne National Laboratory (Argonne, IL) using a beam energy of 13.297 keV (λ = 0.9322 Å) with a 3.6 m sample-to-detector distance. Silver behenate (d_{100} = 58.38 Å) was used to calibrate all acquired scattering patterns. A Pilatus 2M detector (25.4 cm x 28.9 cm rectangular area) with 1475 x 1679 pixel resolution was used to record 2D-SAXS. Samples were sealed in hermetic alodined aluminum DSC pans which were loaded into a multi-sample array stage and equilibrated at the desired temperature for at least 10 minutes prior to beam exposure. Typical exposures times of 0.1 s were used. Obtained 2D-SAXS patterns were azimuthally integrated using DataSqueeze software package to obtain *I(q)* vs *q* plots.

2.3 Results

Representative 1D-SAXS patterns of **NMe_4-oleate** are shown in Figure 2.1. LLCs with <15 wt% surfactant formed solutions of disordered micelles (dis) for T = 25 – 100 °C. At concentrations from 20 − 25 wt% surfactant, the hexagonally closest-packed spheres structure (HCP, $P6_3/mmc$ symmetry) was obtained with representative unit cell parameters of a = 72.7 Å and c = 118.6 Å at 25 wt%, 25.2 °C. At intermediate hydrations between dis and HCP corresponding to 20 wt% (60.0 °C), dis + LLC coexistence was observed. Hexagonally-packed cylinders (H_I) were observed at concentrations from 28 − 55 wt%. A representative intercylinder distance of 56.5 Å was observed (at 40 wt%, 25.2 °C). At 65 wt% (25.2 °C), a non-birefringent phase with Bragg peaks at q/q^* = √6, √8, √14, √16, and √20, assigned as double gyroid (G_I), was obtained with a = 101.4 Å. At 60 wt% (25.2 °C), small region of H_I + G_I coexistence was observed between the hydrations of the pure

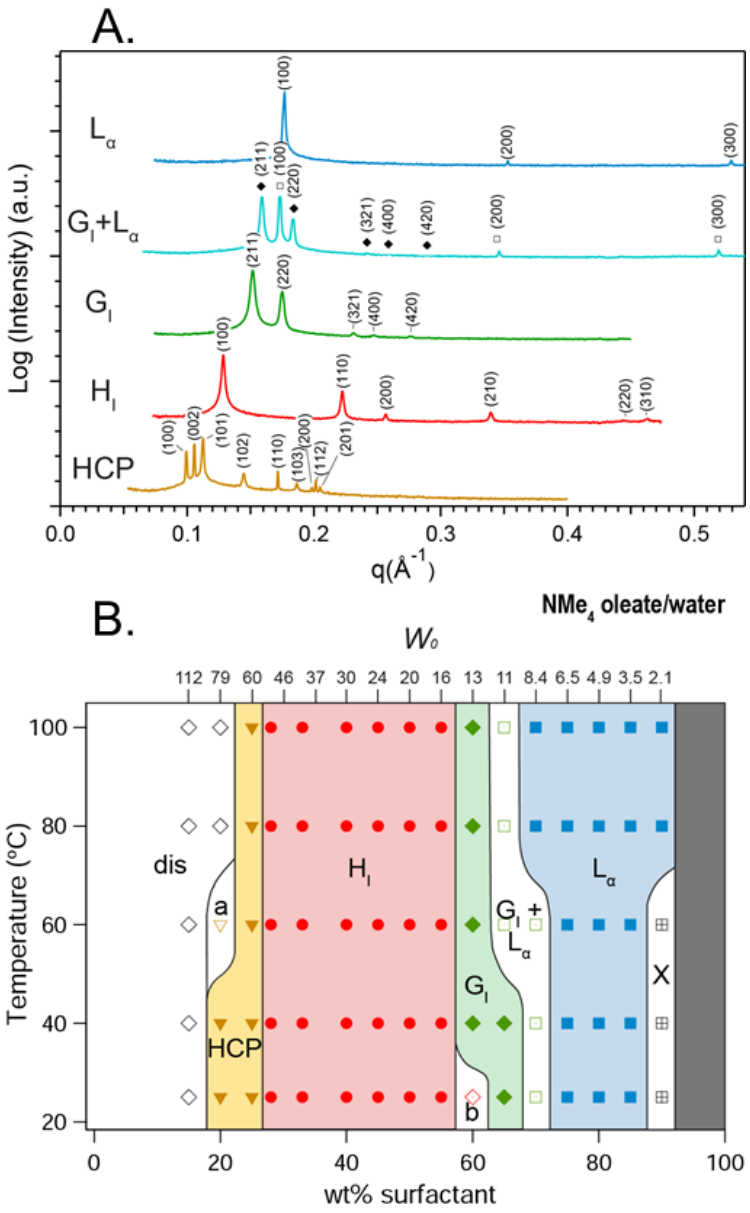

Figure 2.1: Representative SAXS patterns and phase diagram for **NMe$_4$-oleate**

A. Representative 1D SAXS patterns for **NMe$_4$-oleate** of hexagonally closest-packed (HCP, 25 wt%, 25 °C), hexagonally-packed columns (H_I, 40 wt%, 25 °C), double gyroid (G_I, 65 wt%, 25 °C), G_I (◆) + L_α (□) (65 wt%, 80 °C), and lamellar (L_α, 80 wt%, 25 °C). **B.** Phase diagram of **NMe$_4$-oleate**/water system constructed from SAXS data plotted as temperature *versus* weight percent (wt%) surfactant. The top axis represents a conversion from wt% to w_0 (mol of surfactant per mol of water). The observed phases are disordered micelles (dis), HCP, H_I, G_I, L_α, disordered + LLC coexistence (a), H_I + G_I (b), and crystalline + LLC coexistence (X). While regions of coexistence should manifest between two pure phases, the resolution of data points collected is not small enough to observe all regions of coexistence.

phases. At concentrations from 75 − 85 wt% surfactant, a lamellar region (L_α) with a representative spacing of 35.5 Å (at 80 wt%, 25.2 °C) was seen. At 75 wt% (25.2 °C), a significant region of $G_I + L_\alpha$ coexistence was observed between the hydrations of the pure phases. At the lowest investigated hydrations, samples exhibited strong wide-angle X-ray scattering (WAXS) peaks indicating coexistence of crystalline surfactant with LLC phases (X). The 1D-SAXS data was used to construct a phase diagram for **NMe_4-oleate** (Figure 2.1 B). While regions of coexistence should manifest between two pure phases, the resolution of data points (5 wt% increments) is not small enough to observe all regions of coexistence. The general phase progression of L→G→H→HCP→dis with increasing hydration suggests these phases are Type I because curvature is increasing with hydration.

Figure 2.2 shows the phase diagram constructed from 1D-SAXS patterns for **K-oleate**. Below 15 wt% at 27.1 °C, disordered micelles were observed. At concentrations from 40 − 50 wt%, H_I was obtained with a representative intercylinder distance of 60.1 Å (at 40 wt%, 27.1 °C). In the region between disordered micelles and H_I (20 − 35 wt%), there is a region of dis + H_I coexistence. At concentrations from 70-75 wt%, there is a lamellar region (L_α) with a representative spacing of 38.3 Å (at 70 wt%, 27.1 °C). Between hydrations of the pure H_I and L_α, 55 − 65 wt%, a region of unassigned phases (c) is observed (discussed in detail below). Finally, at the highest investigated concentrations of surfactant, a region of solid crystalline and LLC coexistence (X) is observed indicated by strong peaks in the WAXS region. Similar to **NMe_4-oleate**, the phase progression of L→H→dis with increasing hydration suggests these are normal phases for **K-oleate**.

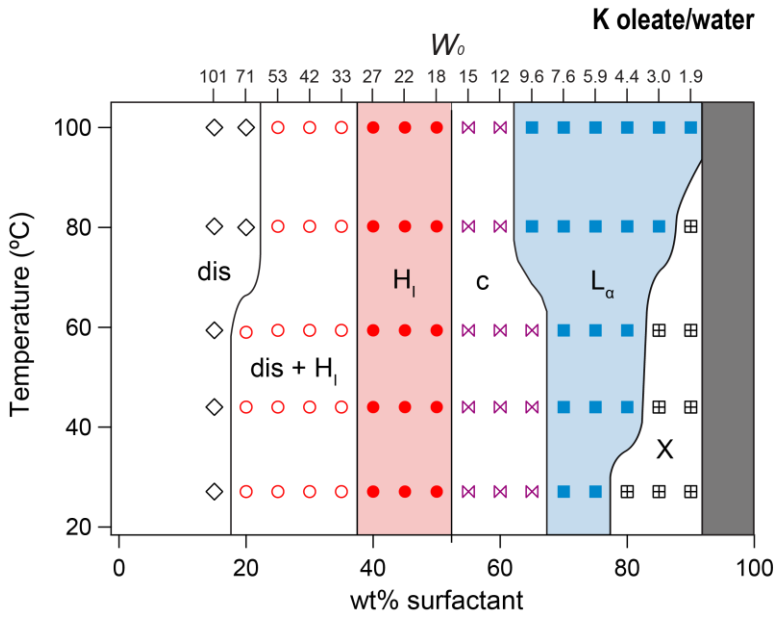

Figure 2.2: Phase diagram for **K-oleate**

Phase diagram of **K-oleate**/water system constructed from 1D SAXS data plotted as temperature *versus* weight percent (wt%) surfactant. The top axis represents a conversion from wt% to w_0 (moles of surfactant per moles of water). The observed phases are disordered micelles (dis), hexagonally-packed columns (H_I), double gyroid (G_I), lamellar (L_α), crystalline + LLC coexistence (X), disordered + hexagonally-packed columns coexistence (dis + H_I), and a region of unassigned phases (c).

Lattice parameters can be obtained from the location of q^* in the SAXS patterns. The L_α *d*-spacing for the oleate salts are shown in Figure 2.3 (A). For both oleates, the *d*-spacings increase linearly with increasing w_0. At comparable hydrations ($w_0 \approx 6$), **K-oleate** has a larger *d*-spacing than **NMe_4-oleate**. Similarly, the intercylinder distance for H_I increases monotonically for both oleates and **K-oleate** has a larger intercylinder than **NMe_4-oleate** at similar hydrations (Figure 2.3 B).

2.4 Discussion

2.4.1 Effects of Counterion on Oleate Phase Behavior

NMe4-oleate had large H_I and L_α windows, a relatively narrow G_I window, and an unexpected HCP window. HCP has previously been seen in nonionic $C_{12}EO_8$ (Brij®) surfactant,[92] cationic alkyl-trimethylammonium surfactant,[93] and anionic malonate surfactants.[94] These previously reported ionic systems have highly disassociated counterions which favors higher positive curvature. The narrow gyroid window in **NMe4-oleate** is not surprising, as the known G_I-phase window in single-tail ionic surfactants is usually less than 10 wt%.[76, 95] Single-tail surfactants typically prefer to pack into phases with constant mean curvature so that the headgroups are equally hydrated.

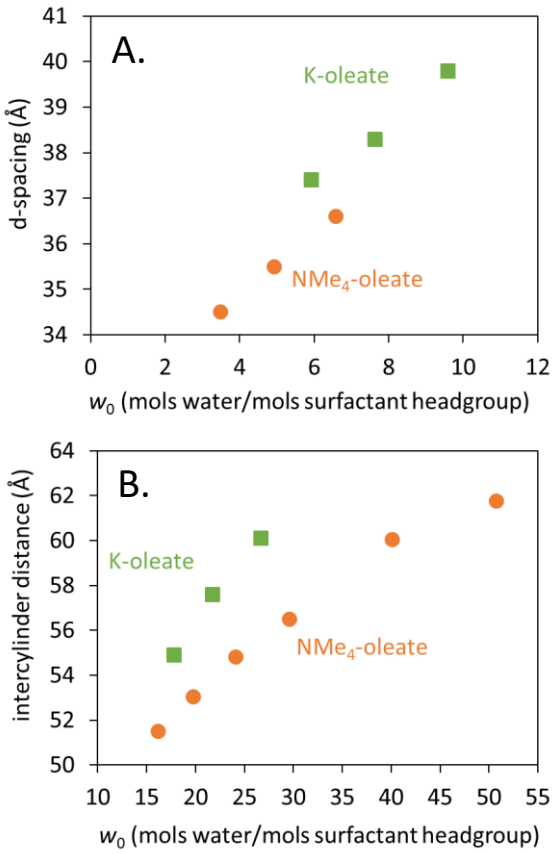

Figure 2.3: Lattice parameters for oleate salts

A. Plot of L_α *d*-spacing as a function of w_0. **B.** Plot of H_I intercylinder distance as a function of w_0.

The more associated K^+ counterion shifts the phase diagram slightly in favor of flatter curvature. While **K-oleate** and **NMe4-oleate** both exhibited large H_I and L_α phase windows, the HCP phase has completely disappeared in **K-oleate** and the pure H_I phase window shrunk in favor of dis + H_I coexistence. Finally, **K-oleate** had a slightly wider crystalline window than **NMe4-oleate**.

This general assessment of **K-oleate** phase behavior is in good agreement with the work of McBain and Sierichs,[90] who mapped the phase diagram with polarized light microscopy; as well as Luzzati and Husson[73] and then later Eins.[87] These authors also struggled to assign the phases in the region labeled c and deemed these as "intermediate phases". Luzzati and Husson[73] had proposed four possible phases: 1) deformed hexagonal, 2) rectangular (ribbon), 3) complex-hexagonal, and 4) isotropic cubic; however, assigning these phases remained ambiguous due to the quality of X-ray data. Luzzati and coworkers assigned one of these intermediate phases as a primitive rectangular (*pmm*).[96] Using electron micrographs, Eins dismissed deformed hexagonal and cubic phases, but found the rectangular phase and deemed the complex-hexagonal phase to be plausible.[87] Later work by Hagslätt, *et al*. argued that this pattern was more likely to be a centered rectangular (*cmm*) ribbon phase.[97]

While the assignment of a ribbon phase seems plausible for one of the patterns collected in this study (see Appendix 1.2.4 for more discussion of the ribbon phase), most of the SAXS patterns in region c cannot be indexed with either a primitive or centered rectangular unit cell. In preliminary efforts to assign phases in region c, one of the patterns was indexed with a tetragonal unit cell (a = 156.3 Å, c/a=1/√2, 57.5 wt%, 70 °C, after thermal annealing at 60 °C for 1.5 hours) as shown in Figure 2.4 A. It seems likely that this could be a network based on its existence between H_I and L_α and its birefringent texture (Figure 2.4 B). However, the broadness of the peaks and the shoulder after the (321) peak suggests that this pattern may not be a pure phase.

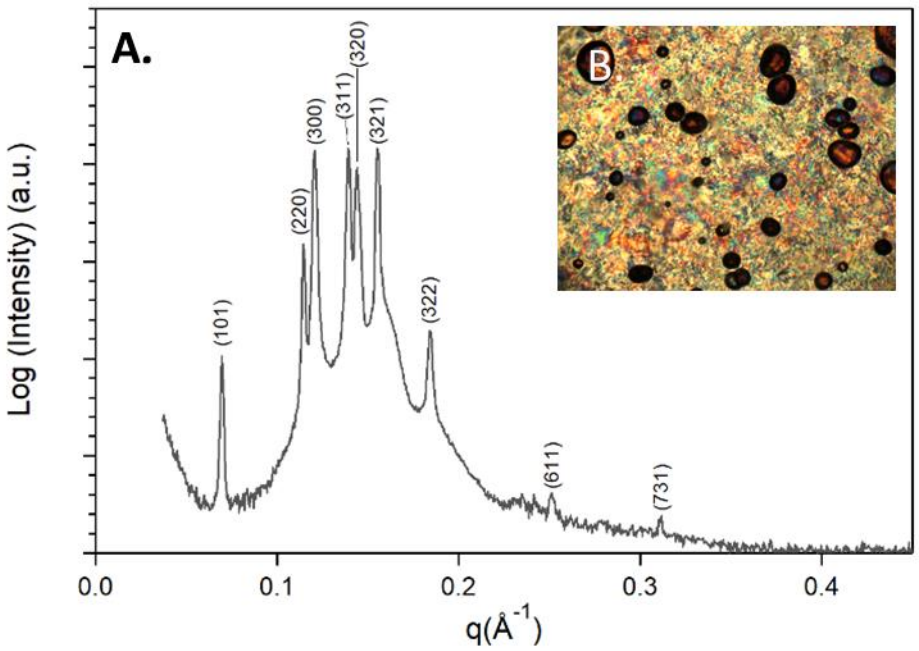

Figure 2.4: 1D SAXS pattern of **K-oleate** at 57.5 wt% and 70 °C

A. The pattern was obtained after thermally annealing samples at 60 °C for 1.5 hrs. The pattern is tentatively indexed with a tetragonal unit cell (a = 156.3 Å, c/a=1/√2).

B. The image was obtained using POM after thermally annealing samples at 60 °C for 1.5 hrs. The sample appears birefringent. The dark spots are air pockets.

2.4.2 Effects of Counterion on Surface Area per Headgroup

The surface area per headgroup was calculated at each concentration for pure phases for **NMe_4-oleate** and **K-oleate** (Figure 2.5, calculations shown in Appendix 1.3). For both oleate salts, the area per headgroup increases with hydration. **NMe_4-oleate** has a higher surface area per headgroup at similar hydrations than **K-oleate**. K^+ is a more associated counterion than NMe_4^+ and sits closer to the interface. Therefore, it is better able to screen inter-headgroup repulsions and leads to a lower surface area per headgroup than NMe_4^+.

2.4.3 L_α Structure of Oleate Soaps

While the tail packing of amphiphilic molecules is an important factor in determining the global morphology of LLC systems, few studies have analyzed L_α tail packing. L_α is commonly depicted as a two leaflet, non-interdigitated bilayer and is characterized by its fluid tail packing.[98] In biological membranes, there have been many studies looking at the thermally induced phase transition between the gel phase, L_β and the liquid crystalline phase, L_α.[1, 10-11, 15] This phase transition is marked by the increased mobility of the hydrophobic tails and can be determined by differential scanning calorimetry (DSC) or the disappearance of sharp peaks at larger *q* values with increasing temperature.[98] Luzzati and coworkers describe the potassium soap gel phase as being an interdigitated membrane with the surfactants hexagonally packed in the lamellar plane as observed by a sharp peak corresponding to 4.1 Å.[98]

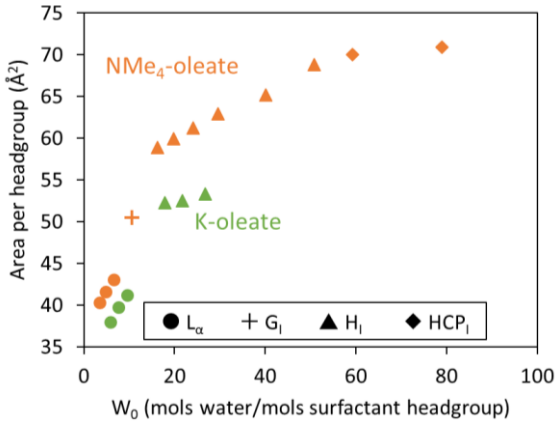

Figure 2.5: Area per headgroup of oleate salts

The area per headgroup for pure LLC phases in **NMe_4-oleate** (orange) and **K-oleate** (green) systems increase with increasing hydration, w_0.

The observed lamellar phases in this study for **TMA-oleate** and **NMe_4-oleate** do not exhibit sharp peaks in the WAXS region, only a broad band at 1.35 $Å^{-1}$ which corresponds to water. Hence, we are confident in the L_α phase assignment rather than another lamellar phase such as L_β (gel phase) or L_c (crystalline phase). The calculated bilayer thickness (25.9 Å for **K-oleate** at 65 wt%) is only slightly longer than the length of a fully stretched oleate chain (19.4 Å), rather than the length of two oleate chains as one

would expect for a L_α bilayer. Thus, it seems likely that that the oleate soaps are forming a partially interdigitated bilayer.

The tails in the partially digitated bilayer have to fill space at a constant density. Using this argument, it is possible to calculate the angle of the tail from the surface normal (see Appendix 1.4 for details). For **K-oleate** at 65 wt%, this angle is 49 °. If we assume that the oleate salts are arranged in a hexagonally packed lattice within the lamellar plane, then distance between headgroups can be calculated from the interfacial area per headgroup (6.9 Å for **K-oleate** at 65 wt%). These parameters have been used to construct a tail packing model for the oleate salt L_α-phase (Figure 2.6). This gives a density in region *y* of 0.71 g/mL and 0.79 g/mL for **NMe_4-oleate** and **K-oleate**, respectively, which compare well the density of nonane at 20 °C (0.72 g/mL).

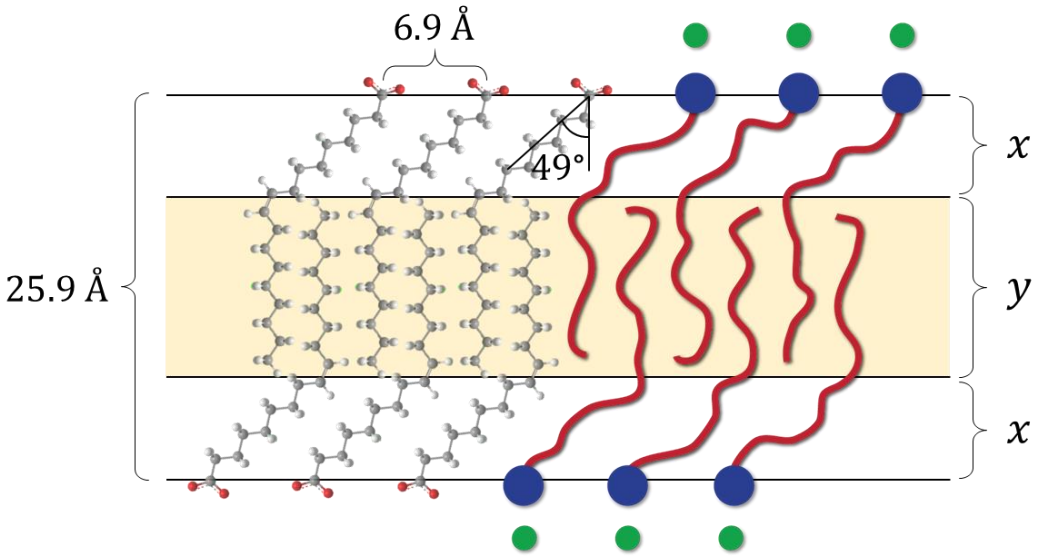

Figure 2.6: Partially interdigitated L_α model

Partially interdigitated bilayer using 3D molecules (left) and a cartoon illustrating L_α tail fluidity (right) for **K-oleate** at 65 wt% with a bilayer thickness of 25.9 Å, a distance between headgroups of 6.9 Å, and a tail angle from surface normal of 49 °.

Anhydrous **K-oleate** forms a non-interdigitated L_c bilayer where d = 44 Å[99] which is slightly larger than two times the fully stretched end-to-end oleate tail length (19.4 Å). As hydration increases, the counterions become more associated and the distance per head group increases, implying a greater area per headgroup. In order to maintain an ideal hydrophobic density, the bilayer thickness must decrease. Hence, the sample adopts a partially interdigitated bilayer. As hydration increases further, the tail angle relative to the surface normal increases resulting in a further reduction of the bilayer thickness (Figure 2.7 A). From this, we learn that the L_α tail packing and bilayer thickness are dependent on headgroup hydration (Figure 2.7 B). However, the relationship between the tail angle and hydration does not appear to be counterion dependent.

The proposed model for the interdigitated L_α bilayer is characteristic of oleate salts. However, neither monoolein with a lipid bilayer of 38 Å[100] nor the cardiolipin sodium salt with a lipid bilayer of 40 Å[101] seem to form an interdigitated membrane. Furthermore, the bilayer thickness of monoolein does not appreciably change with hydration.[100] From the partially interdigitated model (Figure 2.6), it appears that one of the carbonyl oxygens lies along the interface. Perhaps, monoolein, unlike the oleate salts, is unable to form a partially interdigitated membrane because it is energetically unfavorable for its bulky headgroup to sit along the interface. Thus, the headgroup forces monoolein to adopt conformations that orient the headgroup perpendicular to the surface. Additionally, the non-ionic monoolein headgroups are able to pack closer together than the oleate salts. Monoolein has an interfacial area per headgroup of 31 $Å^2$ as compared to oleate salts at ~40 $Å^2$.[100] Whereas, the partially interdigitated membrane allows oleate salts to have a tighter tail packing than

a non-interdigitated membrane while maintaining a relatively large distance between headgroups.

2.5 Conclusions

Tetramethylammonium oleate/water and potassium oleate/water systems were studied by SAXS to determine their LLC behavior. The **NMe_4-oleate** exhibited only narrow G_I-phase windows and **K-oleate** did not exhibit an assignable network phase window. We hypothesize that the oleate salts relieve packing frustration between headgroup repulsions and cohesive energy of the tails by forming a partially interdigitated bilayer. SANS experiments in which a segment of the tail is deuterated are needed confirm the existence of a L_α interdigitated bilayer and could offer more insight into lamellae tail packing.

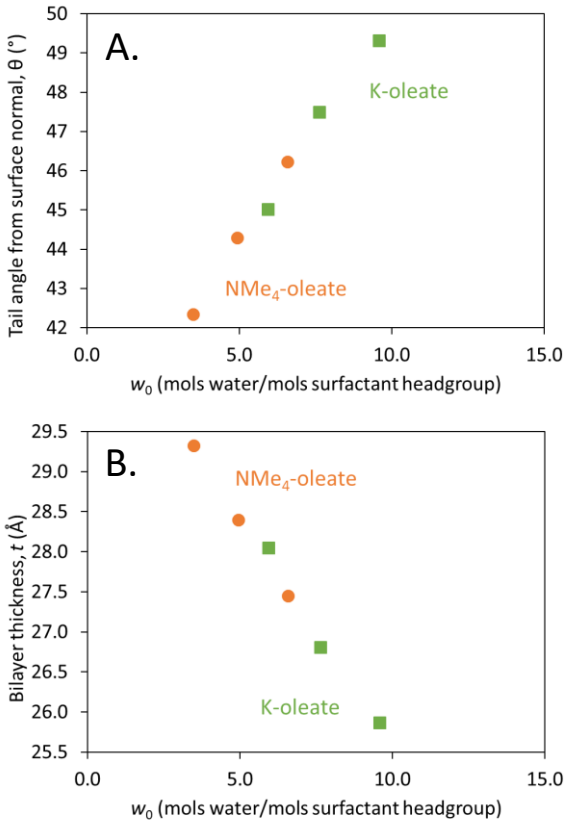

Figure 2.7: Tail splay and bilayer thickness of oleate salts

Tail splay from surface normal (A) and bilayer thickness (B) as a function of hydration for **K-oleate** (■) and **NMe_4-oleate** (●).

The gemini architecture has been shown to cause tail splay due to intramolecular headgroup repulsion.[47, 68] We hypothesize that the network phase window for both **NMe_4-oleate** and **K-oleate** could be expanded by changing the architecture from a single-tail surfactant to that of a gemini surfactant. The single-tail surfactants have relatively more

degrees of freedom and, thus, prefer to form phases with constant mean curvature so that each headgroup is equally hydrated. The gemini architecture may disfavor the partially interdigitated bilayer, which is a highly cooperative tail packing arrangement in favor of network phases that exhibit NGC.

Chapter 3: Synthesis and LLC Phase Behavior of an Oleate Gemini Surfactant

3.1 Introduction

Gemini or dimeric surfactants are two single-tail surfactants covalently linked near the headgroups. They have gained a lot of attention for their ability to lower the critical micelle concentrations (cmc) and are more efficient at lowering the surface tension of water than their single-tail counterparts.[102-103] In Chapter 1, the gemini architecture was introduced as a means for widening LLC G_I window.[47, 66-68] Additionally, gemini dicarboxylate surfactants are known to form a less commonly observed triply periodic continuous phase with hexagonally symmetry, H_I[193].[42] Recently Mahanthappa and coworkers have showed that blending as little as 20 mol% of a gemini into its single-tail counterpart widens the network phase window substantially. They argue that even small loadings of gemini surfactant stabilize negative Gaussian curvature (NGC) by localizing at the saddle points.[91]

Cis-unsaturated lipids compared to their saturated counterparts are known to display reduced L_α to L_β phase transition and to increase the tendency for bilayer lipids to form non-bilayer structures.[104] A particular case of this is the 18:1 (the first number denotes the number of carbons in the tail, the second number denotes the number of unsaturations) oleate tail, which has a 9,10-*cis*-unsaturation. The *cis*-unsaturation creates chain splay within the tail and disrupts hydrocarbon tail packing by virtue of its non-linear shape.[104] Oleate tails are found in naturally occurring lipids such as monoolein, cardiolipin, and DOPC. Monoolein has been extensively studied due to its ability to form stable LLC inverse network phases over wide composition windows that are particularly useful in drug delivery and protein crystallization.[58] In this work, we demonstrate a viable synthetic route

to a gemini dicarboxylate surfactant with *cis*-unsaturated, long tails which we hypothesize will be inclined to stabilize NGC.

3.2 Oleate Gemini Synthesis via Olefin Metathesis

3.2.1 Experimental

Oleic acid gemini, **4**, was synthesized from 10-undecenoic acid in four steps shown by Scheme 3.1. Laboratory notebook pages for each step can be found in Table A2.1 of the Appendix.

Materials: All materials and reagent grade solvents were purchased from Sigma Aldrich (Milwaukee, WI) and used as received unless otherwise noted. 1,6-dibromohexane was distilled over CaH_2 and stored under $N_2(g)$ away from light. Diisopropylamine and hexamethylphosphoramide (HMPA) were distilled from CaH_2 and stored under $N_2(g)$. Anhydrous, anaerobic THF was obtained by sparging analytical grade solvent with $N_2(g)$ for 30 min, followed by cycling through a column of activated alumina in a Vacuum Atmosphere Solvent purification system. *n*-Butyllithium (*n*-BuLi) (2.79 M in hexanes) was titrated using diphenylacetic acid in anhydrous, anaerobic THF prior to use and stored under $N_2(g)$ at 8 °C. Dry methanol was obtained by distilling methanol over Mg turnings and I_2 and stored under $N_2(g)$. Benzoquinone was purified by sublimation at 22 °C and stored away from light at 8 °C. Hoveyda-Grubbs 2nd Generation catalyst (HG2) was stored in a glovebox under argon at 8 °C.

Molecular Characterization: ^{1}H NMR has been previously described in section 2.1.1. Electron spray ionization time-of-flight mass spectrometry (ESI/TOF-MS) was performed on a Bruker BioTOF II. The *m/z* range was 100-1000 Da. For carboxylic acids, the negative

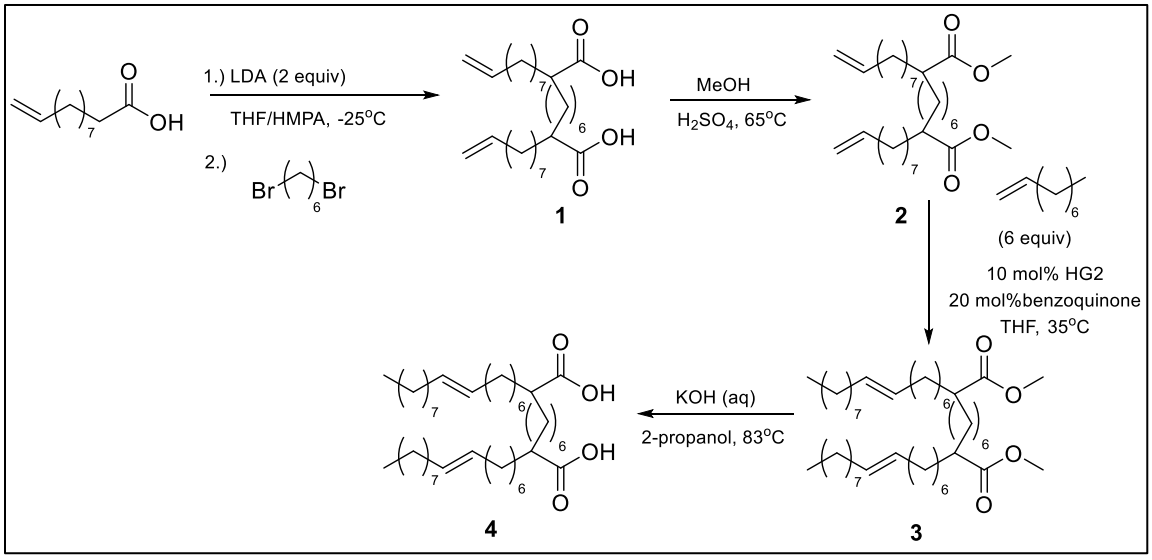

Scheme 3.1: Olefin metathesis route to oleate-derived gemini

Synthesis of an oleate gemini dicarboxylate, **4**, from 10-undecenoic acid in four steps. The metathesis reaction results in 84% trans-olefin (determined from ^{1}H NMR).

ionization mode was used. All other compounds were analyzed in positive ionization mode. The solvent used was MeOH:$CDCl_3$ (2:1).

Synthesis of 2,9-di(oct-7-en-1-yl)decanedioic acid (1): Following a procedure previously reported by Sorenson *et al.*,[47] a 500 mL 2-necked round bottom flask was charged with a stirbar and fitted with an addition funnel. The reaction flask and addition funnel were pump-purged three times and left under $N_2(g)$. Diisopropylamine (15.7 mL, 112 mmol) and dry THF (100 mL) were added to the reaction vessel. The solution was cooled to -25 °C using an ethanol/water/dry ice bath (~30 min), and *n*-BuLi (39.1 mL of a 2.79 M solution in hexanes, 109 mmol) was added dropwise *via* an addition funnel, followed by a THF rinse (8 mL). The reaction mixture was stirred for 30 min, after which a solution of 10-undecenoic acid (10.0378 g, 54.47 mmol) in THF (30.0 mL) was added dropwise *via* addition funnel, which was then rinsed with THF (6 mL). The reaction mixture was stirred for 30 min, after which HMPA (9.50 mL, 54.6 mmol) was added dropwise by syringe,

followed by a THF rinse (6 mL). The reaction was warmed to 22 °C, and allowed to stir for 30 min. The reaction mixture was then cooled back down to -25 °C and 1,6-dibromohexane (4.20 mL, 27.2 mmol) was added dropwise *via* addition funnel, which was then rinsed with THF (6 mL). The reaction was warmed to 22 °C and stirred overnight. The reaction was quenched by adding 2 M HCl(*aq*) (126 mL) and allowed to stir before transferring to a separatory funnel. The aqueous and organic layers were separated, the aqueous layer was extracted with diethyl ether (3 x 50 mL), and the combined organic layers were washed with 2 M HCl (3 x 50 mL), DI H_2O (1 x 50 mL), and saturated NaCl(*aq*) (1 x 50 mL). The pH of organic layers was neutral. After drying over $MgSO_4$(*s*), all volatiles were removed under vacuum. The crude solid was purified by recrystallizing from hot EtOH (23 mL). Yield: 8.4488 g (68.8%). ^{1}H NMR: (400 MHz, DMSO-d_6) δ (ppm): 5.78 (ddt, 2H), 4.98 (ddt, 2H), 4.91 (ddt, 2H), 2.16 (m, 2H), 1.99 (dt, 4H), 1.50-1.15 (m, 38H).

Synthesis of 10,17-dimethoxycarbonyl-1,25-hexacosadiene (2): Following a procedure previously reported by Sorenson,[30] **1** (5.2954 g, 11.758 mmol) was dissolved in dry methanol (60 mL) in a 250 mL round bottom flask under N_2(*g*). The reaction mixture was heated to 50 °C and stirred until **1** dissolved. Concentrated H_2SO_4 (55 µL) was added and the flask was fitted with a water-cooled reflux condenser. After refluxing overnight under N_2(*g*), the reaction mixture was cooled. $NaHCO_3$ (~0.5 g) was added to neutralize the solution. Then, the mixture was concentrated using a rotary evaporator. The resulting oil and excess $NaHCO_3$ was transferred to a separatory funnel using diethyl ether (50 mL) and DI water (50 mL) and the two layers were separated. The aqueous layer was extracted with

ether (3 x 50 mL) and the combined organic layers were washed with saturated $NaHCO_3(aq)$ (3 x 50 mL), water (50 mL), and saturated NaCl(*aq*) (50 mL). After drying over $MgSO_4(s)$, all volatiles were removed under vacuum resulting in a slightly yellow oil. This compound was used without further purification. Crude yield: 5.159 g. ^{1}H NMR: (400 MHz, $CDCl_3$) δ (ppm): 5.81 (ddt, 2H), 4.99 (ddt, 2H), 4.92 (ddt, 2H), 3.67 (s, 5H), 2.32 (m, 2H), 2.03 (m, 4H), 1.70-1.15 (m, 38).

Synthesis of dimethyl 2,9-di(hexadec-7-en-1-yl)decanedioate (3): Following a procedure adopted from Grubbs and coworkers,[105-106] **2** (0.1730 g, 0.3614 mmol) was weighed into a 25 mL Schlenk reaction tube and charged with a stirbar. The reaction vessel was pump-purged with $N_2(g)$ three times. Benzoquinone (0.0232 g, 0.214 mmol) and 1-nonene (0.40 mL, 2.3 mmol) were added to **2**. The reaction vessel was stirred under a $N_2(g)$ purge and heated to 35 °C. In the glovebox, HG2 (0.0580 g, 0.0926 mmol) was weighed into a 25 mL Schlenk reaction tube charged with a stirbar. On a vacuum line, the catalyst was dissolved in dry THF (0.80 mL, divided into 3 parts) and transferred to reaction vessel *via* syringe. After 4 h, the reaction vessel was removed from heat and quenched with cold ethyl vinyl ether (~27 µL). After stirring for 5 min, all volatiles were removed under vacuum to give a dark green oil, which was purified by silica gel chromatography (100% hexanes, then switching to 2% EtOAc in hexanes, then switching to 5% EtOAc). All volatiles were removed under vacuum to afford a clear, colorless oil which was purified by a second silica gel chromatography column (2.5% EtOAc in hexanes) and afforded a clear, colorless oil. Yield: 0.17 g (64% over 2 steps). TLC: R_f = 0.50 (in 10% ethyl acetate in hexanes). ^{1}H NMR: (400 MHz, $CDCl_3$) δ (ppm): 5.38 (m, 4H), 3.66 (s, 6H), 2.32 (m, 2H),

1.96 (m, 8H), 1.65-1.10 (m, 57), 0.88 (6H, t). Metathesis conditions such as molarity, time, temperature, inhibitor, and nonene equivalents were varied to try to achieve higher yields and reduce byproducts. Table A2.2 shows the conditions and subsequent yields.

Synthesis of 2,4-di((E)-pent-2-en-1-yl)pentanedioic acid (4): 4 was synthesized following a modified procedure previously reported by Sorenson.[30] 0.0392 g (0.058 mmol) of **3** was transferred to a 50 mL round bottom with hexanes/ethyl acetate (9:1 v/v). All volatiles were removed under vacuum and the flask was charged with a stirbar. Then, **3** was dissolved in 0.7 mL isopropyl alcohol and stirred. Separately, 0.0498 g (0.89 mmol) KOH was dissolved in 0.0741 g DI H_2O. The KOH(*aq*) was added to the reaction vessel and the reaction vessel was fitted with a reflux condenser. The reaction flask was heated to 82 °C and allowed to reflux overnight (12 h). The crude reaction mixture was evaporated until only ~10% of the solvent remained. The crude product was transferred to a separatory funnel using DI H_2O (12 mL) and washed with hexanes (1.5 mL). 1.5 mL 2 M HCl(*aq*) was added to the aqueous layer (pH < 2) and the aqueous layer was extracted with ethyl acetate (3 x 10 mL). The combined organic layers were washed with DI H_2O (1 x 10 mL) and saturated NaCl(*aq*) (2 x 10 mL). After drying over $MgSO_4$, all volatiles were removed under vacuum to afford a white solid. Yield: 0.0331 g (88.0%). ^{1}H NMR: (400 MHz, $CDCl_3$) δ (ppm): 5.38 (m, 4H), 2.33 (m, 2H), 1.96 (m, 8H), 1.65-1.10 (m, 58), 0.88 (6H, t).

3.2.2 Results and Discussion

This synthetic route for an oleate gemini (Scheme 3.1) was initially chosen because we thought it would be modular and would thus allow broad molecular structure variation in addition to providing us *Z*-selectivity at the olefin. The linker length can be changed

from a 6-carbon linker to a 3-, 4-, or 5- carbon linker by substituting the dibromohexane for dibromo- propane, butane, or pentane, respectively. This synthetic route also allows for headgroup and counterion variations. From the oleic acid gemini, **4**, only one additional step is required to make either NMe_4-oleate and K-oleate gemini surfactants or two additional steps would furnish the glycerol headgroup. Finally, the tail length and placement of the unsaturation may be altered by changing the starting materials.

While the route is quite modular, it did not provide the *Z*-selectivity that we had originally anticipated. The first metathesis catalyst that we tried was Grubbs *Z*-selective catalyst; however, this catalyst is sensitive to protic impurities. With the *Z*-selective catalyst, <5% conversion was obtained using crude **2** without further purification and a 60% conversion was obtained after purifying **2** by silica gel chromatography. However, 60% conversion is still quite low compared to HG2 which gives complete conversion without the additional column needed to purify the ester, **2**. While HG2 gives higher conversion, the olefin was determined to be 84% *trans* (^{1}H NMR) (Figure A2.1).

Additionally, removing ruthenium byproducts after metathesis is cumbersome and even small amounts of residual ruthenium could affect the LLC phase behavior. After attempting to remove the ruthenium with activated charcoal and basic alumina, we found that the method that worked best was to run a silica gel chromatography column on the oleate gemini methyl ester, **3**. However, it has been reported that residual ruthenium byproducts may likely still be present after running multiple silica gel chromatography columns.[107] While the residual ruthenium was not quantified for these samples, it could be

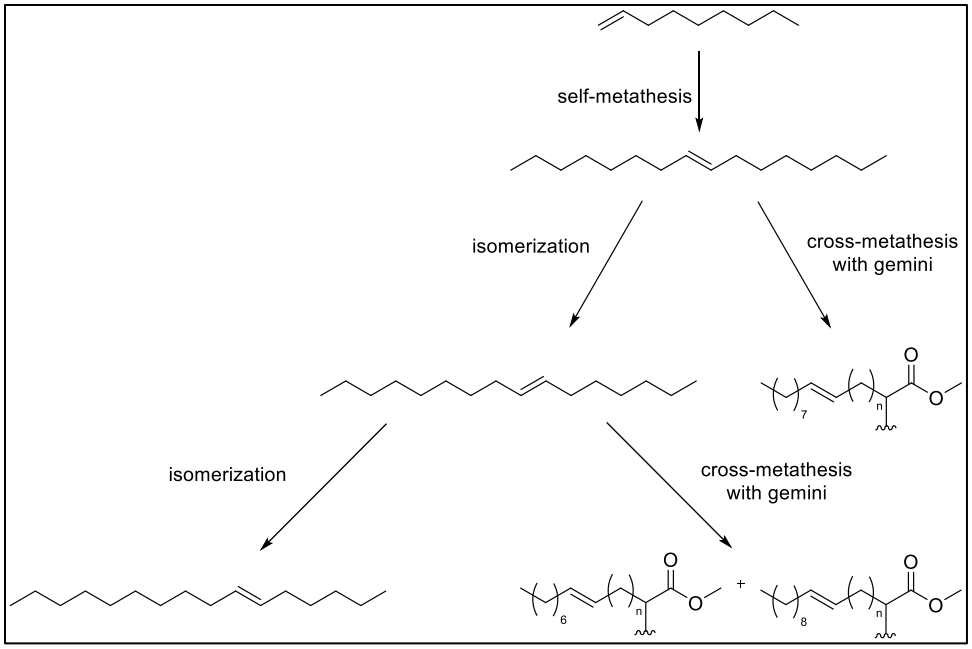

Figure 3.1: Isomerization pathway during olefin metathesis

This isomerization pathway leads to molecular weight dispersity in gemini product during metathesis. Additional isomerization pathways can be found in Appendix 2.1.4 (Figure A2.3).

measured in the future using inductively coupled plasma optical emission spectroscopy (ICP-OES).

Further complications with the metathesis step such as isomerization ("chain walking"), ring-closing metathesis, and coupling byproducts made the synthesis route impractical for studying LLC phase behavior. Figure A2.2 shows the EOS/TOF MS of **4** without the addition of benzoquinone (BQ) in the metathesis step. In the MS, there is a large peak at [M-1] (taken in negative ionization mode) and many smaller peaks that differ in mass by one methylene group both at larger and smaller molecular weights. Figure 3.1 depicts the main pathway for isomerization, in which the double bond in the nonene dimer isomerizes prior to metathesis; however, there are numerous means by which the bond can isomerize to create various products (Figure A2.3). Since isomerization is caused by

ruthenium decomposition into a ruthenium-hydride, 2 mol equivalent (relative to the catalyst) of BQ was added and the reaction time was reduced from overnight to 4 h.[105] Adding BQ to prevent catalyst reduction greatly reduced the degree of isomerization. As shown in the EOS/TOF MS of **3** in Figure A2.4 (red trace), there are only four peaks: a large peak at [M-1], a smaller peak at [M-15], and two small peaks at [M-29] and [M+13] when [Ru]:[BQ] = 1:2. Even though BQ worked well at reducing isomerization, it did not completely eliminate isomerization. Additionally, BQ elutes near the product in silica gel chromatography, making it difficult to separate after metathesis. Next, we tried using tetrafluoro-1,4-benzoquinone (TFBQ) because it is a stronger oxidant than BQ. TFBQ ([Ru]:[TFBQ] = 1:4) reduced isomerization further, resulting in greater than 95% purity after silica gel chromatography (Figure A2.4, black trace). However, yields were still quite low (13.2% over two steps: metathesis and hydrolysis). TLC plates and EOS/TOF MS of the crude reaction mixture and high polarity column aliquots showed that ring-closing metathesis and higher order coupling byproducts were causing low yields of desired product (Figure A2.5).

3.3 K-C19:1 Gemini Synthesis via Wittig Reaction

3.3.1 Experimental

K-C19:1 gemini dicarboxylate salt, **11**, was synthesized from 10-undecenoic acid in six steps shown by Scheme 3.2. Laboratory notebook pages for each step may be found in Table A2.3.

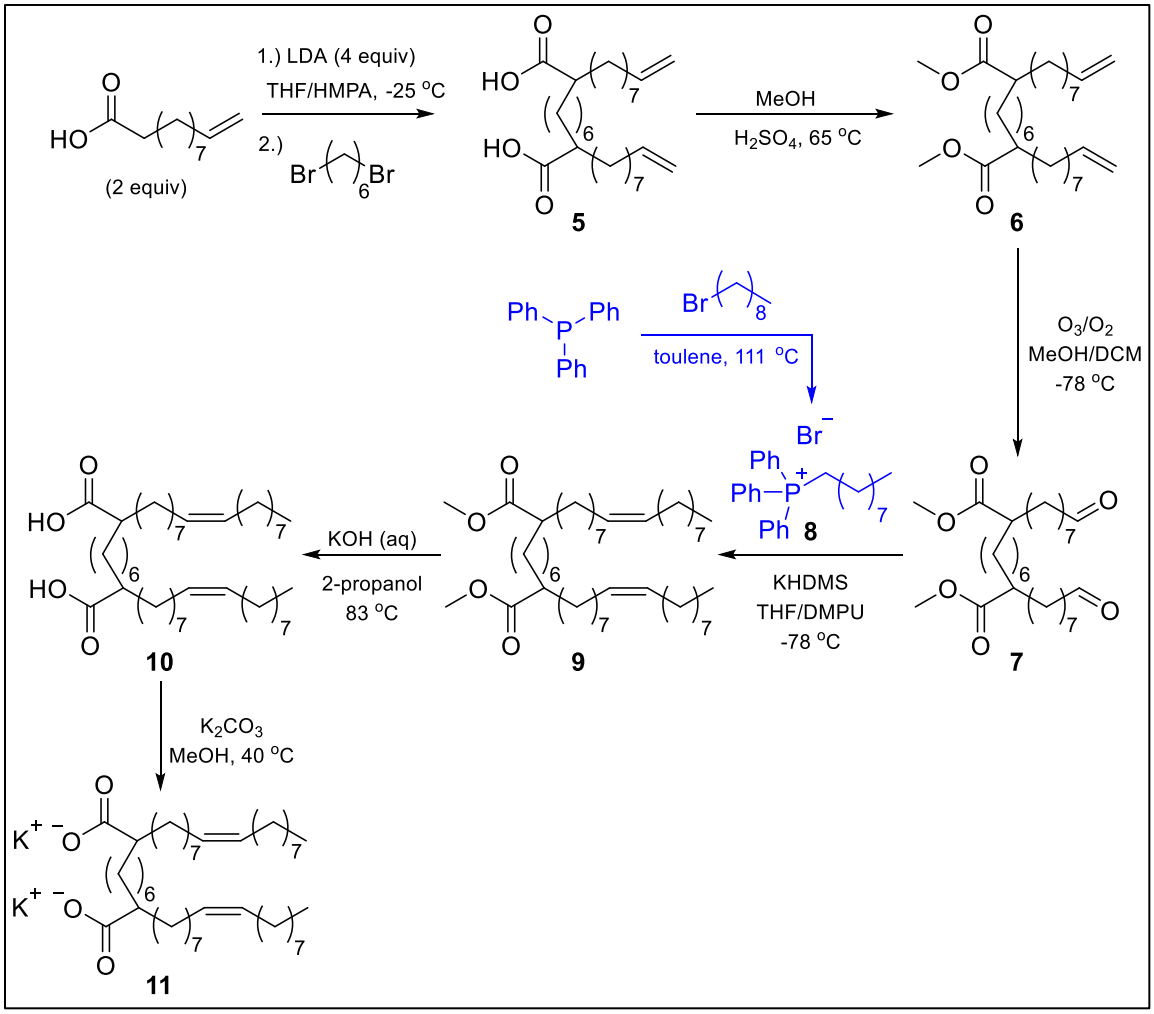

Scheme 3.2: Wittig reaction route to oleate-derived gemini

Synthesis of K-C19:1 gemini dicarboxylate, **11**, from 10-undecenoic acid in six steps. The metathesis reaction results in >95% *cis*-olefin (determined from ^{1}H NMR).

Materials: All materials and reagent grade solvents were purchased from Sigma Aldrich (Milwaukee, WI) and used as received unless otherwise noted. 1,6-dibromohexane was distilled over CaH_2 and stored under $N_2(g)$ away from light. Diisopropylamine and hexamethylphosphoramide (HMPA), and N,N′-Dimethylpropyleneurea (DMPU) were distilled from CaH_2 and stored under $N_2(g)$. Anhydrous, anaerobic THF, DCM, and toluene were obtained by sparging analytical grade solvent with $N_2(g)$ for 30 min, followed by

cycling through a column of activated alumina in a Vacuum Atmosphere Solvent purification system. *n*-Butyllithium (*n*-BuLi) (2.79 M in hexanes) was titrated using diphenylacetic acid in anhydrous, anaerobic THF prior to use and stored under $N_2(g)$ at 8 °C. Dry methanol was obtained by distilling methanol over Mg turnings and I_2 and stored under $N_2(g)$.

Synthesis of 2,9-di(oct-7-en-1-yl)decanedioic acid (5): Following a procedure previously reported by Sorenson *et al*., [47] **5** was synthesized starting from 10-undecenoic acid following the procedure detailed in section 3.2.1 for the synthesis of **1**. Yield: 43.5%. ^{1}H NMR: (400 MHz, $CDCl_3$) δ (ppm): 5.80 (ddt, 2H), 4.99 (ddt, 2H), 4.92 (ddt, 2H), 2.35 (m, 2H), 2.04 (dt, 4H), 1.7-1.1 (m, 36 H).

Synthesis of dimethyl 2,9-di(oct-7-en-1-yl)decanedioate (6): Following a procedure previously reported by Sorenson,[30] **6** was synthesized from **5** using the procedure detailed in section 3.2.1 for the synthesis of **2**. Yield: 90.0%. ^{1}H NMR: (400 MHz $CDCl_3$) δ (ppm): 5.80 (ddt, 2H), 4.99 (ddt, 2H), 4.92 (ddt, 2H), 3.66 (s, 6H), 2.32 (m, 2H), 2.03 (dt, 4H), 1.7-1.1 (m, 36 H).

Synthesis of 2,9-bis(7-oxoheptyl)decanedioic acid (7): Following a procedure previously adapted from Sorenson,[30] 5.04 g (1.05 mmol) of **6** was dissolved in 85 mL methanol:DCM (1:1 v/v) and transferred into a 250 mL gas washing bottle with a fritted cylinder. The reaction solution was cooled to -78 °C using a dry ice/acetone bath. An OREC V Series Ozone System operating at 1.5 amps and 1.5 L/min was used to bubble $O_3/O_2(g)$ into the reaction solution until a pale blue color persisted (~20 min). $O_2(g)$ was bubbled through the solution until the pale blue color faded to remove excess ozone. The reaction solution

was allowed to warm to room temperature and was transferred to a 200 mL round bottom flask charged with a stirbar. Solid thiourea (2.0486 g, 2.7 mmol) was added to the reaction solution and it was stirred overnight (~16 h). The mixture was filtered through Celite and the filtrate was condensed using a rotary evaporator. The resulting yellow oil was dissolved in 100 mL ethyl acetate and transferred to a separatory funnel. To this, 100 mL saturated $NaHCO_3$(*aq*) was added and the organic layer was separated from the aqueous layer. The aqueous layer was extracted with ethyl acetate (3 x 50 mL) and the combined organic layers were washed with DI H_2O (1 x 50 mL) and saturated NaCl(*aq*) (2 x 50 mL). After drying over $MgSO_4$(*s*), all volatiles were removed under vacuum. The crude oil (4.99 g) was dissolved in 72 mL THF and 14.5 mL 1 M HCl was added to convert any dimethyl acetal formed to the desired aldehyde. The reaction was stirred overnight (~16 h). The resulting solution was concentrated by rotary evaporation and the resulting oil was transferred to a separatory funnel with ethyl acetate (50 mL). To this, 50 mL of saturated $NaHCO_3$(*aq*) was added and the aqueous layers were separated from the organic layers. The aqueous layers were extracted with ethyl acetate (3 x 50 mL) and the combined organic layers were washed with saturated $NaHCO_3$(*aq*) (1 x 50 mL) and saturated NaCl(*aq*) (2 x 50 mL). After drying over $MgSO_4$(*s*), all volatiles were removed under vacuum resulting in a pale, yellow oil. This product was used without further purification. Yield: 4.19 g (82.4%).^{1}H NMR: (400 MHz, $CDCl_3$) δ (ppm): 9.78 (s, 1.2 H), 3.66 (s, 6H), 2.42 (t, 2.4H), 2.31 (m, 2H), 1.8-1.1 (m, 36H).

Synthesis of nonyl(triphenyl)phosphonium bromide (8): Following a procedure previously report by Mostyn *et al.*,[108] **8** was synthesized by adding 10.05 g (3.83 mmol)

triphenylphosphine (TPP) to a 250 mL 2-neck round bottom flask charged with a stirbar and fitted with a reflux condenser. Under a $N_2(g)$ atmosphere, 100 mL of anhydrous toluene was added to the reaction vessel and the reaction was stirred to give a cloudy mixture. To this, 7.95 g (3.84 mmol) 1-bromononane was added and the solution became clear, colorless. After refluxing for 72 h, the reaction vessel was allowed to cool to 25 °C and then further cooled to -24 °C. After 4 h, the toluene was decanted off and 50 mL of hexanes was added and the vessel was stirred overnight at 25 °C. The vessel was then cooled to -25 °C for 4 h and the hexanes were decanted off. Remaining volatiles were removed under vacuum affording a white, sticky solid. Yield: 12.18 g (67.7%). ^{1}H NMR: (400 MHz, $CDCl_3$) δ (ppm): 8-7.5 (m, 15 H), 3.87 (dt, 2H), 1.8-1.0 (m, 14H), 0.88 (t, 3H).

Synthesis of dimethyl 2,9-di((Z)-heptadec-8-en-1-yl)decanedioate (9): Following a procedure modified from Mostyn *et al.*,[108] **9** was synthesized by adding 9.68 g (2.06 mmol) of **8** to a 250 mL 2-neck round bottom flask charged with a stirbar and equipped with an addition funnel. **8** was suspended in THF (27.0 mL) and N,N′-dimethylpropyleneurea (DMPU, 2.5 mL) at 0 °C under a $N_2(g)$ atmosphere. Separately, 3.7660 g (1.89 mmol) of potassium bis(trimethylsilyl)amide (KHDMS) was dissolved in THF (19.0 mL) and the KHDMS solution was added to the reaction vessel dropwise at 0 °C. The reaction was allowed to warm to 25 °C and stirred for 40 minutes. The reaction mixture was cooled down to -78 °C using a dry ice/acetone bath. Separately, 4.19 g (0.87 mmol) **7** was dissolved in 27.0 mL THF. The aldehyde solution was added dropwise to the reaction vessel and an additional 10 mL THF was added to rinse the addition funnel. The reaction was stirred at -78 °C for 30 minutes and then allowed to warm to 25 °C. After stirring for

12 h, the reaction was quenched with saturated $NH_4Cl(aq)$ (10.5 mL) to a pH ~7–8. The crude reaction mixture was extracted with DCM (3 x 20 mL) and dried over $NaSO_4(s)$. All volatiles were removed under vacuum to afford a pale orange oil, which was purified by silica gel chromatography (6.5% ethyl acetate in hexanes, then switching to 8% ethyl acetate in hexanes). All volatiles were removed under vacuum to afford a pale, orange oil. ^{1}H NMR showed that some triphenylphosphine oxide (TPPO) remained; product was used without further purification. Crude yield: 2.07 g (33.9%). Purity: 44 mol%. TLC: R_f = 0.68 (in 10% ethyl acetate in hexanes). ^{1}H NMR: (400 MHz, $CDCl_3$) δ (ppm): 5.34 (m, 4H), 3.66 (s, 6H), 2.32 (m, 2H), 2.01 (m, 8H), 1.8-1.1 (m, 60H), 0.88 (t, 6H).

Synthesis of 2,9-di((Z)-heptadec-8-en-1-yl)decanedioic acid (10): This synthesis follows the procedure detailed in section 3.2.1 for the synthesis of **4**, but with the C19:1 gemini instead. Briefly, **9** was hydrolyzed with KOH(*aq*) in isopropanol affording a pale, brown oil. ^{1}H NMR showed that some TPPO remained; product was used without further purification. Crude yield: 83.0%. Purity: 87.1%. ^{1}H NMR (400 MHz, $CDCl_3$) δ (ppm): 5.37 (m, 4H), 2.36 (m, 2H), 1.96 (m, 8H), 1.7-1.10 (m, 60), 0.88 (6H, t).

Synthesis of potassium 2,9-di((Z)-heptadec-8-en-1-yl)decanedioate (11): The potassium gemini salt, **11**, was prepared by dissolving 1.4820 g (0.220 mmol) **10** and 0.2913 g (5.19 mmol) KOH(*s*) in 3.2 mL methanol. The reaction was stirred at 40 °C for 5 h. The reaction solution was then filtered through Celite, all volatiles were removed under vacuum, and the resulting solid was freeze dried from benzene. The resulting slightly brown solid was suspended in 20 mL of DCM, sonicated for 10 min, and cooled to -25 °C for 3 h. DCM was decanted off to remove TPPO impurity and this was repeated 3 more

times until there was no trace of TPPO in the ^{1}H NMR. The resulting tan solid was freeze dried from benzene. Yield: 1.225 g (74.3%). ^{1}H NMR (400 MHz, CD_3OD) δ (ppm): 5.34 (m, 4H), 2.16 (m, 2H), 2.02 (m, 8H), 1.7-1.10 (m, 60), 0.88 (6H, t). ^{13}C NMR (100 MHz, CD_3OD) δ (ppm): 184.1, 129.5, 129.4, 49.5, 33.5, 33.3, 31.7, 29.8, 29.6, 29.5, 29.4, 29.3, 29.2, 29.1, 29.0 28.9, 27.9, 27.8, 26.8, 26.7, 22.3, 13.1. Elemental Analysis Calculated for $C_{44}O_4H_{80}K_2$: C, 70.34; H, 10.73. Found: C, 72.89; H, 11.40.

3.3.2 Results and Discussion

While the route to the oleate gemini via Scheme 3.2 (Wittig route) is slightly longer than the route depicted in Scheme 3.1 (metathesis route), it does offer many benefits compared to the metathesis route. First, the Wittig reaction allows for better control over the regiochemistry of the olefin. A *Z*-specific variant of the Wittig reaction reported by Bestmann, *et al.* which achieves high *Z*-selectivity in THF at low temperatures (-78 °C) was used.[109] From ^{1}H NMR, we see a symmetric peak at 5.34 ppm corresponding to the *cis*-olefin, with no trace of the *trans*-isomer (Figure A2.6). Hence, it appears that we have >95 mol% *Z*-selectivity. Another advantage of the Wittig route is that there are no byproducts caused by isomerization, coupling, or ring-closing metathesis as observed in the metathesis route. Finally, Scheme 3.2 does not require ruthenium catalyst.

While the Wittig route has many advantages over metal-catalyzed olefin metathesis, there is still some optimization needed. TPPO is produced by the Wittig reaction and proves difficult to remove by silica gel chromatography column since it elutes at nearly the same time as the product. While it was shown that TPPO can be removed from the gemini salt, **11**, using multiple DCM washes, it is recommended that TPPO be

removed before the deprotonation step which requires stoichiometric conditions to make **11**. Either column conditions should be optimized to better remove TPPO or washing **10** with a nonpolar solvent may be able to remove most of the TPPO before deprotonation.

The elemental analysis of **11** showed that the gemini dicarboxylate had not been fully deprotonated to form the potassium salt. The extent of the deprotonation is estimated to be between 56 – 68 mol% potassium soap from elemental analysis with the water content of the sample being between 0 – 1.3 mol% (0 – 0.03 wt%). Henceforth, it will be assumed that there was no residual water in the samples after freeze-drying and that the extent of deprotonation is 68 mol%. Small and coworkers showed that it is possible to quantify the extent of ionization, which they did by titrating their oleic acid/K-oleate (acid-soap) samples.[99]

Furthermore, it should be noted that we did not actually form oleate tails. Since the starting material of 9-decenoic acid is more costly than 10-undecenoic acid, we decided to use 10-undecenoic acid to optimize the chemistry and preliminarily explore the phase behavior of the K-C19:1 gemini system. However, this chemistry is modular and the tail length as well as the location of the unsaturation can be controlled by changing the starting materials of 10-undecenoic acid and 1-bromononane. One could even use the Wittig reaction as a handle to include different tail structures such as cyclic tail ends that mimic the lipid tails found in certain thermoacidophilic archaebacteria.[110-113] Additionally, the linker length can be controlled by changing the 1,6-dibromohexane and the counterions can be controlled by changing the base used for deprotonation.

LLC Sample Preparation and Small Angle X-ray Scattering: LLC sample preparation and SAXS measurements were performed as detailed in Chapter 2.2.

3.4 LLC Phase Behavior of Oleate Gemini Acid-Soaps

3.4.1 Results

Representative 1D-SAXS patterns of **11** are shown in Figure 3.2 A. LLCs with < 30 wt% surfactant formed disordered solutions (dis) for T = 25 – 100 °C. At concentrations > 72 wt% surfactant, lamellar phases (L_α) with representative d-spacings of 34.0 Å (at 80 wt%, 25.0 °C) were seen. At intermediate concentrations between dis and L_α (36 − 68 wt% surfactant), dis + L_α coexistence was observed. The 1D-SAXS data was used to construct the phase diagram for **11** shown in Figure 3.2 B.

Lattice parameters can be obtained from the location of q^* in the SAXS patterns. The L_α d-spacings for the **11** are compared with the d-spacings of the oleate salts at similar wt% surfactant and w_0 (Figure 3.3). As the weight percent of **11** increases, the d-spacing decreases until it plateaus at 33.8 Å. Compared to the oleate salts at similar weight percentages and hydrations, **11** has a smaller d-spacing.

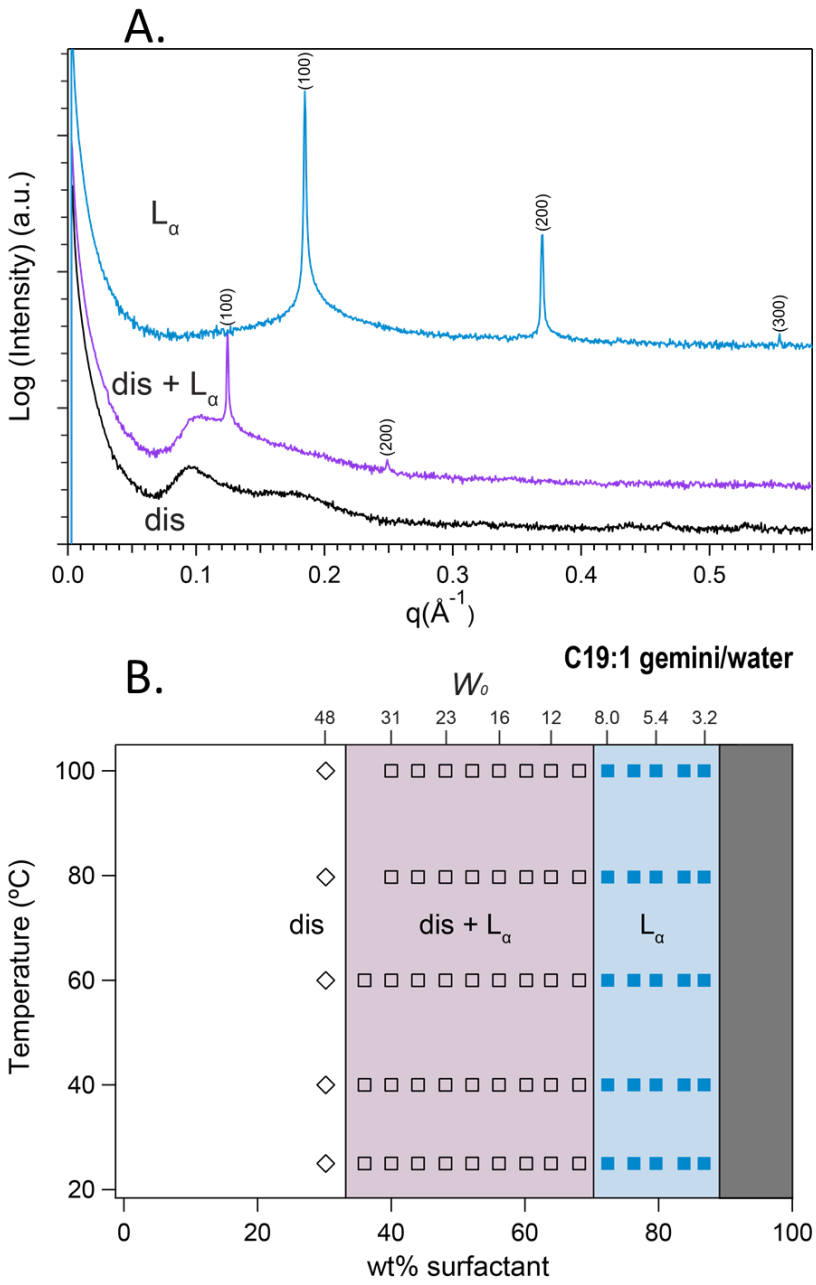

Figure 3.2: Representative SAXS patterns and phase diagram for K-C19:1 gemini

A. Representative K-C19:1 gemini (**11**) 1D SAXS patterns of disordered (dis, 30 wt%, 25 °C), disordered and lamellae coexistence (dis + L_α, 44 wt%, 25 °C), and lamellae (L_α, 80 wt%, 25 °C).

B. Phase diagram of K-C19:1 gemini/water system constructed from SAXS data plotted as temperature *versus* weight percent (wt%) surfactant. The top axis represents a conversion from wt% to W_0 (moles of surfactant per moles of water). The observed phases are dis, dis + L_α, L_α, and crystalline + LLC coexistence (X) in increasing wt% surfactant.

3.4.2 Discussion

The phases adopted by **11** are primarily lamellar, indicating a strong preference for flat curvature as compared to **K-oleate** and **NMe$_4$-oleate**. This flatter curvature coincides well with the elemental analysis which shows that **11** was not fully deprotonated. Hence, this gemini system resembles acid-soap systems of oleic acid/K-oleate/water. Small and coworkers mapped the phase behavior of 1:1 K-oleate/oleic acid systems with changing hydration[99] and, in subsequent work, examined the phase behavior of hydrated acid soaps at different degrees of ionization.[114] The non-ionized (acid) headgroups shield the ionic (soap) headgroups which allow for tighter headgroup packing and lower positive curvature. In the 1:1 K-oleate/oleic acid system, Small and coworkers observed H_{II} at low hydrations and L_α at the highest investigated hydrations with a region of coexistence in between the two phases[99] suggesting that the ionization of **11** is between that of the 1:1 acid-soap and fully ionized soap.

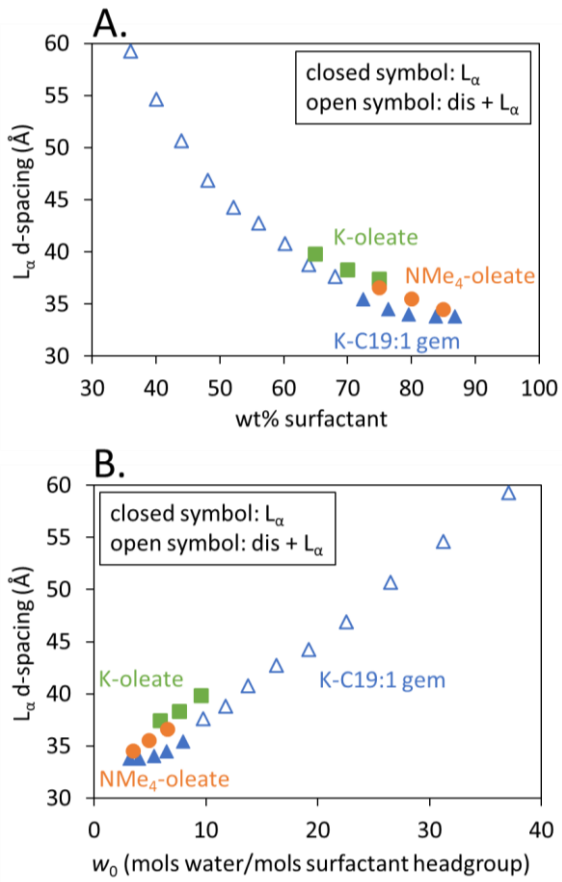

Figure 3.4: Lα *d*-spacings for K-C19:1 gemini

K-C19:1 gemini (**11**) surfactant's pure Lα *d*-spacing (▲) and dis + Lα (△) are compared with **K-oleate** (■) and **NMe$_4$-oleate** (●) at similar concentrations, wt% surfactant (**A**) and at similar hydrations, w_0 (**B**).

At low concentrations (<30 wt%), **11** forms a disordered phase in water. At slightly higher concentrations, a large window of disorder + L_α is formed. We believe that this region is disordered vesicles, or liposomes. Since liposomes are large enough to scatter light, these samples appear opaque with a slightly blue tinge while micellar solutions are clear, colorless solutions. In our samples, it is difficult to evaluate the opacity of these samples because they are brown. Nevertheless, it has been reported that K-oleate/oleic acid (1:1 acid-soap) mixtures form unilamellar and multilamellar vesicles; [99, 114] hence, we believe that at low concentrations **11** forms vesicles as well.

The area per headgroup was calculated for the pure L_α phases of **11** and were compared to **K-oleate**, **NMe_4-oleate**, and K-oleate/oleic acid (1:1) data from Small and coworkers[99] (Figure 3.4). While the K-oleate/oleic acid (1:1) system has a much lower area per headgroup than either oleate soap at similar hydrations as would be expected for a partially ionized system, the gemini (**11**) showed a higher surface area per headgroup than either oleate salt. The average distance between headgroups for **11** is 6.4 Å at w_0 = 7.4, assuming a hexagonally closed packing of headgroups within the lamellar plane. This distance between headgroups is significantly smaller than that of a fully stretched, *trans* zigzag 6-carbon gemini linker, 8.8 Å. Hence, it appears that the linker is pushing the linked headgroups apart. The surface area per headgroup for the gemini should reflect an average of the intermolecular headgroup distance and the intramolecular headgroup distance. The bilayer thickness of **11** is comparable to **K-oleate** and **NMe_4-oleate** (Figure 3.5, Table A2.4) which suggests that **11** also forms a partially interdigitated bilayer as discussed for the oleate salts in Chapter 2.

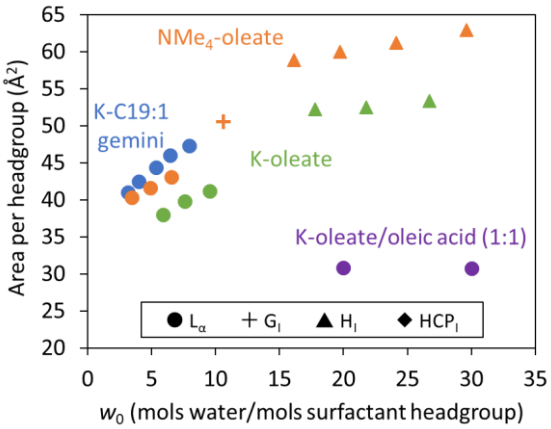

Figure 3.5: Area per headgroup of K-C19:1 gemini

Graph of area per headgroup of pure LLC phases K-C19:1 gemini (**11**) (blue), **NMe$_4$-oleate** (orange), **K-oleate** (green), and K-oleate/oleic acid (1:1) (data from Small and coworkers[99]) (blue) with increasing hydration, w_0.

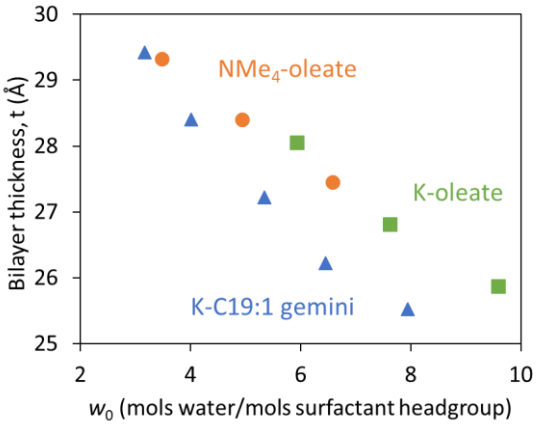

Figure 3.6: Bilayer thickness of K-C19:1 gemini

Bilayer thickness as a function of hydration for K-C19:1 gemini (**11**) (▲), **K-oleate** (■), and **NMe$_4$-oleate** (●).

3.5 Conclusions

We attempted to synthesize oleate-derived gemini surfactants via an olefin metathesis route and a route using a Wittig reaction. The metathesis route did not allow for *Z*-selectivity and was difficult to purify due to isomerization. The Wittig route is a more viable route to synthesizing oleate derived gemini surfactants allowing for *Z*-selectivity. Additionally, the modularity of the Wittig route could allow one to change the length of tail and placement of the unsaturation, as well as explore gemini dicarboxylates with different tail ends.

We used the Wittig route to synthesize a K-C19:1 gemini, **11**, and explored the phase behavior. Since **11** was not fully deprotonated, only flat curvature was observed and there was no region of NGC. While it was not intended for **11** to be partially deprotonated,

the extent of ionization could be used as a handle for fine tuning phase behavior by controlling the deprotonation stoichiometry as verified by titration. Higher extents of ionization should lead to more positive curvature, while lower extents of reaction will lead to flatter curvature or even negative mean curvature.[99] Furthermore, the phase behavior for a fully deprotonated K-C19:1 or K-C18:1 has not yet been mapped. It is hypothesized that the K-oleate gemini surfactant will lead to a wider network than that of the single-tail.

Mahanthappa and coworkers have shown that the phase behavior of gemini dicarboxylates is dependent on the linker length.[41, 47, 70] Furthermore, the phase behavior of **11** which has a 6-carbon linker suggests that even a "flexible" hydrocarbon linker can disallow headgroups from packing as close as they might prefer. Based on the surface area per headgroup of the **K-oleate** systems, the critical linker length for the oleate gemini system is probably closer to four carbons.

Chapter 4: Conclusion and Outlook

4.1 Conclusion

Periodic long-range ordered assemblies of amphiphilic molecules, known as lyotropic liquid crystals (LLCs), are governed by a subtle balance of noncovalent forces such as headgroup interactions and cohesive forces of hydrophobic tails. LLC phases with negative Gaussian curvature are of particular value in many applications such as membranes, drug delivery, and protein crystallization because of their 3-dimensional, interconnected hydrophobic and hydrophilic channels. In this thesis, we described our efforts to drive NGC formation by designing and synthesizing gemini amphiphile structures with oleate tails (18-carbon tails with one unsaturation).

In Chapter 2, we studied tetramethylammonium oleate/water and potassium oleate/water systems using small angle X-ray scattering (SAXS) to determine their LLC behavior as the control experiment for the gemini oleates. The **NMe_4-oleate** exhibited only narrow G_I-phase windows and **K-oleate** did not definitively exhibit an assignable network phase window, but we have tentatively indexed a tetragonal unit cell in these samples which we speculate to be a network phase. Instead of forming network phases, we hypothesized that the oleate salts relieve packing frustration between headgroup repulsions and hydrophobic cohesive forces by forming a partially interdigitated bilayer. The partially interdigitated bilayer allows for a tail packing density similar to nonane while maintaining the system's preferred inter-headgroup distance.

Chapter 3 details our efforts to synthesize and to study the phase behavior of oleate-derived gemini surfactants. Initial efforts to synthesize these molecules involved a metal-catalyzed olefin metathesis route. However, due to the low regioselectivity and the

formation of isomerization byproducts, the metathesis route was replaced with a route that instead utilizes a Wittig reaction. The Wittig route showed high *Z*-selectivity and is modular in design. We synthesized K-C19:1 gemini, **11**, using the Wittig route and explored the phase behavior. Since **11** was not fully deprotonated, only flat curvature was observed and there was no region of NGC. Unexpectedly, **11** had a higher area per headgroup than **K-oleate** at similar hydrations, suggesting that the long 6-carbon linker disallows preferred, tight intramolecular headgroup packings.

4.2 Outlook

More work is needed to definitively assign and create electron density reconstructions of the **K-oleate** phases between H_{II} and L_{α}. As discussed in Chapter 2 and Appendix 1, these phases may be rare network, mesh, or ribbon phases. While multiple studies, both old and new, have been directed towards assigning the **K-oleate** intermediate phases, there is still much to be learned.

The Wittig route described in Chapter 3 could be used to synthesize new gemini surfactants with mono-unsaturated tails, as well as a variety of other tail architectures. Some recommended tail structures are the oleate tail (9,10-*cis*-unsaturation), as well as variations that change the placement of the unsaturation. The oleate-derived gemini surfactants are expected to have a wider network phase window than their single-tail oleate salt counterparts. Linker length is an important parameter for LLC phase behavior, based on the observed area per headgroup of the oleate salts and the gemini, **11**, it is recommended that a linker length of 3- or 4- carbons be tried. Another suggested tail structure is to add 5-, 6-, and 7- carbon cyclic tail ends that mimic structures found in

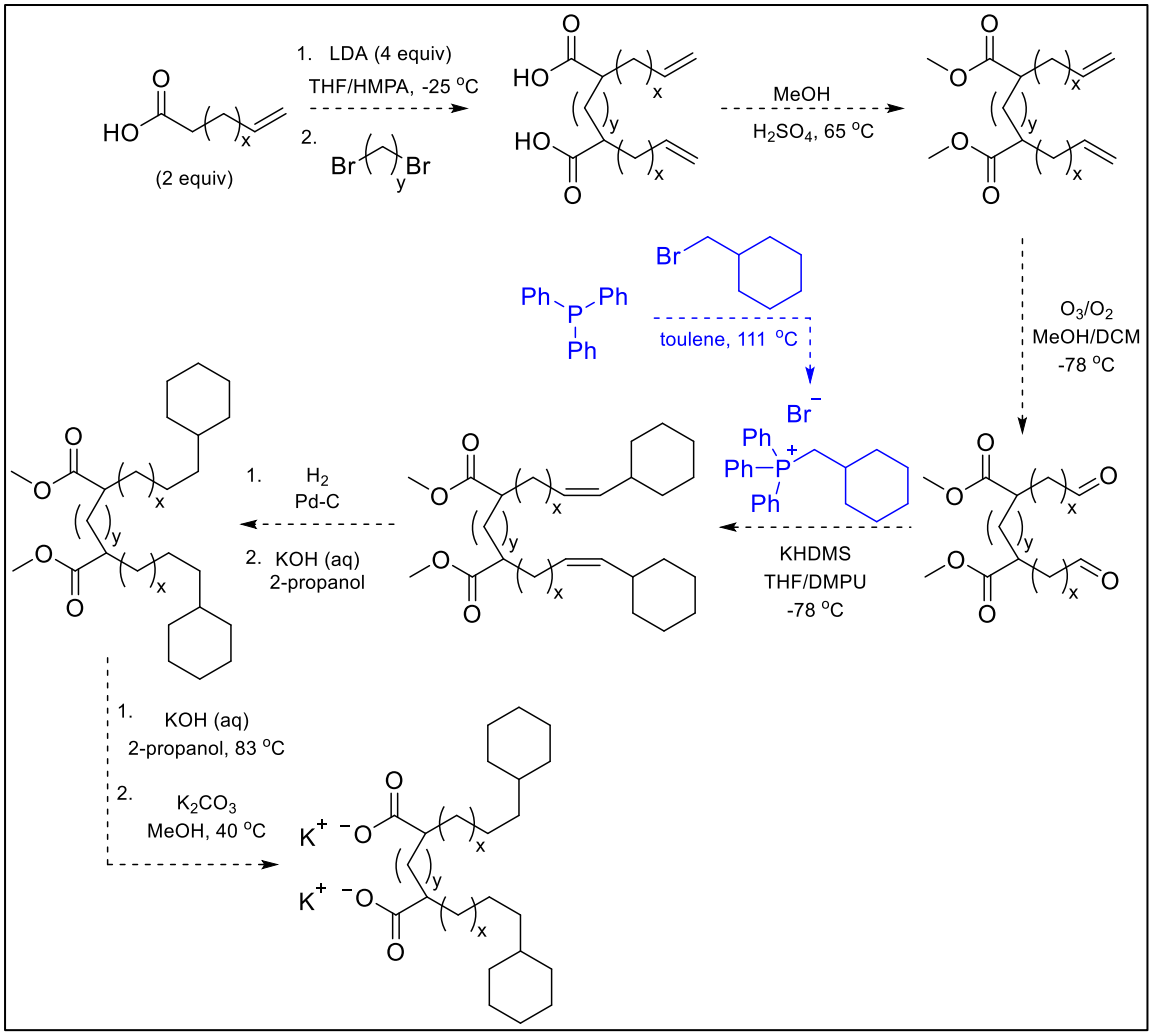

Scheme 4.1: Proposed synthesis of gemini surfactant with cyclic tail end using Wittig reaction

thermoacidophilic archaebacteria. Cyclic tail ends have been shown to act as fluidizers in membranes below their gel transition temperature and as immobilizers in membranes above their gel transition temperature.[110-113] These cyclic tail ends would be expected to disrupt hydrocarbon tail packing and may open unusual LLC phases. A suggested route to forming gemini surfactants with cyclic tail ends using a Wittig reaction is shown in Scheme 4.1.

The results from Chapter 2 warrant further investigation into L_α tail packing. In Chapter 2, a partially interdigitated bilayer model was proposed for the L_α packing of **K-oleate** and **NMe$_4$-oleate**, and subsequently the K-C19:1 gemini, **11**, in Chapter 3. However, further small angle neutron scattering (SANS) experiments are needed to verify the model. If a partially interdigitated bilayer is being formed, one could create neutron scattering contrast in the region where the tail segments overlap by synthesizing oleate salts in which the tail segment after the unsaturation is deuterated. This would allow one to measure the length of this segment and compare it to the expected value based on the constant density argument made in Chapter 2 and Appendix 1. Furthermore, this could be done for a series of salts with varied tail lengths and positions of the unsaturation which would have slightly different values for the expected overlap length. These molecules could be synthesized by adopting the Wittig chemistry worked out in Chapter 3; a suggested route is shown in Scheme 4.2.

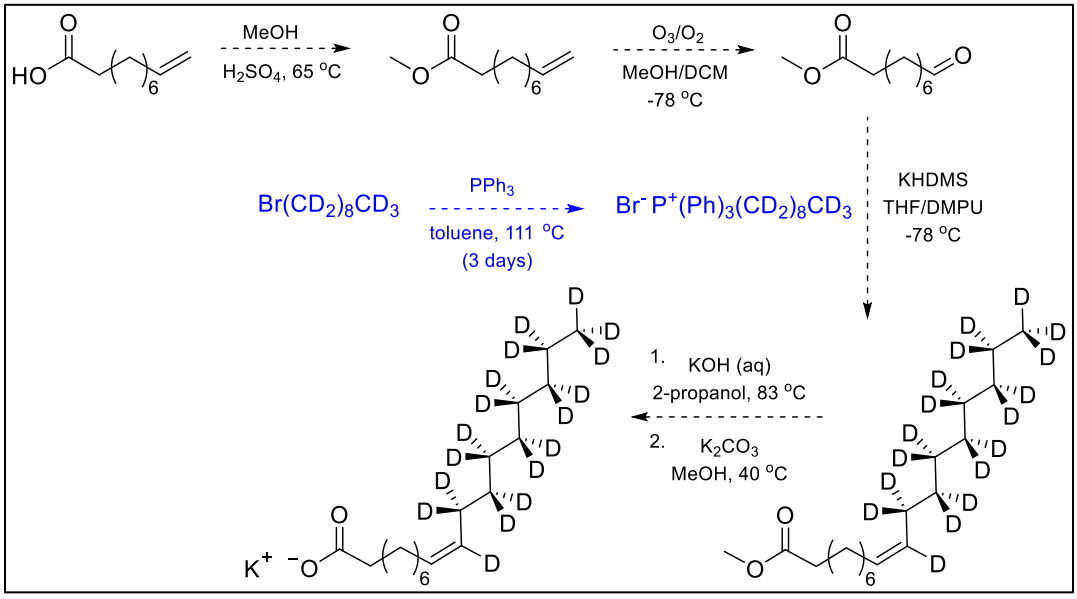

Scheme 4.2: Proposed synthesis of potassium oleate with deuterated tail ends using a Wittig reaction

References

1. Chapman, D., *Biological Membranes; Physical Fact and Function*. Academic Press: London, 1968.

2. Escribá, P. V.; González-Ros, J. M.; Goñi, F. M.; Kinnunen, P. K.; Vigh, L.; Sánchez-Magraner, L.; Fernández, A. M.; Busquets, X.; Horváth, I.; Barceló-Coblijn, G., Membranes: a meeting point for lipids, proteins and therapies. *J. Cell. Mol. Med.* **2008,** *12* (3), 829-875.

3. Zimmerberg, J.; Kozlov, M. M., How proteins produce cellular membrane curvature. *Nat. Rev. Mol. Cell Biol.* **2006,** *7* (1), 9-19.

4. Shearman, G.; Ces, O.; Templer, R.; Seddon, J., Inverse lyotropic phases of lipids and membrane curvature. *J. Phys.: Condens. Matter* **2006,** *18* (28), S1105-S1124.

5. Hyde, S. T., Identification of lyotropic liquid crystalline mesophases. In *Handbook of Applied Surface and Colloid Chemistry*, Holmberg, K., Ed. 2001; Vol. 2, pp 299-332.

6. Mackay, A. L., Periodic minimal surfaces. *Physica B+C* **1985,** *131* (1-3), 300-305.

7. Guo, C.; Wang, J.; Cao, F.; Lee, R. J.; Zhai, G., Lyotropic liquid crystal systems in drug delivery. *Drug Discovery Today* **2010,** *15* (23-24), 1032-1040.

8. Cherezov, V.; Clogston, J.; Misquitta, Y.; Abdel-Gawad, W.; Caffrey, M., Membrane protein crystallization in meso: lipid type-tailoring of the cubic phase. *Biophys. J.* **2002,** *83* (6), 3393-3407.

9. Kulkarni, C. V., Lipid crystallization: from self-assembly to hierarchical and biological ordering. *Nanoscale* **2012,** *4* (19), 5779-5791.

10. Byrne, P.; Chapman, D., Liquid crystalline nature of phospholipids. *Nature* **1964,** *202* (4936), 987-988.

11. Chapman, D.; Collin, D., Differential thermal analysis of phospholipids. *Nature* **1965,** *206* (4980), 189.

12. Demetzos, C., Differential scanning calorimetry (DSC): a tool to study the thermal behavior of lipid bilayers and liposomal stability. *J. Liposome Res.* **2008,** *18* (3), 159-173.

13. Cullis, P.; De Kruijff, B., The polymorphic phase behaviour of phosphatidylethanolamines of natural and synthetic origin. A 31P NMR study. *Biochim. Biophys. Acta* **1978,** *513* (1), 31-42.

14. Frederik, P. M.; Burger, K. N.; Stuart, M. C.; Verkleij, A. J., Lipid polymorphism as observed by cryo-electron microscopy. *Biochim. Biophys. Acta* **1991,** *1062* (2), 133-141.

15. Chapman, D.; Byrne, P.; Shipley, G., The physical properties of phospholipids I. Solid state and mesomorphic properties of some 2, 3-diacyl-DL-phosphatidylethanolamines. *Proc. R. Soc. London, Ser. A* **1966,** *290* (1420), 115-142.

16. Kaoui, B.; Biros, G.; Misbah, C., Why do red blood cells have asymmetric shapes even in a symmetric flow? *Phys. Rev. Lett.* **2009,** *103* (18), 188101.

17. Dommersnes, P. G.; Fournier, J.-B., The many-body problem for anisotropic membrane inclusions and the self-assembly of "saddle" defects into an "egg carton". *Biophys. J.* **2002,** *83* (6), 2898-2905.

18. Boyd, K. J.; Alder, N. N.; May, E. R., Buckling under pressure: Curvature-based lipid segregation and stability modulation in cardiolipin-containing bilayers. *Langmuir* **2017,** *33* (27), 6937-6946.

19. Unsay, J. D.; Cosentino, K.; Subburaj, Y.; García-Sáez, A. J., Cardiolipin effects on membrane structure and dynamics. *Langmuir* **2013,** *29* (51), 15878-15887.

20. Fournier, J. B., Nontopological saddle-splay and curvature instabilities from anisotropic membrane inclusions. *Phys. Rev. Lett.* **1996,** *76* (23), 4436-4439.

21. Budnik, A.; Stephens, D. J., ER exit sites – Localization and control of COPII vesicle formation. *FEBS Lett.* **2009,** *583* (23), 3796-3803.

22. Schmidt, N. W.; Mishra, A.; Wang, J.; DeGrado, W. F.; Wong, G. C., Influenza virus A M2 protein generates negative Gaussian membrane curvature necessary for budding and scission. *J. Am. Chem. Soc.* **2013,** *135* (37), 13710-13719.

23. Braun, A. R.; Sevcsik, E.; Chin, P.; Rhoades, E.; Tristram-Nagle, S.; Sachs, J. N., α-Synuclein induces both positive mean curvature and negative Gaussian curvature in membranes. *J. Am. Chem. Soc.* **2012,** *134* (5), 2613-2620.

24. Mouritsen, O. G., Lipids, curvature, and nano-medicine. *Eur. J. Lipid Sci. Technol.* **2011,** *113* (10), 1174-1187.

25. Varkouhi, A. K.; Scholte, M.; Storm, G.; Haisma, H. J., Endosomal escape pathways for delivery of biologicals. *J. Controlled Release* **2011,** *151* (3), 220-228.

26. de Gennes, P. G., *The Physics of Liquid Crystals*. 2 ed.; Clarendon Press: Oxford, 1974; p 1-10.

27. Chandler, D., Interfaces and the driving force of hydrophobic assembly. *Nature* **2005,** *437* (7059), 640-647.

28. Israelachvili, J. N.; Mitchell, D. J.; Ninham, B. W., Theory of self-assembly of lipid bilayers and vesicles. *Biochim. Biophys. Acta* **1977,** *470* (2), 185-201.

29. Fong, C.; Le, T.; Drummond, C. J., Lyotropic liquid crystal engineering–ordered nanostructured small molecule amphiphile self-assembly materials by design. *Chem. Soc. Rev.* **2012,** *41* (3), 1297-1322.

30. Sorenson, G. P., Triply periodic multiply continuous lyotropic liquid crystals derived from gemini surfactants. Ph. D. Dissertation, UW Madison, 2013.

31. Hatakeyama, E. S.; Gabriel, C. J.; Wiesenauer, B. R.; Lohr, J. L.; Zhou, M.; Noble, R. D.; Gin, D. L., Water filtration performance of a lyotropic liquid crystal polymer membrane with uniform, sub-1-nm pores. *J. Membr. Sci.* **2011,** *366* (1-2), 62-72.

32. Zabara, A.; Amar-Yuli, I.; Mezzenga, R., Tuning in-meso-crystallized lysozyme polymorphism by lyotropic liquid crystal symmetry. *Langmuir* **2011,** *27* (10), 6418-6425.

33. Wan, Y.; Zhao, D., On the controllable soft-templating approach to mesoporous silicates. *Chem. Rev.* **2007,** *107* (7), 2821-2860.

34. Leal, C. l.; Bouxsein, N. F.; Ewert, K. K.; Safinya, C. R., Highly efficient gene silencing activity of siRNA embedded in a nanostructured gyroid cubic lipid matrix. *J. Am. Chem. Soc.* **2010,** *132*, 16841-16847.

35. Martiel, I.; Sagalowicz, L.; Mezzenga, R., Phospholipid-based nonlamellar mesophases for delivery systems: bridging the gap between empirical and rational design. *Adv. Colloid Interface Sci.* **2014,** *209*, 127-143.

36. Sivakumar, S.; Wark, K. L.; Gupta, J. K.; Abbott, N. L.; Caruso, F., Liquid crystal emulsions as the basis of biological sensors for the optical detection of bacteria and viruses. *Adv. Funct. Mater.* **2009,** *19* (14), 2260-2265.

37. Meikle, T.; Drummond, C.; Separovic, F.; Conn, C., Membrane-mimetic inverse bicontinuous cubic phase systems for encapsulation of peptides and proteins. In

Advances in Biomembranes and Lipid Self-Assembly, Elsevier: 2017; Vol. 25, pp 63-94.

38. Kulkarni, C. V.; Ces, O.; Templer, R. H.; Seddon, J. M., Pressure effects on a protein–lipid model membrane. *Soft Matter* **2013,** *9* (28), 6525-6531.

39. Schröder-Turk, G. E.; De Campo, L.; Evans, M. E.; Saba, M.; Kapfer, S. C.; Varslot, T.; Grosse-Brauckmann, K.; Ramsden, S.; Hyde, S. T., Polycontinuous geometries for inverse lipid phases with more than two aqueous network domains. *Faraday Discuss.* **2013,** *161*, 215-247.

40. Hyde, S. T.; Schröder, G. E., Novel surfactant mesostructural topologies: between lamellae and columnar (hexagonal) forms. *Curr. Opin. Colloid Interface Sci.* **2003,** *8*, 5-14.

41. Perroni, D. V.; Baez-Cotto, C. M.; Sorenson, G. P.; Mahanthappa, M. K., Linker length-dependent control of gemini surfactant aqueous lyotropic gyroid phase stability. *J. Phys. Chem. Lett.* **2015,** *6* (6), 993-998.

42. Sorenson, G. P.; Schmitt, A. K.; Mahanthappa, M. K., Discovery of a tetracontinuous, aqueous lyotropic network phase with unusual 3D-hexagonal symmetry. *Soft Matter* **2014,** *10* (41), 8229-8235.

43. Phan, S.; Fong, W.-K.; Kirby, N.; Hanley, T.; Boyd, B. J., Evaluating the link between self-assembled mesophase structure and drug release. *Int. J. Pharm.* **2011,** *421* (1), 176-182.

44. Conn, C. E.; Darmanin, C.; Sagnella, S. M.; Mulet, X.; Greaves, T. L.; Varghese, J. N.; Drummond, C. J., Incorporation of the dopamine D2L receptor and bacteriorhodopsin within bicontinuous cubic lipid phases. 1. Relevance to in meso crystallization of integral membrane proteins in monoolein systems. *Soft Matter* **2010,** *6* (19), 4828-4837.

45. Rummel, G.; Hardmeyer, A.; Widmer, C.; Chiu, M. L.; Nollert, P.; Locher, K. P.; Pedruzzi, I.; Landau, E. M.; Rosenbusch, J. P., Lipidic cubic phases: new matrices for the three-dimensional crystallization of membrane proteins. *J. Struct. Biol.* **1998,** *121* (2), 82-91.

46. Landau, E. M.; Rosenbusch, J. P., Lipidic cubic phases: a novel concept for the crystallization of membrane proteins. *Proc. Natl. Acad. Sci. USA* **1996,** *93* (25), 14532-14535.

47. Sorenson, G. P.; Coppage, K. L.; Mahanthappa, M. K., Unusually stable aqueous lyotropic gyroid phases from gemini dicarboxylate surfactants. *J. Am. Chem. Soc.* **2011,** *133* (38), 14928-14931.

48. Dierking, I., *Textures of Liquid Crystals*. John Wiley & Sons: 2003.

49. Schulz, P.; Puig, J.; Barreiro, G.; Torres, L., Thermal transitions in surfactant-based lyotropic liquid crystals. *Thermochim. Acta* **1994,** *231*, 239-256.

50. Mezzenga, R.; Meyer, C.; Servais, C.; Romoscanu, A. I.; Sagalowicz, L.; Hayward, R. C., Shear rheology of lyotropic liquid crystals: A case study. *Langmuir* **2005,** *21*, 3322-3333.

51. Winey, K. I.; Patel, S. S.; Larson, R. G.; Watanabe, H., Morphology of a lamellar diblock copolymer aligned perpendicular to the sample plane: Transmission electron microscopy and small-angle X-ray scattering. *Macromolecules* **1993,** *26* (16), 4373-4375.

52. Gu, X.; Liu, Z.; Gunkel, I.; Chourou, S.; Hong, S. W.; Olynick, D. L.; Russell, T. P., High aspect ratio sub-15 nm silicon trenches from block copolymer templates. *Adv. Mater.* **2012,** *24* (42), 5688-5694.

53. Israelachvili, J. N.; Mitchell, D. J.; Ninham, B. W., Theory of self-assembly of hydrocarbon amphiphiles into micelles and bilayers. *J. Chem. Soc., Faraday Trans. 2* **1976,** *72*, 1525-1568.

54. Kulkarni, C. V.; Tang, T.-Y.; Seddon, A. M.; Seddon, J. M.; Ces, O.; Templer, R. H., Engineering bicontinuous cubic structures at the nanoscale—the role of chain splay. *Soft Matter* **2010,** *6* (14), 3191-3914.

55. Qiu, H.; Caffrey, M., The phase diagram of the monoolein/water system: metastability and equilibrium aspects. *Biomaterials* **2000,** *21* (3), 223-234.

56. Nagarajan, R., Molecular packing parameter and surfactant self-assembly: The neglected role of the surfactant tail. *Langmuir* **2002,** *18* (1), 31-38.

57. Abbott, S. J., *Surfactant Science: Principles & Practice*. DEStech Publications, Incorporated: 2017.

58. Kulkarni, C. V.; Wachter, W.; Iglesias-Salto, G.; Engelskirchen, S.; Ahualli, S., Monoolein: a magic lipid? *Phys. Chem. Chem. Phys.* **2011,** *13* (8), 3004-3021.

59. Qiu, H.; Caffrey, M., Lyotropic and thermotropic phase behavior of hydrated monoacylglycerols: structure characterization of monovaccenin. *J. Phys. Chem. B* **1998,** *102* (24), 4819-4829.

60. Barauskas, J.; Landh, T., Phase behavior of the phytantriol/water system. *Langmuir* **2003,** *19* (23), 9562-9565.

61. Yamashita, J.; Shiono, M.; Hato, M., New lipid family that forms inverted cubic phases in equilibrium with excess water: Molecular structure− aqueous phase structure relationship for lipids with 5, 9, 13, 17-tetramethyloctadecyl and 5, 9, 13, 17-tetramethyloctadecanoyl chains. *J. Phys. Chem. B* **2008,** *112* (39), 12286-12296.

62. Brooks, N. J.; Hamid, H. A.; Hashim, R.; Heidelberg, T.; Seddon, J. M.; Conn, C. E.; Mirzadeh Husseini, S. M.; Zahid, N. I.; Hussen, R. S. D., Thermotropic and lyotropic liquid crystalline phases of Guerbet branched-chain-D-glucosides. *Liq. Cryst.* **2011,** *38* (11-12), 1725-1734.

63. Hato, M.; Yamashita, J.; Shiono, M., Aqueous phase behavior of lipids with isoprenoid type hydrophobic chains. *J. Phys. Chem. B* **2009,** *113* (30), 10196-10209.

64. Salkar, R. A.; Minamikawa, H.; Hato, M., Alkylglucosides with isoprenoid-type hydrophobic chains-effects of hydrophobic chain size on the aqueous phase behavior. *Chem. Phys. Lipids* **2004,** *127* (1), 65-75.

65. Hatakeyama, E. S.; Wiesenauer, B. R.; Gabriel, C. J.; Noble, R. D.; Gin, D. L., Nanoporous, bicontinuous cubic lyotropic liquid crystal networks via polymerizable gemini ammonium surfactants. *Chem. Mater.* **2010,** *22* (16), 4525-4527.

66. Pindzola, B. A.; Jin, J.; Gin, D. L., Cross-linked normal hexagonal and bicontinuous cubic assemblies via polymerizable gemini amphiphiles. *J. Am. Chem. Soc.* **2003,** *125* (10), 2940-2949.

67. Robertson, L. A.; Schenkel, M. R.; Wiesenauer, B. R.; Gin, D. L., Alkyl-bis (imidazolium) salts: A new amphiphile platform that forms thermotropic and non-aqueous lyotropic bicontinuous cubic phases. *Chem. Commun.* **2013,** *49* (82), 9407-9409.

68. Mondal, J.; Mahanthappa, M.; Yethiraj, A., Self-assembly of gemini surfactants: A computer simulation study. *J. Phys. Chem. B* **2012,** *117* (16), 4254-4262.

69. Zana, R., Dimeric (gemini) surfactants: effect of the spacer group on the association behavior in aqueous solution. *J. Colloid Interface Sci.* **2002,** *248* (2), 203-220.

70. Mantha, S.; McDaniel, J. G.; Perroni, D. V.; Mahanthappa, M. K.; Yethiraj, A., Electrostatic Interactions Govern “Odd/Even” Effects in Water-Induced Gemini Surfactant Self-Assembly. *J. Phys. Chem. B* **2017,** *121* (3), 565-576.

71. Fong, C.; Wells, D.; Krodkiewska, I.; Hartley, P. G.; Drummond, C. J., New role for urea as a surfactant headgroup promoting self-assembly in water. *Chem. Mater.* **2006,** *18* (3), 594-597.

72. Faul, C. F.; Antonietti, M., Ionic self-assembly: Facile synthesis of supramolecular materials. *Adv. Mater.* **2003,** *15* (9), 673-683.

73. Luzzati, V.; Husson, F., The structure of the liquid-crystalline phases of lipid-water systems. *J. Cell Biol.* **1962,** *12* (2), 207-219.

74. Luzzati, V.; Mustacchi, H.; Skoulios, A., The structure of the liquid-crystal phases of some soap+ water systems. *Discuss. Faraday Soc.* **1958,** *25*, 43-50.

75. Luzzati, V.; Tardieu, A.; Gulik-Krzywicki, T.; Rivas, E.; Reiss-Husson, F., Structure of the cubic phases of lipid–water systems. *Nature* **1968,** *220* (5166), 485-488.

76. Klein, R.; Tiddy, G. J.; Maurer, E.; Touraud, D.; Esquena, J.; Tache, O.; Kunz, W., Aqueous phase behaviour of choline carboxylate surfactants—Exceptional variety and extent of cubic phases. *Soft Matter* **2011,** *7* (15), 6973-6983.

77. Molchanov, V.; Philippova, O., Effects of concentration and temperature on viscoelastic properties of aqueous potassium oleate solutions. *Colloid J.* **2009,** *71* (2), 239-245.

78. Molchanov, V.; Shashkina, Y. A.; Philippova, O.; Khokhlov, A., Viscoelastic properties of aqueous anionic surfactant (potassium oleate) solutions. *Colloid J.* **2005,** *67* (5), 606-609.

79. Klevens, H., Structure and aggregation in dilate solution of surface active agents. *J. Am. Oil Chem. Soc.* **1953,** *30* (2), 74-80.

80. Sata, N.; Tyûzyô, K., On the relation between viscosity and critical micelle concentration of detergent solutions. *Bull. Chem. Soc. Jpn.* **1953,** *26* (4), 177-183.

81. Friberg, S.; Burasczenska, I., Microemulsions in the Water-Potassium Oleate-Benzene System. In *Emulsions*, Springer: 1978; pp 1-9.

82. Sjöblom, E.; Friberg, S., Light-scattering and electron microscopy determinations of association structures in W/O microemulsions. *J. Colloid Interface Sci.* **1978,** *67* (1), 16-30.

83. Gerbacia, W.; Rosano, H.; Zajac, M., Solubilization in aqueous mixed micellar solutions: Water-potassium oleate-1-pentanol-benzene. *J. Am. Oil Chem. Soc.* **1976,** *53* (3), 101-104.

84. Nora, A.; Szczepanek, A.; Koenen, G., Metallic Soaps. In *Ullmann's Encyclopedia of lndustrial Chemistry*, Wiley-VCH: Weinheim, 2001.

85. Food and Drug Administration, Food Additive Status List. https://www.fda.gov/food/food-additives-petitions/food-additive-status-list.

86. Vold, R. D., The phase rule behavior of concentrated aqueous systems of a typical colloidal electrolyte: Sodium oleate. *J. Phys. Chem.* **1939,** *43*, 1213-1231.

87. Eins, S., Electron microscopy of mesomorphic structures of aqueous lipid phases. I. The system potassium oleate/water. *Mol. Cryst. Liq. Cryst.* **1970,** *11* (2), 119-132.

88. Borné, J.; Nylander, T.; Khan, A., Vesicle formation and other structures in aqueous dispersions of monoolein and sodium oleate. *J. Colloid Interface Sci.* **2003,** *257*, 310-320.

89. Antunes, F. E.; Coppola, L.; Gaudio, D.; Nicotera, I.; Oliviero, C., Shear rheology and phase beaviour of sodium oleate/water mixtures. *Colloids Surf., A* **2007,** *297*, 95-104.

90. McBain, J. W.; Sierichs, W. C., The solubility of sodium and potassium soaps and the phase diagrams of aqueous potassium soaps. *J. Am. Oil Chem. Soc.* **1948,** *25* (6), 221-225.

91. Jackson, G. L.; Poulsen, K. M.; Bible, N. G.; Jennings, J.; Mahanthappa, M. K., Polycontinuous network phase formation in single-tail surfactants induced by anisotropic gemini surfactant inclusions. *Manuscript in preparation*.

92. Zeng, X.; Liu, Y.; Impéror-Clerc, M., Hexagonal close packing of nonionic surfactant micelles in water. *J. Phys. Chem. B* **2007,** *111* (19), 5174-5179.

93. Liu, C. K.; Warr, G. G., Hexagonal closest-packed spheres liquid crystalline phases stabilised by strongly hydrated counterions. *Soft Matter* **2014,** *10* (1), 83-87.

94. Jayaraman, A.; Mahanthappa, M. K., Counterion-dependent access to low-symmetry lyotropic sphere packings of ionic surfactant micelles. *Langmuir* **2018,** *34* (6), 2290-2301.

95. Kekicheff, P.; Cabane, B., Between cylinders and bilayers: Structures of intermediate mesophases of the SDS/water system. *J. Phys. (Paris)* **1987,** *48* (9), 1571-1583.

96. Luzzati, P.; Mustacchi, H.; Husson, F.; Skouliosn, A., The structures of colloid association 1. The liquid crystalline phases of amphiphile-water systems. *Acta Crystallog. A* **1960,** *13*, 660-667.

97. Hagslätt, H.; Söderman, O.; Jönsson, B., The structure of intermediate ribbon phases in surfactant systems. *Liq. Cryst.* **1992,** *12* (4), 667-688.

98. Luzzati, V., X-ray diffraction studies of lipid-water systems. *Biol. Membr.* **1968,** *1*, 71-123.

99. Cistola, D. P.; Atkinson, D.; Hamilton, J. A.; Small, D. M., Phase behavior and bilayer properties of fatty acids: hydrated 1: 1 acid-soaps. *Biochemistry* **1986,** *25* (10), 2804-2812.

100. Briggs, J.; Chung, H.; Caffrey, M., The temperature-composition phase diagram and mesophase structure characterization of the monoolein/water system. *J. Phys. II* **1996,** *6* (5), 723-751.

101. Chen, Y.-f., Phase behavior of cardiolipin. Cornell University, 2012.

102. Zana, R.; Xia, J., *Gemini Surfactants: Synthesis, Interfacial and Solution-Phase Behavior, and Applications*. CRC Press: 2003; Vol. 117.

103. Zana, R., Gemini (dimeric) surfactants. *Curr. Opin. Colloid Interface Sci.* **1996,** *1* (5), 566-571.

104. Quinn, P.; Joo, F.; Vigh, L., The role of unsaturated lipids in membrane structure and stability. *Prog. Biophys. Mol. Biol.* **1989,** *53* (2), 71-103.

105. Hong, S. H.; Sanders, D. P.; Lee, C. W.; Grubbs, R. H., Prevention of undesirable isomerization during olefin metathesis. *J. Am. Chem. Soc.* **2005,** *127* (49), 17160-17161.

106. Keitz, B. K.; Endo, K.; Patel, P. R.; Herbert, M. B.; Grubbs, R. H., Improved ruthenium catalysts for Z-selective olefin metathesis. *J. Am. Chem. Soc.* **2011,** *134* (1), 693-699.

107. Cho, J. H.; Kim, B. M., An efficient method for removal of ruthenium byproducts from olefin metathesis reactions. *Org. Lett.* **2003,** *5* (4), 531-533.

108. Mostyn, S. N.; Carland, J. E.; Shimmon, S.; Ryan, R. M.; Rawling, T.; Vandenberg, R. J., Synthesis and characterization of novel acyl-glycine inhibitors of GlyT2. *ACS Chem. Neurosci.* **2017,** *8* (9), 1949-1959.

109. Bestmann, H. J.; Stransky, W.; Vostrowsky, O., Reaktionen mit Phosphinalkylenen, XXXIII. Darstellung lithiumsalzfreier Ylidlösungen mit Natrium-bis (trimethylsilyl) amid als Base. *Chem. Ber.* **1976,** *109* (5), 1694-1700.

110. Kannenberg, E.; Blume, A.; Poralla, K., Properties of ω-cyclohexane fatty acids in membranes. *FEBS Lett.* **1984,** *172* (2), 331-334.

111. Endo, T.; Inoue, K.; Nojima, S.; Terashima, S.; Oshima, T., Synthesis and physical properties of phosphatidylcholines containing ω-cyclohexyl fatty acyl chains. *Chem. Phys. Lipids* **1982,** *31* (1), 61-74.

112. Sunamoto, J.; Iwamoto, K.; Inoue, K.; Endo, T.; Nojima, S., Liposomal membranes XI. A suggestion to structural characteristics of acido-thermophilic bacterial membranes. *Biochim. Biophys. Acta* **1982,** *685* (3), 283-288.

113. Hamilton, R. J., *Lipid Analysis in Oils and Fats*. Springer science & business media: 2012.

114. Cistola, D. P.; Hamilton, J. A.; Jackson, D.; Small, D. M., Ionization and phase behavior of fatty acids in water: application of the Gibbs phase rule. *Biochemistry* **1988,** *27* (6), 1881-1888.

Appendix 1: Supporting Information for Chapter 2 - LLC Phase Behavior of Oleate Salts

A1.1 Detailed Synthesis for Oleate Salts

Table A1.1: Lab notebook page numbers for synthesis oleate salts

Molecule	Notebook Page
NMe_4-oleate	MTH-I-060
K-oleate	MTH-I-067

Materials: All materials and reagent grade solvents were purchased from Sigma Aldrich (Milwaukee, WI) and used as received unless otherwise noted. Oleic acid was purchased from MilliporeSigma and was stored at 0 °C and away from light. Tetramethylammonium hydroxide solution (NMe_4OH) (~1.0 M) was titrated with 1.0 N HCl to determine the exact molarity. Milli-Q water (18 MΩ) was obtained from ThermoScietific Barnstead NANOpure^{TM} and was sparged with $N_2(g)$ for a minimum of 30 minutes before use.

Molecular Characterization: ^1H nuclear magnetic resonance (NMR) data was collected on a Bruker Advance 400 MHz. The samples were referenced to the residual proton shift in CD_3OD (3.31 ppm), DMSO-d_6 (2.50 ppm), or $CDCl_3$ (7.26 ppm). Elemental analysis (C, H, N) was performed by Atlantic Microlab, Inc. (Norcross, GA, USA).

Synthesis of oleate salts: Oleate salts (**K-oleate** or **NMe_4-oleate**) were synthesized as shown in Scheme 2.1.[1] Oleic acid was dissolved in MeOH (~0.1 M) and stirred until it forms a homogeneous solution. To this, $K_2CO_3(s)$ or 1 M $NMe_4OH(aq)$ was added in stoichiometric molar equivalents to deprotonate oleic acid. The reaction vessel was stirred with a vent needle for ~6 hours. After the reaction reached completion, all volatiles were removed using vacuum and the resulting sample was azeotropically freeze-dried from

benzene multiple times to remove residual water and stored in the glovebox. **K-oleate** ^{1}H NMR: (400 MHz, CD_3OD) δ (ppm): 5.34 (m, 2H), 2.15 (t, 2H), 2.03 (m, 4H), 1.60 (tt, 2H), 1.33 (m, 20H), 0.90 (t, 3H). Elemental Analysis: C (67.63 %), H (10.45%). **NMe_4-oleate** ^{1}H NMR: (400 MHz, CD_3OD) δ (ppm): 5.35 (m, 2H), 3.20 (s, 12H), 2.16 (t, 2H), 2.04 (m, 4H), 1.60 (tt, 2H), 1.33 (m, 20H), 0.91 (t, 3H). Elemental Analysis: C (69.62 %), H (12.80%), N (3.70)

A1.2 Possible Intermediate Phases of K-oleate

A1.2.1 55 wt% - Tetragonal or Complex Hexagonal (2D)

Luzzati and coworkers identified the complex hexagonal phase as a possible intermediate phase between H_I and L_α. The complex hexagonal phase is described as cylindrical bilayer arranged on a hexagonally packed lattice (Figure A1.1 b). At 55 wt% after annealing for 1.5 hours at 60 °C, a pattern was obtained at 25 °C that can be indexed with a 2D hexagonal unit cell (Figure A1.2 red trace). Compared with normal H_I for **K-oleate**, this pattern has broader peaks and the (100) appears at much lower *q*.

For the same sample at 70 °C, a pattern was obtained that can be indexed with a simple tetragonal unit cell (Figure A1.3 green trace). Tetragonal phases have been observed by Kekicheff and Cabane in sodium dodecyl sulfate (SDS) and water systems between H_I and L_α.[2]

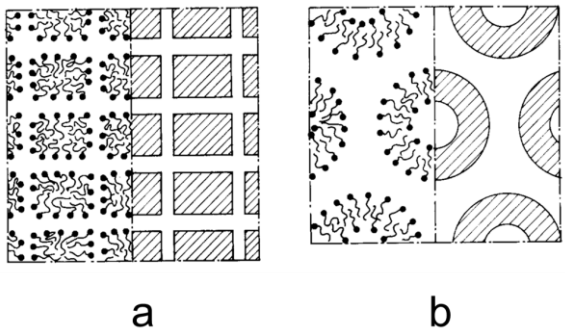

Figure A1.1: Diagram of rectangular (ribbon) and complex hexagonal phases

Luzzati's purposed intermediate phases: (a) rectangular (ribbon) and (b) complex hexagonal phases.[3] Fig. from Ref [3].

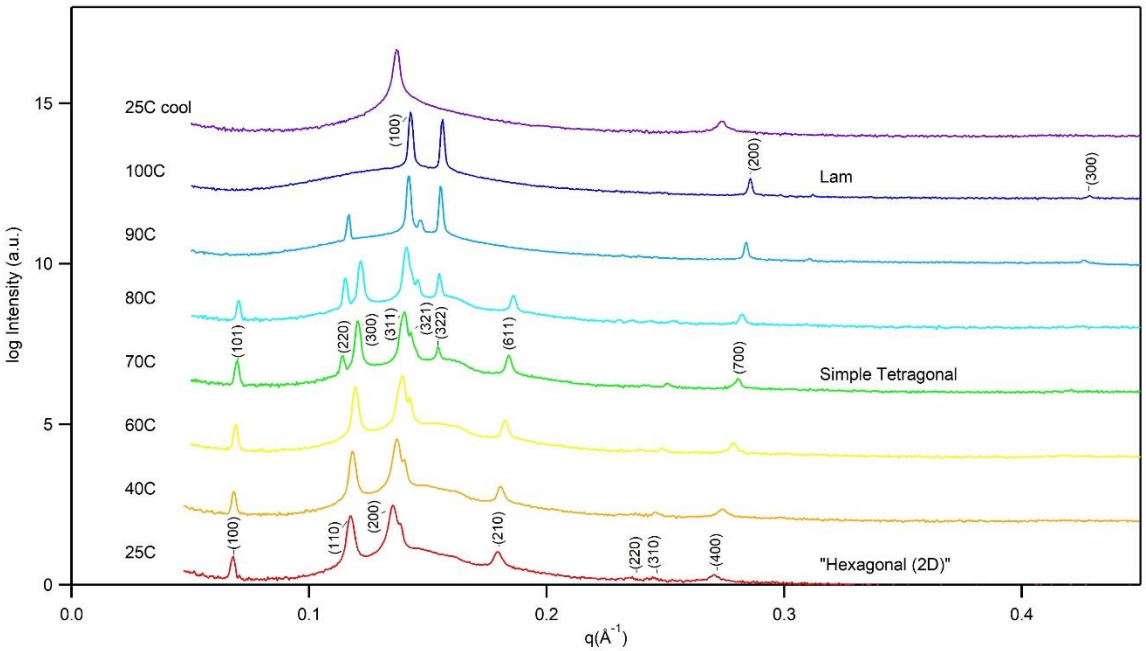

Figure A1.2: 1D SAXS patterns of **K-oleate** at 55 wt% after annealing for 1.5 hours at 60 °C.

A1.2.2 60 wt% - 3D Hexagonal

The SAXS pattern collected for **K-oleate** at 60 wt% and 27 °C can be indexed with a hexagonal (3D) lattice (Figure A1.3 red trace). Le Bail refinement and X-ray background fitting using *JANA2006* crystallographic computing software package[4] of the one-dimensional SAXS intensity $I(q)$ *versus* scattering wavevector, q, enabled extraction of the

static structure factor intensities. Miller indices using *P6* space group symmetry with 3D-hexagonal unit cell parameters of a = 107.79 Å and c = 43.2 Å were assigned. Application of the SUPERFLIP charge-flipping algorithm[5] by allowing it to determine the space group yielded one converged election density map with poor figures of merit, fm = 56. SUPERFLIP determined the space group to be *P6/mmm* and the electron density reconstruction of the 90% isosurface rendered by VESTA software package[6] shows elongated micelles (as if pinched off from an undulating column) arranged on a hexagonal lattice surrounded by a lamellar mesh (Figure A1.4). However, this electron density reconstruction could not be replicated for this SAXS pattern. Chen, et al. report a similar electron density reconstruction with *P6/mmm* symmetry, but instead of micelles, they claim undulating columns.[7] This pattern is similar to the 55 wt% at 25 °C after annealing, except that there is an additional dimension exhibited by the (001) and (002) peak. This could be a 3D-hexagonal unit cell (a = 108.3 Å, c = 94.0 Å) with L_α coexistence (d = 43.2 Å). This seems more likely since the peaks labeled (001) and (002) are less broad than the other peaks.

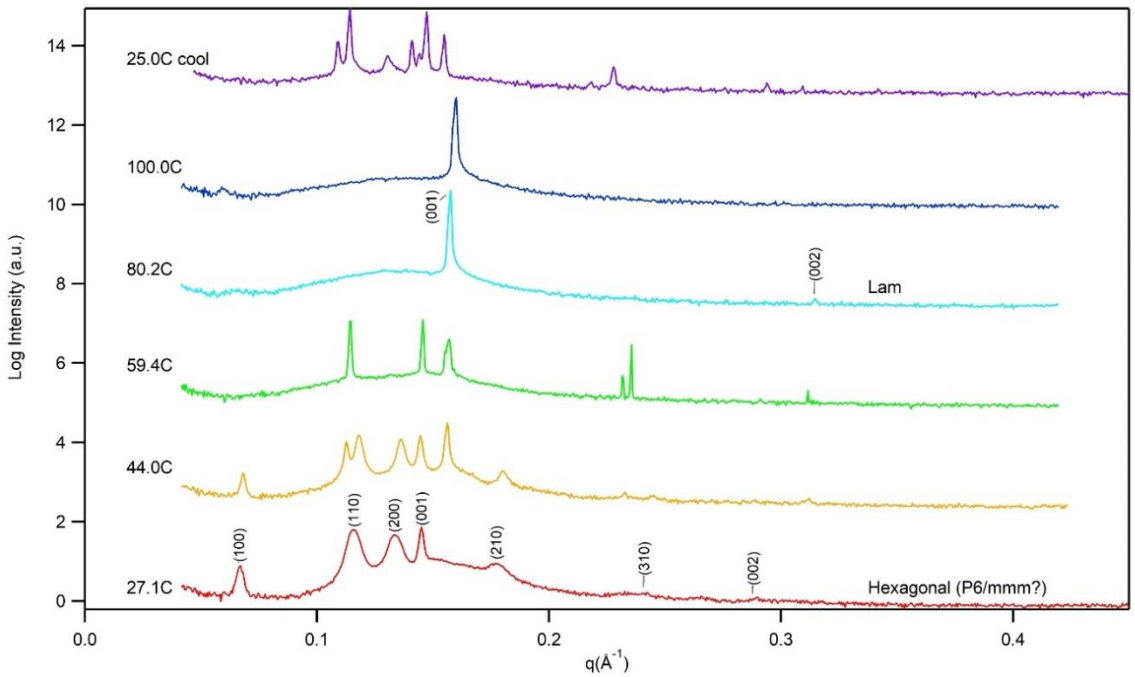

Figure A1.3: 1D SAXS patterns of **K-oleate** at 60 wt%

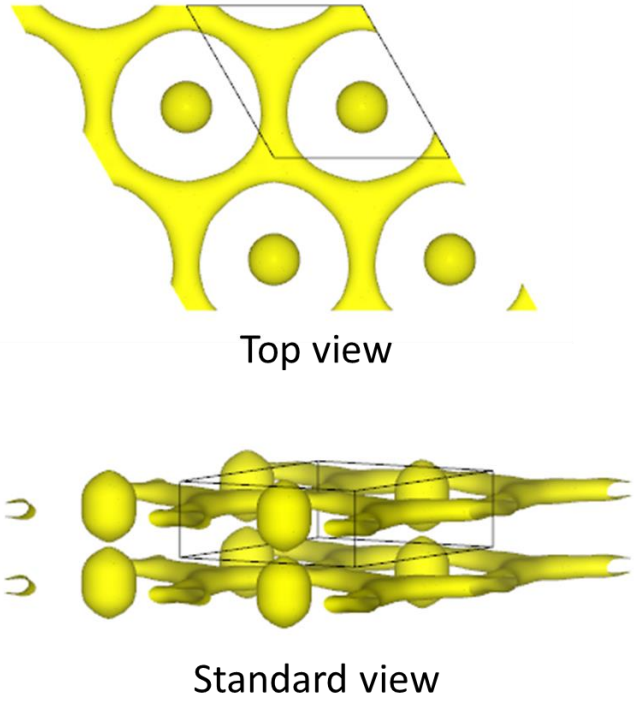

Figure A1.4: Electron density reconstruction of **K-oleate** at 60 wt%

The 90% isosurface of **K-oleate** at 60 wt% and 27 °C with *P6/mmm* symmetry. This electron density was constructed from one convergence and could not be replicated. The figures of merit (fm = 56) is poor, suggesting a less than ideal fit.

A1.2.4 70 wt% - Rectangular Ribbon Phase

Luzzati and coworkers assigned a **K-oleate** sample at 64 wt% (20 °C) as primitive rectangular (*pmm*) ribbon phase (Figure A1.1 a) with unit cell dimensions a = 53.9 Å and b = 41.9 Å.[8] Later work by Hagslätt, *et al*. showed that this pattern could also be indexed as centered rectangular (*cmm*) ribbon phase with unit cell dimensions of a = 107.8 Å and b = 45.5 Å.[9] Luzzati and coworkers noted that while the ribbon phase could be misinterpreted as two distinct sets of lamellae peaks, that since the a/b ratio is invariant with concentration that it is its own distinct phase.[8] While neither SAXS patterns in this study collected at 60 wt% and 65 wt% (27 °C) could be indexed with either primitive rectangular or centered rectangular unit cell, the anisotropic 2D patterns (Figure A1.5)

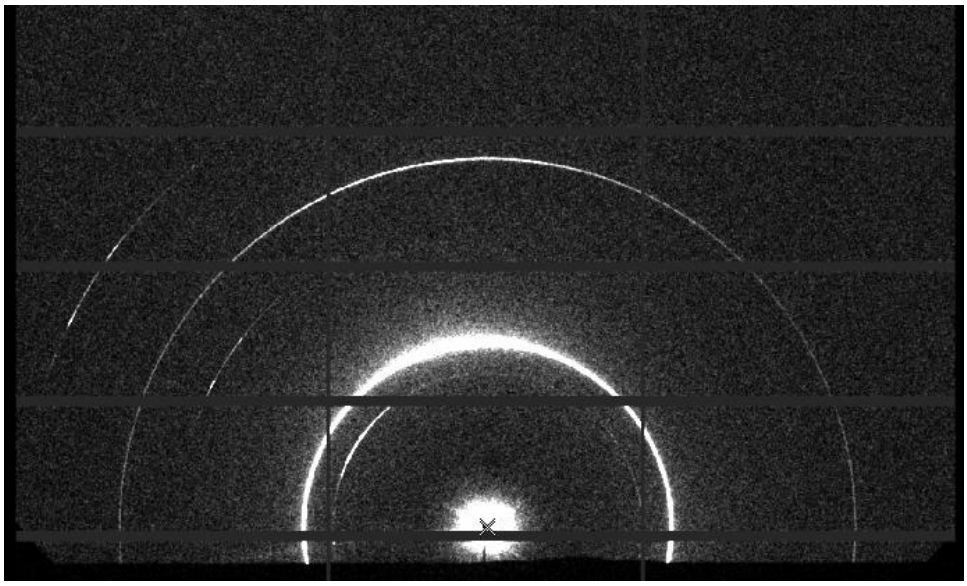

Figure A1.5: 2D SAXS pattern of **K-oleate** at 70 wt% and 59.4 °C

Two different sets of lamellae peaks are observed, (d_1 = 44 Å, d_2 = 37 Å). This may be a rectangular ribbon phase, but more likely to be two sets of lamellae peaks due to the high anisotropy of one set of rings.

collected at 70 wt% (44 − 100 °C) could be indexed as either primitive rectangular (a = 44 Å, b = 37 Å) or centered rectangular (a = 89.2, b = 42.0) for 44 °C. Since this pattern only occurs at one concentration, it is not possible to distinguish between a ribbon phase and two sets of lamellae. This pattern only occurs in the top and middle pan shots, but not the bottom pan shot which show only one set of L_α (d_2 = 37 Å); thus, indicating that the sample is heterogeneous. The first set of lamellar peaks (d_1 = 44 Å) which appear to have rather aligned grains in the 2D SAXS pattern have the same *d*-spacing as anhydrous **K-oleate**.[10] Since there was some sample on the outside of the pan, it seems more likely that this scattering is pattern is L_α and L_c.

A1.3 Surface Area Calculations for Different Phases

A1.3.1 Lamellae (L_α)

First, a geometric argument based on the interfacial area for a "unit cell" will be made to calculate the surface area per headgroup, a_0. Second, it will be shown that this calculation matches the a_0 calculation by Kulkarni, *et al*. using a molecular geometric argument.[11]

Assume that the mass densities of the constituent oil and water phases are, $\rho = \rho_l = \rho_w = 1\,\frac{g}{cm^3} = 10^{-24}\,\frac{g}{\text{Å}^3}$. Since the lipid density is assumed to be equal to the water density, then the lipid volume fraction, ϕ_l, is equal to the lipid mass fraction, x_l. Hence,

$$\phi_l = 1 - \phi_w = x_l = 1 - x_w \tag{A1.1}$$

The lamellar unit cell will have a height equal to the repeat distance of the layers, d, and an arbitrary area, A. Hence, the volume of the unit cell, V_{uc}, is

$$V_{uc} = dA \tag{A1.2}$$

The interfacial area per headgroup can be expressed as,

$$a_0 = \frac{a_{uc}}{n_h} \tag{A1.3}$$

where a_{uc} is the interfacial area per unit cell between the hydrophilic layer and the hydrophobic layer and n_h is the number of headgroups per unit cell. Since there are two interfacial planes per unit cell,

$$a_{uc} = 2A. \tag{A1.4}$$

The number of headgroups per unit cell, n_h, can be calculated as

$$n_h = \frac{\rho N_A v_l m_h}{M_w} \tag{A1.5}$$

where N_A is Avagrado's number, v_l is the hydrophobic volume per unit cell, m_h is the number of headgroup's per lipid molecule, and M_w is the molecular weight of the molecule.

$$v_l = \phi_l V_{uc} = \phi_l dA = x_l dA \tag{A1.6}$$

Hence, plugging Equation A1.5 and A1.6 into A1.3 gives,

$$a_0 = \frac{2AM_w}{\rho N_A m_h x_l dA} = \frac{2M_w}{\rho N_A m_h x_l d}. \tag{A1.7}$$

Notice, that the arbitrary unit cell area, A, is not in the final expression of a_0.

Using the molecular approach that Kulkarni *et al*. used,[11] the geometry for a single lipid in L_α can be approximated as a cylinder. Hence, a_0 can be expressed as,

$$a_0 = \frac{v_{l,i}}{d_l m_h} \tag{A1.8}$$

where $v_{l,i}$ is the volume of an individual lipid molecule and d_l is the monolayer thickness (or height of a single lipid). $v_{l,i}$ can be represented as

$$v_{l,i} = \frac{M_w}{\rho N_A} \tag{A1.9}$$

and d_l can be represented as

$$d_l = \tfrac{1}{2}\phi_l d = \tfrac{1}{2}x_l d \quad \text{(A1.10)}$$

Hence, substituting Equations A1.9 and A1.10 back into A1.8 gives the same result as Equation A1.7.

A1.3.2 Normal Hexagonal (H_I)

For H_I, a_0 will be calculated using the same unit cell geometrical approach as L_α. The "unit cell" will be a 3-dimensional hexagonal unit cell where the unit cell parameter, *a*, is the intercylinder distance, d, and *c* is an arbitrary height, l. There is one column per unit cell. Hence the volume is given by,

$$V_{uc} = \frac{3^{1/2} l d^2}{2} \quad \text{(A1.11)}$$

The interfacial area of the unit cell is given by the surface area for a cylinder (without the top and bottom),

$$a_{uc} = 2\pi r l \quad \text{(A1.12)}$$

where r is the radius of the column, which can be solved for by setting the volume fraction of the lipid to the ratio of volume of a cylinder to the volume of the unit cell,

$$\phi_l = x_l = \frac{v_l}{V_{uc}} = \frac{\pi r^2 l}{\frac{1}{2}3^{1/2} l d} = \frac{2\pi r^2}{3^{1/2} d}. \quad \text{(A1.13)}$$

Using, Equation A1.13, we can solve for r,

$$r = \frac{3^{1/4} x_l^{1/2} d}{2^{1/2}\pi^{1/2}}. \quad \text{(A1.14)}$$

Substituting Equation A1.14 into A1.12 gives,

$$a_{uc} = 2^{1/2} 3^{1/4} \pi^{1/2}\, l x_l^{1/2} d. \quad \text{(A1.15)}$$

Substituting, v_l and Equation A1.14 into A1.5 gives,

$$n_h = \frac{\rho N_A m_h v_l}{M_w} = \frac{\rho N_A m_h \pi r^2 l}{M_w} = \frac{3^{1/2} \rho N_A m_h l x_l^{1/2} d^2}{2M_w}. \quad \text{(A1.16)}$$

Finally, substituting Equations A1.15 and A1.16 into A1.3 gives

$$a_0 = \frac{a_{uc}}{n_h} = \frac{2^{3/2} \pi^{1/2} M_w}{3^{1/4} x_l^{1/2} \rho N_A m_h d}. \quad \text{(A1.17)}$$

A1.3.3 Hexagonal Closest Packed (HCP_I)

Similarly, a_0 can be calculated for HCP_I using Equation A1.3. The unit cell is 3-dimensional hexagonal with the unit cell parameters a and c. There are two spheres per unit cell. The volume of the unit cell, V_{uc}, is

$$V_{uc} = \frac{3^{1/2} c a^2}{2} \quad \text{(A1.18)}$$

and the interfacial area is given by,

$$a_{uc} = 2(4\pi r^2) = 8\pi r^2 \quad \text{(A1.19)}$$

where r is the radius of a sphere, which can be solved for by setting the volume fraction of the lipid to the ratio of volume of a cylinder to the volume of the unit cell,

$$\phi_l = x_l = \frac{v_l}{V_{uc}} = \frac{\frac{8}{3}\pi r^3}{\frac{3^{1/2} l d^2}{2}} = \frac{16\pi r^2}{3^{3/2} c a^2}. \quad \text{(A1.20)}$$

Equation A1.20 can be solved for r to give,

$$r = \frac{3^{1/2} c^{1/3} a^{2/3} x_l^{1/3}}{2^{4/3} \pi^{1/3}}. \quad \text{(A1.21)}$$

Substituting Equation A1.21 into A1.19 gives,

$$a_{uc} = 2^{1/3} 3 \pi^{1/3} c^{2/3} a^{4/3} x_l^{2/3} \quad \text{(A1.22)}$$

and v_l and Equation A1.21 into A1.5 gives,

$$n_h = \frac{\rho N_A m_h v_l}{M_w} = \frac{3^{1/2} \rho N_A m_h c a^2 x_l}{2M_w}. \quad \text{(A1.23)}$$

Finally, substituting Equation A1.22 and A1.23 into A1.3 gives,

$$a_0 = \frac{a_{uc}}{n_h} = \frac{2^{4/3}3^{1/2}\pi^{1/3}M_w}{\rho N_A m_h c^{1/3} a^{2/3} x_l^{1/3}}. \quad \text{(A1.24)}$$

A1.3.4 Normal Gyroid (G_I)

The interfacial area per headgroup for G_I was calculated following the method reported by Gulink, *et al*., and subsequently Jackson, *et al*. This method assumes that a G_I-phase (with 3-fold connectors) unit cell consists of 24 straight, cylindrical rods that are beveled near the connectors.

A1.4 Spacing Filling Calculation of Partially Interdigitated Bilayers

If one imagines filling space with cylindrical "lipids", both a non-interdigitated structure and a fully interdigitated structure fill space quite well, with a small amount of void area (Figure A1.6). However, trying to fill space with a partially interdigitated structure creates a large amount of voids. The middle region in which the cylinders overlap has twice the density of the outside regions (Figure A1.6). However, the oleate tail is not cylindrical due to the *cis* unsaturation. This kink gives the oleate tail the ability to pack in a partially interdigitated membrane and fill space at a constant density within the bilayer.

If the problem is generalized to 2-dimensions, then the areal density of hydrocarbon tails in regions x and y must be equal (Figure A1.7). By defining l to be the total hydrocarbon length in region x and m to be the total hydrocarbon length in region y, then the areal densities can be expressed as

$$\frac{l\rho}{xa} = \frac{m\rho}{ya} \rightarrow \frac{l}{x} = \frac{m}{y} \quad \text{(A1.25)}$$

where a is some arbitrary length of membrane and ρ is the mass per length of hydrocarbon (or linear density of hydrocarbon).

The distance from the carbonyl carbon to the first olefin carbon is b = 9.92 Å and the length from the second olefin carbon to the terminal methyl carbon is c = 9.92 Å for an oleate tail. Thus, we can use b and c to define l and m, respectively, to give

$$l = nb \text{ and } m = 2nc$$

where n is the number of tails in a monolayer of the length a. Substituting l and m into Equation A1.25 gives

$$\frac{b}{x} = \frac{2c}{y} \rightarrow y = \frac{2cx}{b}. \quad \text{(A1.26)}$$

The bilayer thickness, t, is obtained by multiplying the L_α d-spacing by the volume fraction of the surfactant which assumes a hard interface. t can also be expressed in terms of x and y,

$$t = 2x + y. \quad \text{(A1.27)}$$

Substituting Equation A1.26 into Equation A1.27 and rearranging for x gives

$$x = \frac{t}{2\left(1+\frac{c}{b}\right)} = \frac{tb}{2(c+b)}. \quad \text{(A1.28)}$$

Finally, the tail angle from the surface normal, θ, can be found by,

$$\theta = \cos^{-1}\left(\frac{x}{b}\right). \quad \text{(A1.29)}$$

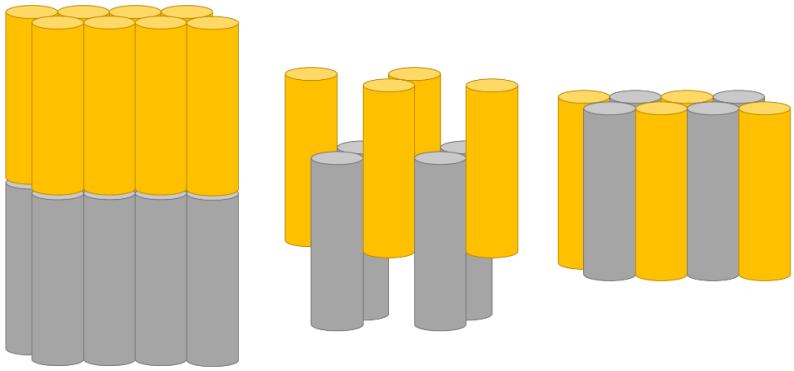

Figure A1.6: 3-dimensional packing of cylinders for a non-interdigitated, partially interdigitated, and fully interdigitated structure

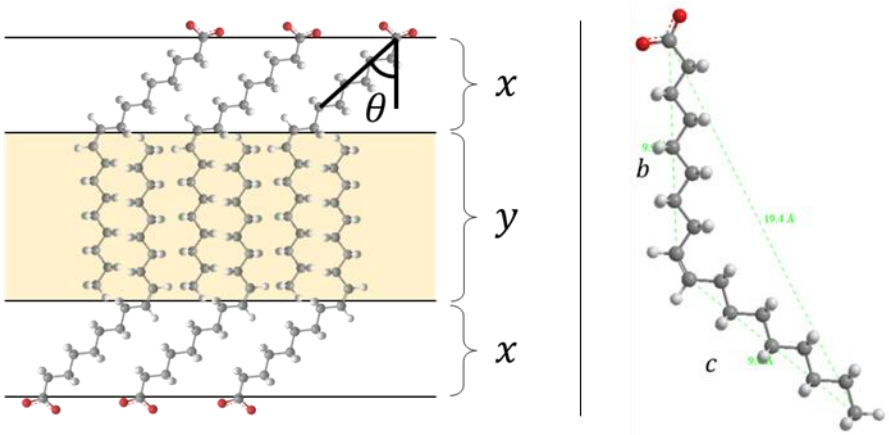

Figure A1.7: Diagram of partially interdigitated bilayer

Oleate salts packed in a partially interdigitated bilayer where x and y have an equal density of hydrocarbon tails (left). 3-dimensional structure of an oleate salt (counterion not shown) where the length from the carbonyl carbon to terminal methyl carbon is 19.4 Å, tail segment b is 9.92 Å, and tail segment c is 9.92 Å (right).

A1.5 Data Tables for LLC Phase Behavior

Table A1.2: Phase data for **NMe_4-oleate**/water and **K-oleate**/water mixtures.

surfactant	**NMe_4-oleate**												**K-oleate**					
M_w (g/mol)	355.6												320.6					
phase	**HCP_I**		**H_I**						**G_I**	**L_α**			**H_I**			**L_α**		
wt% surfactant	20	25	28	33	40	45	50	55	65	75	80	85	40	45	50	65	70	75
mol water/ mol headgroup, W_0	79.0	59.2	50.8	40.1	29.6	24.1	19.7	16.2	10.6	6.6	4.9	3.5	26.7	21.8	17.8	9.6	7.6	5.9
lipid volume fraction, x_l	0.20	0.25	0.28	0.33	0.40	0.45	0.50	0.55	0.65	0.75	0.80	0.85	0.40	0.45	0.50	0.65	0.70	0.75
d (Å)	-	-	-	-	-	-	-	-	-	36.6	35.5	34.5	-	-	-	39.8	38.3	37.4
a (Å)	77.4	72.7	61.8	60.1	56.5	54.8	53.1	51.5	101.4	-	-	-	60.1	57.6	54.9	-	-	-
c (Å)	126.0	118.6	-	-	-	-	-	-	-	-	-	-	-	-	-	-	-	-
bilayer thickness (Å)	-	-	-	-	-	-	-	-	-	27.5	28.4	29.3	-	-	-	25.9	26.8	28.1
unit cell volume ($Å^3$)	6.53E+05	5.43E+05	-	-	-	-	-	-	1.04E+06	-	-	-	-	-	-	-	-	-
cylinder length, λ (Å)	-	-	-	-	-	-	-	-	35.85	-	-	-	-	-	-	-	-	-
radius, r (Å) (sphere or cylinder)	25.0	25.3	17.2	18.1	18.8	19.3	19.7	20.1	15.9	-	-	-	20.0	20.3	20.4	-	-	-
hydrophobic volume per unit cell ($Å^3$)	1.31E+05	1.36E+05	-	-	-	-	-	-	5.36E+05	-	-	-	-	-	-	-	-	-
interfacial area per unit cell ($Å^3$)	1.57E+04	1.61E+04	-	-	-	-	-	-	5.80E+04	-	-	-	-	-	-	-	-	-
hydrophobic vol/unit cell vol	0.200	0.250	-	-	-	-	-	-	0.514	-	-	-	-	-	-	-	-	-
headgroups per unit cell	221	230	-	-	-	-	-	-	1148	-	-	-	-	-	-	-	-	-
aggregation number	111	115	-	-	-	-	-	-	-	-	-	-	-	-	-	-	-	-
interfacial area/headgroup ($Å^2$)	70.9	70.0	68.8	65.2	62.9	61.2	60.0	58.9	50.5	43.0	41.6	40.3	53.3	52.5	52.2	41.2	39.7	38.0
distance between headgroups (Å)	9.0	9.0	8.9	8.7	8.5	8.4	8.3	8.2	7.6	7.0	6.9	6.8	7.8	7.8	7.8	6.9	6.8	6.6

Table A1.3: Partially interdigitated bilayer tail packing data for **NMe_4-oleate** and **K-oleate**

surfactant	**NMe_4-oleate**			**K-oleate**		
M_w (g/mol)	355.6			320.6		
phase	**L_α**			**L_α**		
wt% surfactant	75	80	85	65	70	75
mol water/ mol headgroup, W_0	6.6	4.9	3.5	9.6	7.6	5.9
lipid volume fraction, x_l	0.75	0.80	0.85	0.65	0.70	0.75
d (Å)	36.6	35.5	34.5	39.8	38.3	37.4
bilayer thickness (Å)	27.5	28.4	29.3	25.9	26.8	28.1
interfacial area/headgroup ($Å^2$)	43.0	41.6	40.3	41.2	39.7	38.0
distance between headgroups (Å)	7.0	6.9	6.8	6.9	6.8	6.6
b (Å)	9.9	9.9	9.9	9.9	9.9	9.9
c (Å)	9.9	9.9	9.9	9.9	9.9	9.9
x (Å)	6.9	7.1	7.3	6.5	6.7	7.0
y (Å)	13.7	14.2	14.7	12.9	13.4	14.0
tail angle from normal, θ (°)	46.2	44.3	42.4	49.3	47.5	45.0
density of y (g/mL)	0.71	0.71	0.71	0.79	0.79	0.79
density of bilayer (g/mL)	0.79	0.79	0.79	0.88	0.88	0.88

A1.6 ***NMe$_4$-oleate*** *Microemulsions*

In preliminary work with adding tetradecane to **NMe$_4$-oleate** at 10 wt% oil loading, an initial phase assignment of dodecagonal quasicrystal (DDQC) + H_I was observed at 40 wt% surfactant and 100 °C (Figure A1.8). The DDQC unit cell parameter index to a = 160.7 Å and c = 157.5 Å. Previously, Zeng *et al*. reported a dendritic system which transitioned from H to DDQC upon heating.[12] Soft material DDQC have been subsequently studied and reported.[13-15]

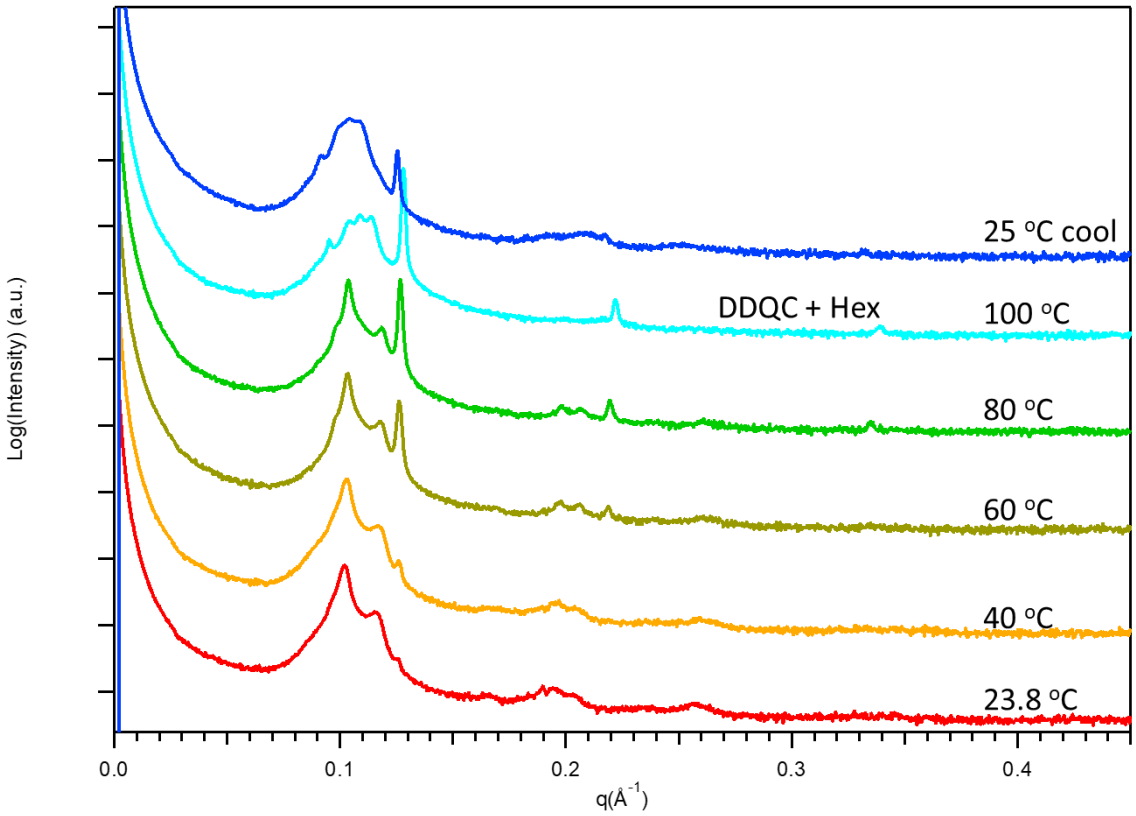

Figure A1.8: 1D SAXS patterns of **NMe$_4$-oleate** at 10 wt% tetradecane loading and 40 wt% surfactant.

A1.7 References

1. Jackson, G. L.; Poulsen, K. M.; Bible, N. G.; Jennings, J.; Mahanthappa, M. K., Polycontinuous network phase formation in single-tail surfactants induced by anisotropic gemini surfactant inclusions. *Manuscript in preparation*.

2. Kekicheff, P.; Cabane, B., Between cylinders and bilayers: Structures of intermediate mesophases of the SDS/water system. *J. Phys. (Paris)* **1987,** *48* (9), 1571-1583.

3. Luzzati, V.; Husson, F., The structure of the liquid-crystalline phases of lipid-water systems. *J. Cell Biol.* **1962,** *12* (2), 207-219.

4. Petříček, V.; Dušek, M.; Palatinus, L., Crystallographic computing system JANA2006: general features. *Zeitschrift für Kristallographie-Crystalline Materials* **2014,** *229* (5), 345-352.

5. Palatinus, L.; Chapuis, G., SUPERFLIP–a computer program for the solution of crystal structures by charge flipping in arbitrary dimensions. *J. Appl. Crystallogr.* **2007,** *40* (4), 786-790.

6. Momma, K.; Izumi, F., VESTA 3 for three-dimensional visualization of crystal, volumetric and morphology data. *J. Appl. Crystallogr.* **2011,** *44* (6), 1272-1276.

7. Chen, B.; Zeng, X. B.; Baumeister, U.; Diele, S.; Ungar, G.; Tschierske, C., Liquid crystals with complex superstructures. *Angew. Chem. Int. Ed.* **2004,** *43*, 4621-4625.

8. Luzzati, P.; Mustacchi, H.; Husson, F.; Skouliosn, A., The structures of colloid association 1. The liquid crystalline phases of amphiphile-water systems. *Acta Crystallog. A* **1960,** *13*, 660-667.

9. Hagslätt, H.; Söderman, O.; Jönsson, B., The structure of intermediate ribbon phases in surfactant systems. *Liq. Cryst.* **1992,** *12* (4), 667-688.

10. Cistola, D. P.; Atkinson, D.; Hamilton, J. A.; Small, D. M., Phase behavior and bilayer properties of fatty acids: hydrated 1: 1 acid-soaps. *Biochemistry* **1986,** *25* (10), 2804-2812.

11. Kulkarni, C. V.; Wachter, W.; Iglesias-Salto, G.; Engelskirchen, S.; Ahualli, S., Monoolein: a magic lipid? *Phys. Chem. Chem. Phys.* **2011,** *13* (8), 3004-3021.

12. Zeng, X.; Ungar, G.; Liu, Y.; Percec, V.; Dulcey, A. E.; Hobbs, J. K., Supramolecular dendritic liquid quasicrystals. *Nature* **2004,** *428* (6979), 157-160.

13. Yue, K.; Huang, M.; Marson, R. L.; He, J.; Huang, J.; Zhou, Z.; Wang, J.; Liu, C.; Yan, X.; Wu, K., Geometry induced sequence of nanoscale Frank–Kasper and quasicrystal mesophases in giant surfactants. *Proc. Natl. Acad. Sci. USA* **2016,** *113* (50), 14195-14200.

14. Gillard, T. M.; Lee, S.; Bates, F. S., Dodecagonal quasicrystalline order in a diblock copolymer melt. *Proc. Natl. Acad. Sci. USA* **2016,** *113* (19), 5167-5172.

15. Fischer, S.; Exner, A.; Zielske, K.; Perlich, J.; Deloudi, S.; Steurer, W.; Lindner, P.; Förster, S., Colloidal quasicrystals with 12-fold and 18-fold diffraction symmetry. *Proc. Natl. Acad. Sci. USA* **2011,** *108* (5), 1810-1814.

Appendix 2: Supporting Information for Chapter 3 - Synthesis and LLC Phase Behavior of Oleate Gemini

A2.1 Experimental Details for Olefin Metathesis Route

A2.1.1 Relevant Notebook Page Numbers

Table A2.1: Laboratory notebook page numbers for synthesis steps of oleate gemini, **4**, via olefin metathesis

Molecule	Notebook Page
1	MTH-I-089
2	MTH-I-120
3	MTH-I-132
4	MTH-I-150

A2.1.2 Metathesis Conditions

Table A2.2: Olefin metathesis conditions and yields

Olefin metathesis conditions with corresponding 2-step yields and mol% of desired molecular weight product determined by mass spectrometry (MS) for metathesis products after silica gel chromatography column.

Notebook Page #	Molarity of **2**	Inhibitor	Nonene	Rxn time & temp	2-Step Yield **1→2→3**	Desired MW by MS
I-132	.457 mol/L THF	0.2 equiv BQ	6 equiv	4 h 35°C	20%	68.6%
I-140	.458 mol/L DCM	0.2 equiv BQ	3 equiv	1 h 40°C	15%	68.8%
I-147	.412 mol/L DCM	0.4 equiv TFBQ	3 equiv	45 min 38°C	22%	83.1%
I-153	.483 mol/L DCM	0.4 equiv TFBQ	3 equiv	30 min 40°C	13.2%	95.7%

A2.1.3 Regioselectivity with HG2

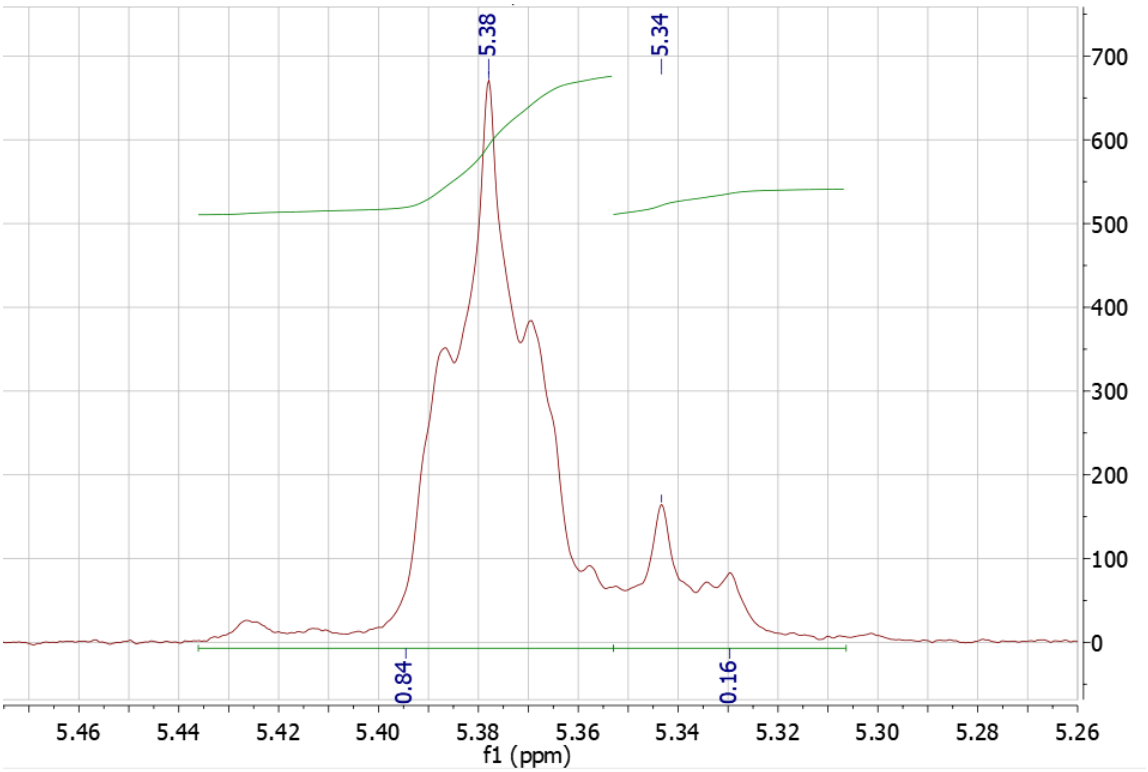

Figure A2.1: ^{1}H NMR of olefinic protons for HG2 catalyzed product

^{1}H NMR ($CDCl_3$) of olefinic protons for sample MTH-I-132 synthesized using HG2 as metathesis catalyst showed a peak at 5.38 ppm corresponding to the *trans*-product and a peak a 5.34 ppm corresponding to the *cis*-product. While the peaks overlap, it is estimated that the final product was ~84 mol% *cis*.

A.2.1.4 Isomerization Byproducts

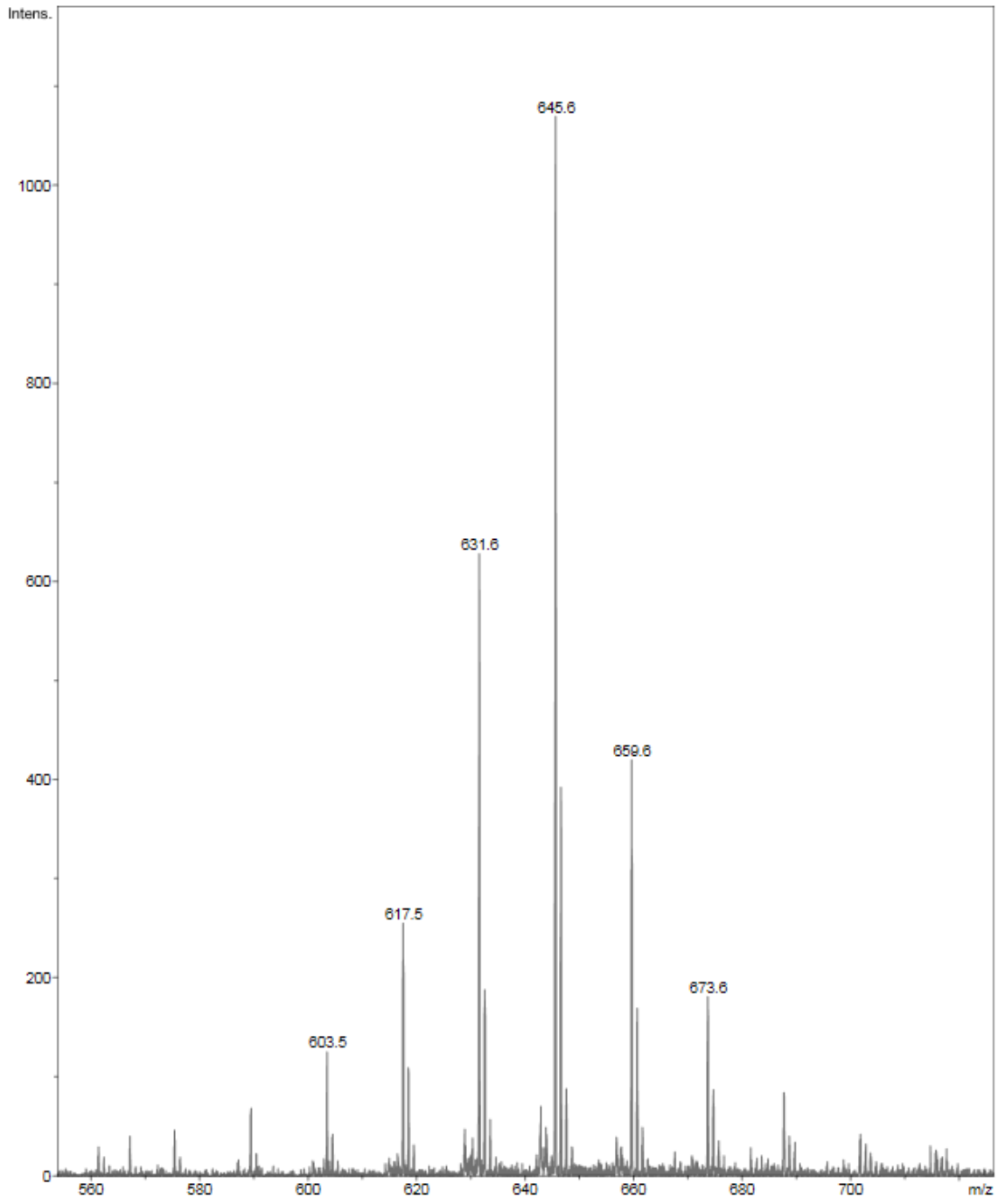

Figure A2.2: Mass spectrometry showing isomerization products without inhibitor

EOS-TOF mass spectrometry using negative mode of oleate gemini dicarboxylate, **4** (exact mass = 646.59 g/mol), without inhibitor during metathesis reaction. Labeled in the figure are: M-43 (603.5), M-29 (617.5), M-15 (631.3), M-1 (645.6), M+13 (659.6), and M+27 (673.6) peaks, indicating the difference of one methylene group between peaks.

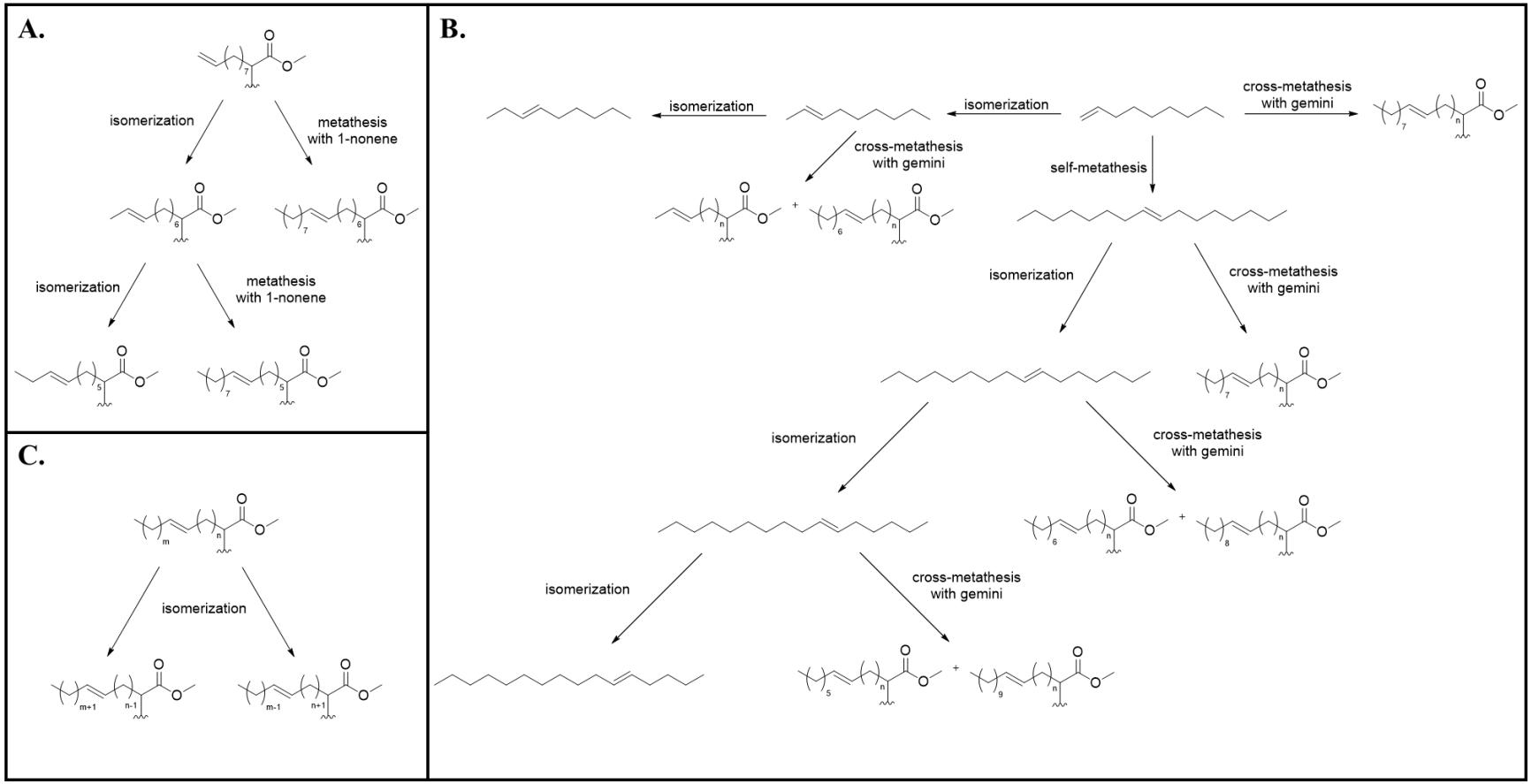

Figure A2.3: Isomerization pathways

The isomerization processes leading to disperse gemini surfactants after metathesis reaction: A.) isomerization of starting material, B.) isomerization process of nonene and nonene dimer, and C.) isomerization of gemini after metathesis.

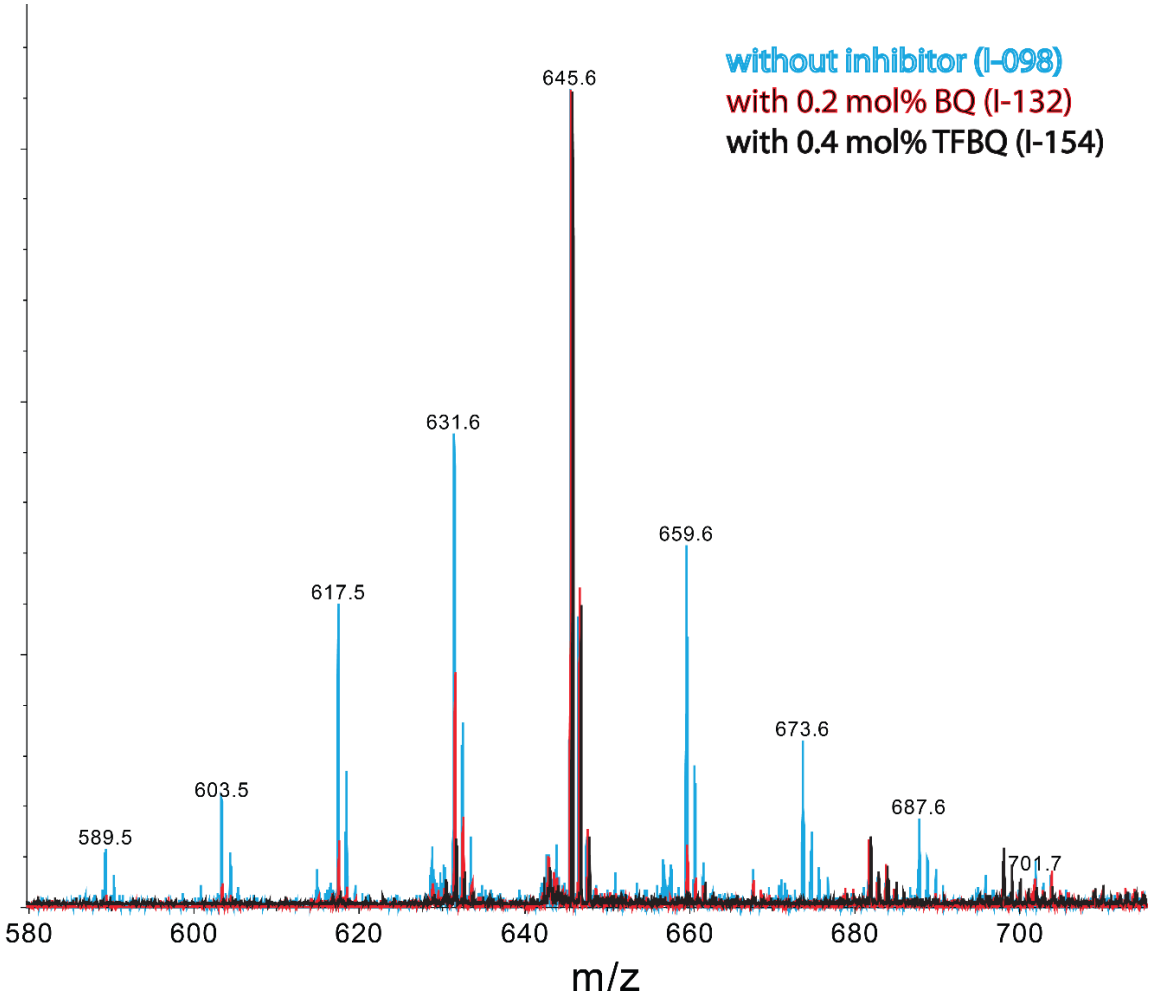

Figure A2.4: Mass spectrometry showing reduction of isomerization products with inhibitor

EOS-TOF mass spectrometry using negative mode of oleate gemini dicarboxylate, **4** (exact mass = 646.59 g/mol) synthesized: without inhibitor (*blue trace*), with 0.2 mol% benzoquinone (*red trace*), and with 0.4 mol% tetrafluorobenzoquinone (TFBQ) (*black trace*). Labeled in the figure are: M-57 (589.5), M-43 (603.5), M-29 (617.5), M-15 (631.6), M-1 (645.6), M+13 (659.6), M+27 (673.6) peaks M+41 (687.6) and M+55 (701.7), indicating the difference of a methylene group between peaks. The addition of inhibitors reduced isomerization products, with TFBQ showing >95 mol% desired molecular weight.

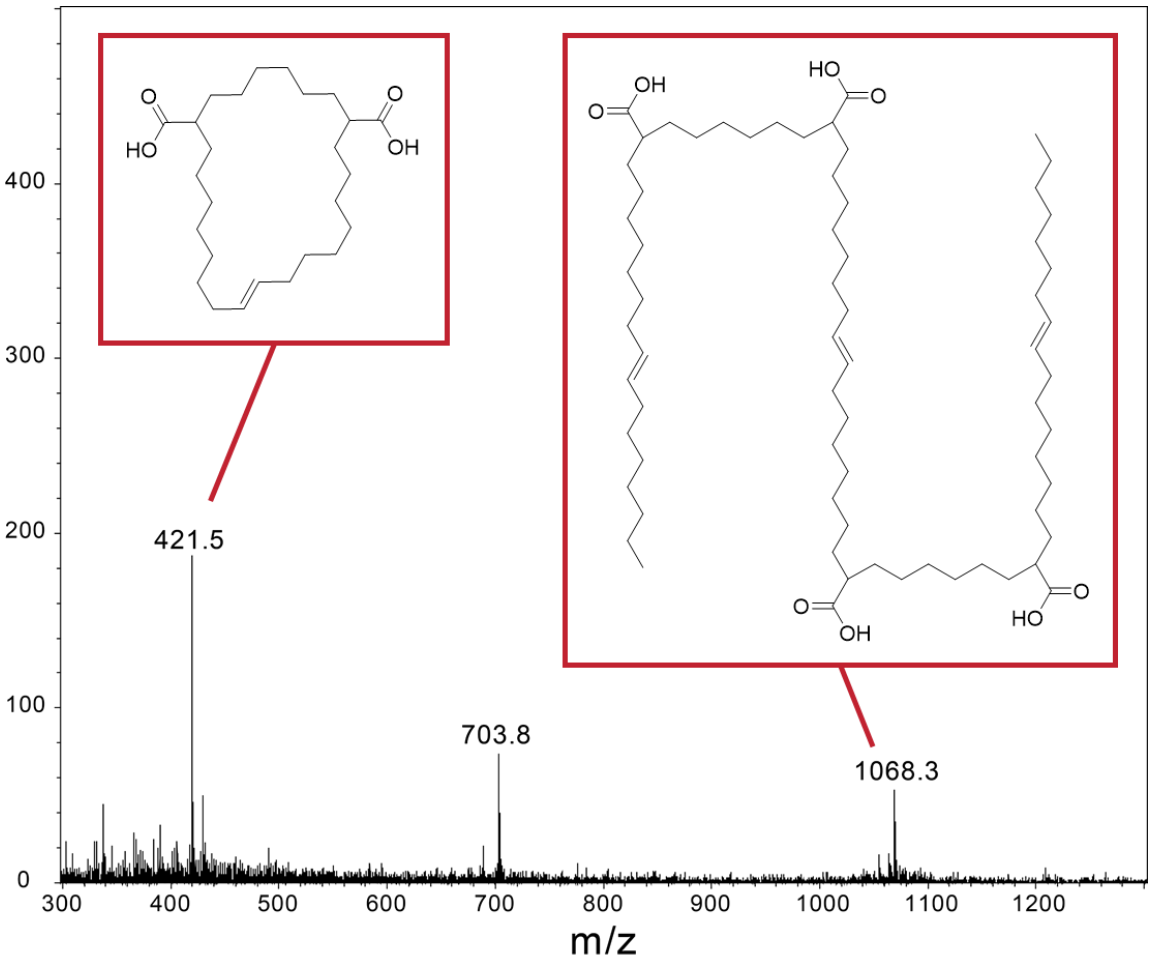

Figure A2.5: Mass spectrometry showing ring-closing metathesis and higher order coupling byproducts

EOS-TOF mass spectrometry using negative mode of ring-closing metathesis, M-1 = 421.5, and higher order coupling byproducts, M-1 = 1068.3, formed during olefin metathesis. The peak at 703.8 is a fragment of the higher order coupling byproduct.

A2.2 Experimental Details for Wittig Route

A2.1.1 Relevant Notebook Page Numbers

Table A2.3: Laboratory notebook page numbers for synthesis steps of oleate gemini, **11**, via Wittig olefination

Molecule	Notebook Page
5	MTH-II-028
6	MTH-II-032
7	MTH-II-034
8	MTH-II-033
9	MTH-II-036
10	MTH-II-040
11	MTH-II-043

A2.2.2 Regioselectivity with Wittig Reaction

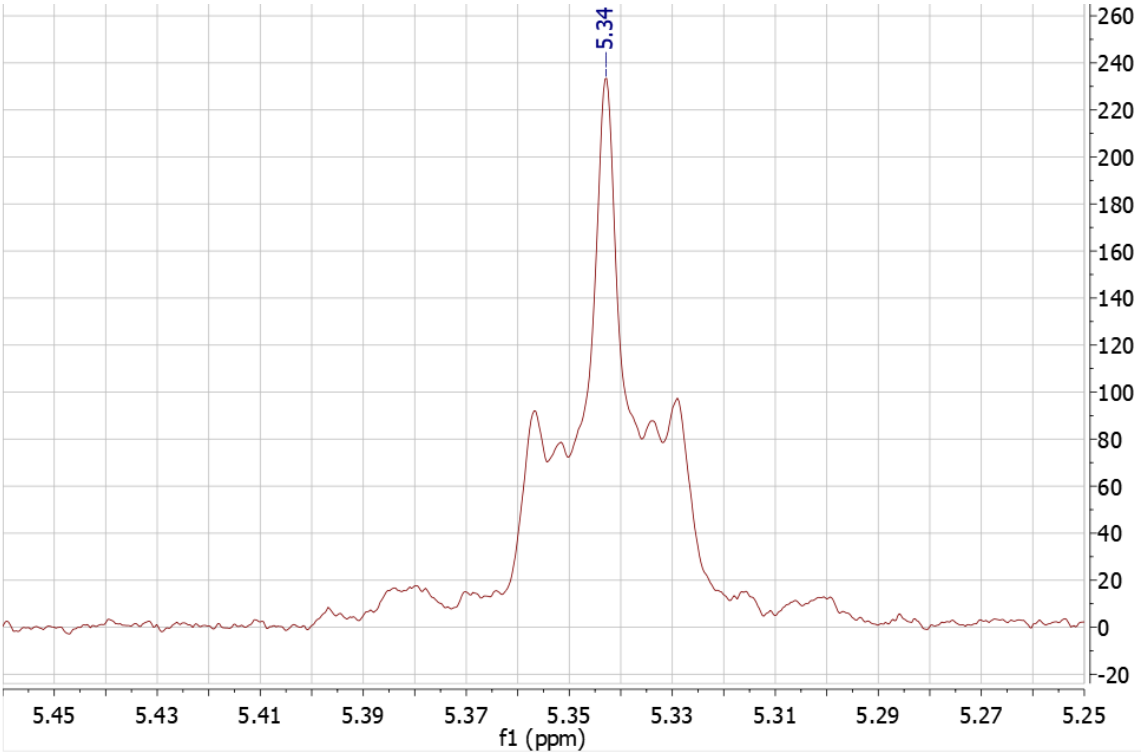

Figure A2.6: ^{1}H NMR of olefinic protons for *Z*-selective Wittig reaction

^{1}H NMR ($CDCl_3$) of olefinic protons for sample MTH-II-036 synthesized via a *Z*-selective Wittig route showed one peak at 5.34 ppm corresponding to the *cis*-product, thus, indicating >95 mol% *cis*-products.

A2.3 Data Table for LLC Phase Behavior

Table A2.4: Measured and calculated L_α parameters for K-C19:1 gemini (**11**)/water system

surfactant	**K-C19:1 gemini (32 acid : 68 soap)**				
M_w (g/mol)	726.5				
phase	**L_α**				
wt% surfactant	72	76	80	84	87
mol water/ mol headgroup, W_0	7.9	6.5	5.3	4.0	3.2
lipid volume fraction, x_l*	0.72	0.76	0.80	0.84	0.87
d (Å)	35.5	34.5	34.0	33.8	33.8
bilayer thickness (Å)	25.5	26.2	27.2	28.4	29.4
interfacial area/headgroup ($Å^2$)	47.3	46.0	44.3	42.5	41.0
distance between headgroups (Å)	7.4	7.3	7.2	7.0	6.9
b (Å)	9.9	9.9	9.9	9.9	9.9
c (Å)	9.9	9.9	9.9	9.9	9.9
x (Å)	6.4	6.6	6.8	7.1	7.4
y (Å)	12.8	13.1	13.6	14.2	14.7
tail angle from normal, θ (°)	50.0	48.6	46.7	44.3	42.2
desnity of y (g/mL)	1.39	1.39	1.39	1.39	1.39
density of bilayer (g/mL)	1.55	1.55	1.55	1.55	1.55